

Traceable Multicomponent Force and Torque Measurement

Dissertation

zur Erlangung des akademischen Grades
Doktoringenieur
(Dr.-Ing.)

vorgelegt der
Fakultät für Maschinenbau der
Technischen Universität Ilmenau

von Herrn

Rafael Ramos Marangoni, M.Sc.

geboren am 05.10.1990 in Porto Alegre/Brasilien

Gutachter: Univ.-Prof. Dr.-Ing. habil. Thomas Fröhlich, TU Ilmenau
Prof. Dr.-Ing. habil. Tino Hausotte, FAU Erlangen-Nürnberg
Dr.-Ing. Dorothea Knopf, PTB Braunschweig

vorgelegt am: 02.11.2018

verteidigt am: 26.02.2019

urn:nbn:de:gbv:ilm1-2019000043

Definition IV

An impressed force is an action exerted upon a body, in order to change its state, either of rest, or of uniform motion in a right line.

– I. Newton (1687)

ABSTRACT

The design of an instrument used to measure force and torque vectors that integrates a calibration system is described. The forces and torques are traced to position, angle, voltage, electrical resistance and time references. In terms of fundamental physical constants, the forces and torques can be traced to the Planck constant h , the speed of light in vacuum c and the hyperfine transition frequency of Caesium $\Delta\nu_{\text{Cs}}$. The measuring strategy used is based on the principle of the electromagnetic force compensation with the calibration based on the Kibble balance principle. Several difficulties and limitations of traditional calibration procedures for multicomponent force and torque transducers are overcome with this system and new features are introduced, such as the automatic in-process calibration. A careful uncertainty analysis is used to determine the achievable uncertainty for both force and torque measurements and identify the limitations caused by the components of the system. A prototype used to measure forces and torques in a range of $\pm 2.2 \text{ N}$ and $\pm 0.11 \text{ N m}$ with relative standard uncertainties of 44 ppm and 460 ppm respectively is presented. Considering the literature reviewed in this work, the system presented here exhibits the lowest uncertainty for the multicomponent force measurement. Verifications were performed by measuring a reference force generated by the weight of a calibrated test mass. Experimental results obtained by the application of multicomponent force and torque transducers to the Lorentz force velocimetry, micromachining and the identification of force and torque measuring systems are shown. Improvement possibilities for reducing the uncertainty for the force and torque measurements with the instrument are suggested.

KURZFASSUNG

Ein Gerät, das für die Messung von Kraft- und Drehmomentvektoren eingesetzt wird und ein Kalibriersystem integriert, wird in dieser Arbeit beschrieben. Die Kräfte und Drehmomente werden auf die Messung von Position, Winkel, elektrischer Spannung, elektrischem Widerstand und Zeit zurückgeführt. Hinsichtlich fundamentaler Naturkonstanten können die Kräfte und Drehmomente auf die Planck Konstante h , die Lichtgeschwindigkeit c und die Frequenz des Hyperfeinübergangs von Caesium $\Delta\nu_{\text{Cs}}$ zurückgeführt werden. Das Messprinzip basiert auf dem Prinzip der elektromagnetischen Kraftkompensation und die Kalibrierung auf dem Kibble-Waagen Prinzip. Mehrere Schwierigkeiten und Einschränkungen von traditionellen Kalibrierverfahren für Mehrkomponenten-Kraft- und Drehmomentaufnehmer werden mit diesem System überwunden und neue Möglichkeiten werden vorgeschlagen, wie z.B. die automatische Inprozess-Kalibrierung. Mithilfe einer sorgfältigen Unsicherheitsanalyse wird die erreichbare Unsicherheit für die Kraft- und Drehmomentmessung ausgewertet und die Einschränkungen identifiziert, die durch die verschiedenen Komponenten des Systems verursacht werden. Ein Prototyp wird vorgestellt, der die Kraft- und Drehmomentmessung im Bereich vom $\pm 2.2 \text{ N}$ und $\pm 0.11 \text{ N m}$ mit einer relativen Standardmessunsicherheit von 44 ppm bzw. 460 ppm ermöglicht. Weiterhin wurde das System durch die Messung einer bekannten Kraft überprüft, die von einem kalibrierten Testgewicht erzeugt wird. Experimentelle Ergebnisse wurden durch die Anwendung von Mehrkomponentenaufnehmern in der Lorentzkraft-Anemometrie, Mikrobearbeitung und für die Identifikation von Kraft- und Drehmomentmesssystemen erzielt. Auf Verbesserungsmöglichkeiten für die weitere Reduzierung der Unsicherheit bei der Kraft- und Drehmomentmessung mit dem Gerät wird eingegangen.

ACKNOWLEDGEMENTS

The results presented in this work were only possible due to the support of other people. I would like to acknowledge this support here.

The work was carried out at the Institute for Process Measurement and Sensor Technology of the Technische Universität Ilmenau. PROF. DR. THOMAS FRÖHLICH was my supervisor and I would like to thank him for all constructive discussions and the freedom provided during this research.

PROF. DR. RENÉ THESKA gave me the opportunity to come to Ilmenau and was my supervisor during a previous period as doctorate student at the Precision Engineering Group. I would like to thank him for all support provided in many ways during this period.

DR. JAN SCHLEICHERT did the first design of the multicomponent transducer and his work was a basis for this thesis. I would like to thank him for the (almost daily) discussions and the great support provided during all phases of this work.

DR. ILKO RAHNEBERG and DR. FALKO HILBRUNNER have contributed with several discussions and important ideas during this work.

DR. HANS-JOACHIM BÜCHNER shared his expertise with optics many times and helped me in the design of the experimental setup used for the calibrations with laser interferometer. DR. ROSTYSLAV MASTYLO has performed the measurements with the nanopositioning and nanomeasuring machine used to evaluate the results for micromachining. DR. DANIEL HERNÁNDEZ coordinated the work to obtain the measurement results in the mini-LIMMCAST plant of the Helmholtz Zentrum Dresden-Rossendorf. HELGE MAMMEN shared his expertise with resistance measurement and helped me in the calibration of the precision resistors. ULRIKE BLUMRÖDER has performed the measurements with the optical frequency comb to calibrate the reference laser and helped me in the design of the experimental setup for the laser frequency measurement. MATTHIAS RÖSER has manufactured several mechanical parts used in this work. I would like to thank this people and all colleagues from the Institute for Process Measurement and Sensor Technology, the Precision Engineering Group and the Research Training Group Lorentz Force who provided support in any way.

I would like to gratefully acknowledge the financial support from the Deutsche Forschungsgemeinschaft, in the framework of the Research Training Group 1567 “Lorentz force velocimetry and Lorentz force eddy current testing” and by the Free State of Thuringia.

The support I have received from my parents DENISE & WLADIMIR and my brother RENAN during my life was fundamental for this work. Finally, I would like to thank my wife JULIA for all support and the companionship.

CONTENTS

1	Introduction	1
2	Review of the state of art	5
2.1	Force measurement and weighing technology	5
2.2	Multicomponent force and torque measurement	8
2.2.1	Measuring systems	8
2.2.2	Calibration setups	8
2.3	Kibble balance experiments	13
3	Description of the instrument	19
3.1	Main components and operation	19
3.1.1	Driver unit	21
3.1.2	Sensing unit	23
3.1.3	Transducer functionality	24
3.2	Mathematical model	26
3.2.1	Mechanical hardware	26
3.2.2	Actuators' forces and torques	30
3.2.3	Induced voltages in the actuators	36
3.2.4	Position measurement	39
3.2.5	Effects of gravity acceleration	45
3.2.6	Metallic wires	46
3.2.7	Further considerations	48
3.2.8	The plant	48
3.3	Control system	49
3.3.1	Design and implementation	49
3.3.2	Controller for normal system operation	52
3.3.3	Controller for the system activation	54
3.3.4	Parametric system identification	54
3.3.5	Implementation results	56
3.3.6	Hybrid position and force control	57
4	Evaluation of the measurement uncertainty	61
4.1	Position and angle measurement	61
4.1.1	Measurement of the laser frequency	65
4.1.2	Laser wavelength determination in air	66
4.2	Voltage measurement	67
4.3	Resistance measurement	70
4.4	Time measurement	75
4.5	Further considerations	76
4.5.1	Coil-current effect	77

4.5.2	Inductive coupling between coils	79
4.6	Uncertainty budget	80
5	Verification of the results	85
5.1	Description of the measuring setup	85
5.2	Experimental results	87
6	Applications of the system	91
6.1	Identification of force and torque transducers	91
6.1.1	Experimental setup	92
6.1.2	Simulation model	94
6.1.3	Results for a strain gauge transducer	95
6.2	Lorentz force velocimetry	97
6.3	Micromachining	101
6.3.1	Experimental setup for micromachining	102
6.3.2	Results for micromachining	103
7	Conclusions	107
7.1	Main results	107
7.2	Outlook	109
A	Use of commercially available products	111
B	Terms and definitions	113
	Bibliography	115

LIST OF FIGURES

2.1	Force measurement principles	6
2.2	Electromagnetic force compensation principle	7
2.3	Hexapod-structured calibration device	9
2.4	Combined force and torque calibration device	9
2.5	GNU six-component calibration device	10
2.6	Single-vector force balance calibration system	11
2.7	Variable acceleration force calibration system	11
2.8	Multicomponent calibration setup with lever	12
2.9	Kibble balance experiment	15
3.1	Sensing element of the multicomponent transducer	19
3.2	System plan with the main components	20
3.3	Main board of the driver unit	21
3.4	Resistor board	22
3.5	Main board of the sensing unit	23
3.6	Control system activation routine	25
3.7	Reference frames for mathematical model	27
3.8	Voice coil actuator	31
3.9	Actuator force as a function of the position	32
3.10	Dimensional parameters of the sensing element	34
3.11	Aperture slit position sensor	40
3.12	Light in dual photodiode	40
3.13	Position sensor sensitivity	41
3.14	Form of gold wires	46
3.15	Fusing current and maximal force for wires	47
3.16	Block diagram for open loop system	49
3.17	Control system for one degree of freedom	51
3.18	Position noise amplification factor	53
3.19	Transducer eigenfrequency and damping factor	53
3.20	Center of mass identification	56
3.21	Natural frequency and force standard deviation	57
3.22	Natural frequency and torque standard deviation	57
3.23	Position noise amplification factor and standard deviation	58
3.24	Control systems for micromachining	58
4.1	Calibration setup for position and angle measurement	62
4.2	Measurement results for position and angle calibration	62
4.3	Temperature inside transducer	63
4.4	Stability evaluation for the position sensor	63
4.5	Repeatability for measurement with interferometer	64

4.6	Measurement of the laser wavelength	65
4.7	Calibration setup for voltage measurement	68
4.8	Experimental results for voltage calibration	69
4.9	Analog-to-digital converter deviation	69
4.10	Repeatability for induced voltage measurement	70
4.11	Measuring setup for resistor calibration	71
4.12	Self heating of the resistors	72
4.13	Measured resistance values	73
4.14	Traceable time measurement	75
4.15	Offset current determination	78
4.16	Coil current parameter determination	79
4.17	Inductive coupling determination	80
5.1	Sketch of verification setup with test mass	86
5.2	Picture of verification setup	86
5.3	Relative force deviation	88
5.4	Temperature, pressure and humidity variation	88
5.5	Coil-current effect deviations	89
5.6	Temperature dependency of the actuator constant	89
6.1	Experimental setup for transducer identification	92
6.2	Sensing element and test transducer	93
6.3	FEM model for transducer identification	94
6.4	Identification of the frequency response	95
6.5	Identification of the hysteresis effect	96
6.6	Shape from motion identification	97
6.7	Lorentz force velocimetry principle	98
6.8	Magnetic center and transducer center	98
6.9	Experimental setup for magnet center determination	99
6.10	Lorentz force measured with rotating disc	100
6.11	Continuous casting model	100
6.12	Interaction forces and torque with liquid metal	101
6.13	Experimental setup for surface micromachining	102
6.14	Test specimens for micromachining	102
6.15	Normal force as a function of position	103
6.16	Tangential forces as a function of position	104
6.17	Tool position as a function of time	104
6.18	Engraving forces and torques as a function of time	104

LIST OF TABLES

2.1	Calibration setups for multicomponent transducers	13
3.1	Position and angle of actuators	35
3.2	Control parameters for damping factor 0.7	54
4.1	Laser frequency uncertainty budget	66
4.2	Air refractive index uncertainty	67
4.3	Resistance values and uncertainties	74
4.4	Time or frequency measurement uncertainty	76
4.5	Uncertainty budget for the force measurement	83
4.6	Uncertainty budget for the torque measurement	83
5.1	Weight force uncertainty for the test mass	87
6.1	Eigenfrequencies from measurements and simulations	97
6.2	Specifications of the multicomponent transducer	103
7.1	Comparison between multicomponent transducers	109
A.1	List of commercial products	111

CHAPTER 1

INTRODUCTION

The measurement of forces and torques has a fundamental importance in research and industry [1, 2]. Although forces and torques are vector quantities, these terms are often used in the force and torque measurement literature as a reference to the measurement of one force or torque component. In some applications, the simultaneous measurement of several force and torque components is necessary. In such cases, multicomponent force and torque measuring systems are used. This is necessary for instance in the aerospace engineering [3], to measure forces and torques during aerodynamic tests with aircraft models in wind tunnels, in crash tests, to measure the mechanical loads in the body of crash dummies during tests [4], in the Lorentz Force velocimetry [5, 6], to measure the flow velocities in liquid metal flows, in micromachining tasks [7], to measure the interaction forces between the machining tool and the surface of the test specimen being machined, and in biomechatronics, to reproduce sensing mechanisms of animals [8, 9].

Depending on the application, different types of force and torque transducers are used. There are several systems available in the literature that use different working principles [10]. For measuring both static and dynamic forces and torques, systems based on the measurement of deformations in compliant structures or force compensation strategies are typically used. For systems that use the measurement of deformations, several realizations can be found. Most of them have a compliant mechanism made of aluminium, but other materials can be used such as ceramics [11]. Strain gauges are normally used to measure the deformations but other systems use, for instance, optical sensors or interferometers. This is an advantage in conditions with high electromagnetic interference (EMI). There are also transducers based on microelectromechanical systems (MEMS), which exhibit a very small form factor and can be integrated, for instance, in robotic hands. For force compensation strategies, electrostatic and electromagnetic forces are typically used. Electrostatic force compensation is normally used for the measurement of small forces, in ranges below milinewton. The principle of electromagnetic force compensation (EMFC) is used in modern precision scales to measure the weight force generated by masses. A multicomponent transducer based on the EMFC principle was designed and implemented in [12]. In this transducer, the sensing element is levitated by using a control system and the external forces and torques are compensated by electromagnetic actuators. These systems have several advantages when compared to transducers based on the measurement of deformations: a higher relative resolution can be achieved, displacements of the sensing element are compensated during the measurement and a more robust behavior can be obtained. Additionally, with this principle it

is possible to change the dynamic behavior of the transducer by modifying the parameters of the control system.

In order to use multicomponent transducers and obtain a traceable force and torque measurement, these systems must be calibrated. There are several setups used to calibrate multicomponent transducers [13]. In these systems, reference forces and torques are generated by using deadweights, the gravity acceleration and levers or pulleys. In this case, the force and torque measurements are traceable to mass, acceleration and length standards. There are also setups which use reference force and torque transducers to provide a traceable measurement. However, the reference transducers are usually calibrated by using deadweights and the gravity acceleration as well. These systems are used to perform calibration procedures described by standards and guidelines, such as the DIN EN ISO 376 [14], DAkkS DKD-R 3-3 [15] and DAkkS DKD-R 3-9 [16], for the calibration of force measurement devices, the DAkkS DKD-R 3-5 [17], DIN 51309 [18] and VDI/VDE 2646 [19], for the calibration of torque measurement devices, the ASTM F3109-16 [20], for the calibration of multicomponent force transducers, and the GTM-RL-002 for the calibration of multicomponent force and torque transducers. Further guidelines are the OIML R60 parts 1, 2 and 3 [21–23], which provide metrological regulations for load cells, and the VDI/VDE/DKD 2638 [24], which contains several terms and definitions for force transducers.

A multicomponent force and torque transducer which integrates the calibration procedure was presented in [25, 26]. This system is based on the Kibble balance [27] principle and can be used to measure forces and torques traceable to position, angle, voltage, resistance and time standards. The Kibble balance is a device used to measure the value of the Planck constant to be adopted in the revised version of the International System of Units (SI). This device will be used to realize the kilogram unit after the redefinition of the SI, which is planned to happen during the 26th meeting of the General Conference on Weights and Measures (*Conférence Générale des Poids et Mesures*, CGPM) in 2018. An alternative to the determination of the Planck constant and realization of the mass unit after the redefinition of the SI is the use of silicon spheres, as investigated in the Avogadro Project [28]. By using the knowledge of the Kibble balance principle in the multicomponent transducer, deadweights and the gravity acceleration are not necessary to perform the calibration task. Furthermore, since the calibration system is integrated in the transducer, the calibration procedure can be performed inside the process, without removing the transducer from the measuring setup. With the Kibble balance the weight of mass prototypes can be determined with a relative uncertainty near to 1×10^{-8} [29, 30] and the application of this principle to multicomponent transducers has the potential to reduce the achievable uncertainty for both force and torque measurements.

In the present work, an extensive description of the multicomponent transducer with integrated calibration is provided, from the design of a prototype used to measure forces and torques in a range of $\pm 2.2 \text{ N}$ and $\pm 0.11 \text{ N m}$ to the verification of the integrated calibration strategy. After this introduction, or in the second chapter, a review of the state of art for multicomponent force and torque measurements and for Kibble balances is shown. In the third chapter, a description of the system with integrated calibration is provided, including the main

components, the operational procedure, a mathematical model and the control system design. In the fourth chapter, the measurement uncertainty for the components of the transducer are evaluated and uncertainty budgets for the force and torque measurements with the multicomponent transducer are described. In the fifth chapter, verification measurements are shown, where the results provided by traditional calibration procedures are compared with the integrated calibration. In the sixth chapter some applications for the system are shown, including the identification of multicomponent transducers, the Lorentz force velocimetry and micromachining. In the last chapter a conclusion with the main results of this work is provided. In appendix A a list of commercially available off-the-shelf (COTS) products used to obtain the results shown here is provided and appendix B contains a list of some terms and definitions used.

CHAPTER 2

REVIEW OF THE STATE OF ART

In this chapter, systems used for the force measurement and weighing technology are described with the respective measuring ranges and achievable measurement uncertainties. A description of multicomponent force and torque transducers is also provided with information about different implementations and calibration methods used, including the limitations of the procedures and achievable measurement uncertainties. The principle of the Kibble balance is described, the advantages of the method are mentioned and the measurement uncertainties that can be achieved are shown. Considerations for precision scales and Kibble balances are mentioned, including information about measurement procedures and relevant design aspects.

2.1 FORCE MEASUREMENT AND WEIGHING TECHNOLOGY

There are several principles for the measurement of forces and torques available in the literature. A description of force transducers is provided in [1, 10], including measurements based on electrical resistance, inductance, capacitance, optical interference, photoelasticity, hydraulic conversion, piezoelectric/magnetostrictive transduction, electromagnetic/electrostatic force compensation and vibrating wires or resonators. Figure 2.1 shows the measuring ranges and achieved uncertainties for measuring forces with the electromagnetic and electrostatic force compensation, strain gauges and the comparison with masses. This graph considers different systems available in the literature and a similar diagram is provided in [31].

The electromagnetic force compensation (EMFC) is a method which dates back to at least 70 years [32, 33] and is used in high precision balances. Figure 2.2 shows a weighing cell which implements this principle. It is composed by a parallel spring mechanism attached to a lever by a coupling band. An electromagnetic actuator with a coil and a magnet system with a permanent magnet are attached to the lever. An aperture slit position sensor is used to measure the angle of the lever and a counterweight is used to generate an offset force. The aperture slit position sensor contains an LED and a dual photodiode which are not shown in this figure. By using the position from the aperture slit position sensor, the force generated by the electromagnetic actuator and a control system, it is possible to compensate the weight force of the test mass applied to the weighing pan and control the angle of the lever to any desired level. Assuming the actuator constant

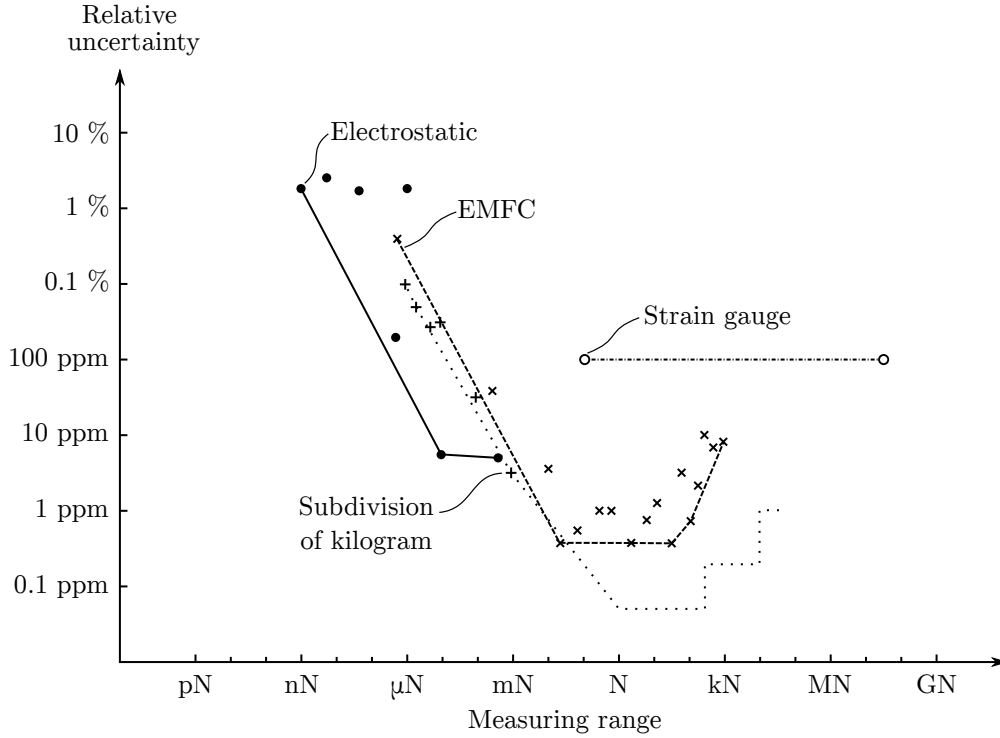


FIGURE 2.1: Methods for measuring forces and associated ranges with achievable relative standard uncertainties.

is known, the force generated by the electromagnetic actuator can be determined by measuring the electric current flowing in the coil. Commercial products can be found in a range from 10 mN up to 700 N. With these devices, it is possible to perform measurements with a relative uncertainty lower than 1 ppm for a force range between 20 mN and 50 N¹. Balances with a measuring range higher than 50 N exhibit larger linearity errors and, for this reason, the force measurement is performed with larger uncertainties. In [34] a microbalance was used to measure forces in a range between 0.5 μN and 0.2 mN with relative standard uncertainties of 0.44 % and 0.005 % respectively.

For measuring forces in a range between 1 nN and 0.2 mN, the smallest uncertainties are typically achieved with the electrostatic force compensation. There are several works in the literature that make use of this principle [31]. With the electrostatic force balance of the National Institute of Standards and Technology (NIST, United States of America) [35] it is possible to measure forces between 10 μN and 0.2 mN with relative standard uncertainties smaller than 8 ppm. The nanonewton force facility [36] of the Physikalisch-Technische Bundesanstalt (PTB, Federal Republic of Germany) can be used to measure forces between 1 nN and 1 μN with relative uncertainties below 3 %. Other devices developed in the Industrial Technology Research Institute (ITRI, Republic of China) [37], in the Tianjin University (People's Republic of China) [38] and also at NIST [39] use the electrostatic force compensation as well to measure small forces.

¹In order to estimate the achievable uncertainty for the measurement, the linearity error specified in the datasheet of the devices was used.

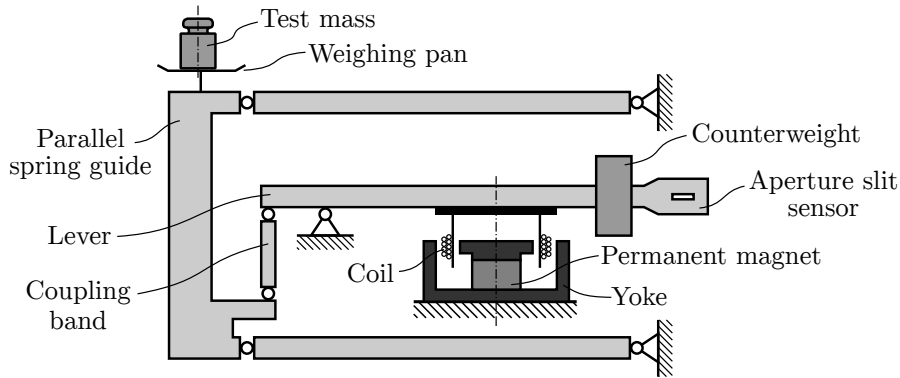


FIGURE 2.2: Electromagnetic force compensation principle used in a weighing cell.

The smallest relative uncertainties for generating forces in a range starting from 0.1 N are achieved by using mass artifacts. These uncertainties are shown in figure 2.1 and are identified as “subdivision of kilogram”. For forces between 10 μ N and 50 kN weights determined by the international recommendation OIML R 111-1 [40] of the International Organization of Legal Metrology can be used. Weights of class E1 can be used to generate forces in range from 10 μ N to 500 N, weights of class E2 can be used to generate forces in a range from 1 kN to 10 kN and weights of class F1 can be used to generate forces in a range from 20 kN to 50 kN. The forces generated by single weights only are listed here and higher forces can be generated by the combination of various weights. It is also possible to generate smaller forces by using weights of classes E2 and F1, but the associated uncertainties are higher. By using E1 weights for the calibration of force and mass measuring instruments, uncertainties smaller than 0.1 ppm can be achieved.

Applications of strain gauge force transducers can be found in a range from 0.1 N to 50 MN. There are different types of strain gauge transducers, including foil gauges, semiconductor gauges and thin film gauges. These principles are used to measure forces in ranges of 5 N to 50 MN, 1 N to 10 kN and 0.1 N to 100 N [41]. Relative measuring uncertainties down to 0.02 % can be achieved with strain gauge force transducers. It is important to observe that the uncertainties listed here are for the measurement of forces in the vertical i.e. gravity acceleration direction.

Torque is a quantity related to the force and similar methods can be employed for the measurement. There are also systems based on the measurement of deformations with strain gauges and the electromagnetic force compensation [42]. Torques generated by forces applied with a lever have the additional difficulty of the determination of the length associated to the lever. For this reason, torques are usually associated to measurement uncertainties higher than forces. The direction of the torques generated by deadweight machines is related to the gravity acceleration direction, which is vertical. For this reason the torques are originally generated in the horizontal direction and, if a torque in the vertical direction is desired, it is necessary to use mechanisms with pulleys or levers.

In this section, basic principles for measuring forces were described and the achievable measuring uncertainties with systems available in the literature were

shown. In the next section, a review on multicomponent transducers is provided, which are devices used to measure forces and torques in more than one component simultaneously.

2.2 MULTICOMPONENT FORCE AND TORQUE MEASUREMENT

For some applications it is desired to measure more than one component of force and torque vectors simultaneously and, in this case, multicomponent transducers can be used. In this section, information about working principles and possible realizations for such systems is provided. After that, a review on the calibration methods available in the literature is given.

2.2.1 MEASURING SYSTEMS

Most of the multicomponent force and torque transducers available in the literature are based on compliant mechanisms with strain gauges. A comprehensive analysis of such systems has already been performed in [12], with details about the working principle of strain gauges and several implementations of multicomponent transducers with structures of different types. An evaluation of the performance of strain gauge transducers has already been performed in [11]. This includes different details like the materials used for the compliant mechanism and nonlinearities originated by the gluing of the strain gauges, or the strain gauges itself.

A multicomponent transducer based on the electromagnetic force compensation principle was presented in [12]. This transducer has several advantages when compared to methods based on the measurement of deformations with strain gauges. There is no displacement of the sensing element during the force measurement, the system exhibits a more robust behavior and a better resolution for both force and torque measurements can be achieved. This system is a basis for the transducer developed in the present work.

2.2.2 CALIBRATION SETUPS

Several calibration setups for multicomponent force and torque transducers have been presented in the literature. For instance, the Physikalisch-Technische Bundesanstalt (PTB) in Germany has published two calibration setups [13, 43] used for calibrating multicomponent transducers. The first system can be used to calibrate six component force and torque transducers and has a measuring range of up to 10 kN for the forces and 1 kN m for the torques. With this system it is possible to measure forces and torques with a relative expanded measurement uncertainty ($k=2$) of 2.2×10^{-4} . Figure 2.3 shows a schematic diagram with this system. It is composed basically by a hexapod-structured reference force and torque measurement system, the test transducer (device under test), a hexapod actuator and a linear guide to adjust the system to different transducers. The

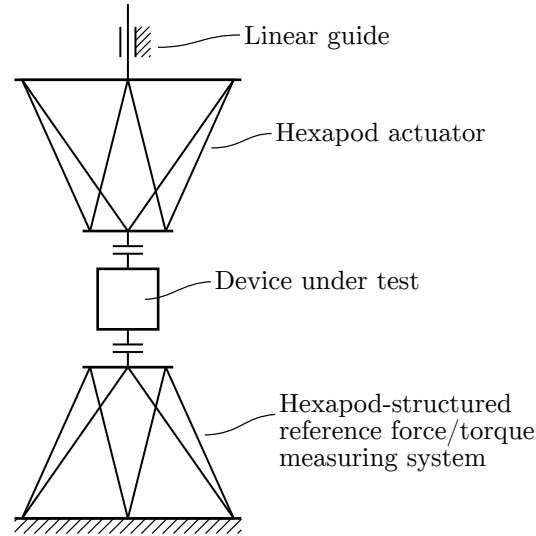


FIGURE 2.3: Hexapod-structured calibration device for multicomponent force and torque transducers (PTB-6) [13].

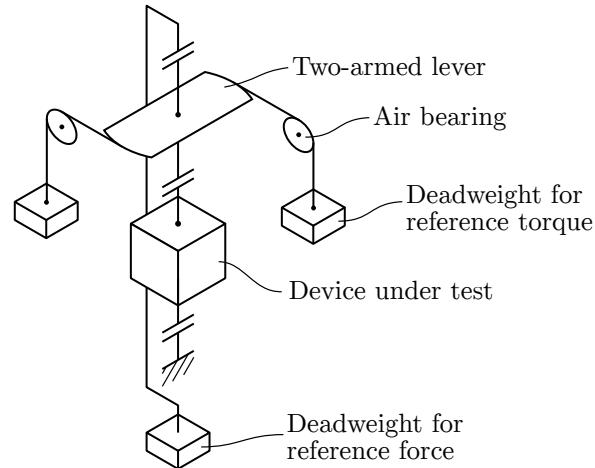


FIGURE 2.4: 2 kNm torque standard machine for superposition with axial forces up to 1 MN (PTB-2) [43].

multicomponent test transducer is fixed to the actuator and the reference transducers. With the hexapod actuator it is possible to generate force and torque vectors. These forces and torques are measured by using the reference transducers and the device under test. In this way the results provided by both transducers can be compared and the test transducer can be calibrated.

The second system published by the PTB is a deadweight force/torque standard machine and can be used to calibrate two-component systems. It has a range from 20 kN to 1 MN for the force component and 20 N m to 2 kN m for the torque component. By using this device, transducers can be calibrated with expanded relative uncertainties ($k=2$) of 2×10^{-5} and 3.9×10^{-4} for forces and torques respectively. A schematic diagram of this system is shown in figure 2.4. It is a deadweight machine composed by separated load stacks for the forces and the torques. Pressure forces and torques in the clockwise direction can be generated simultaneously. The forces are generated by a load stack and the torques

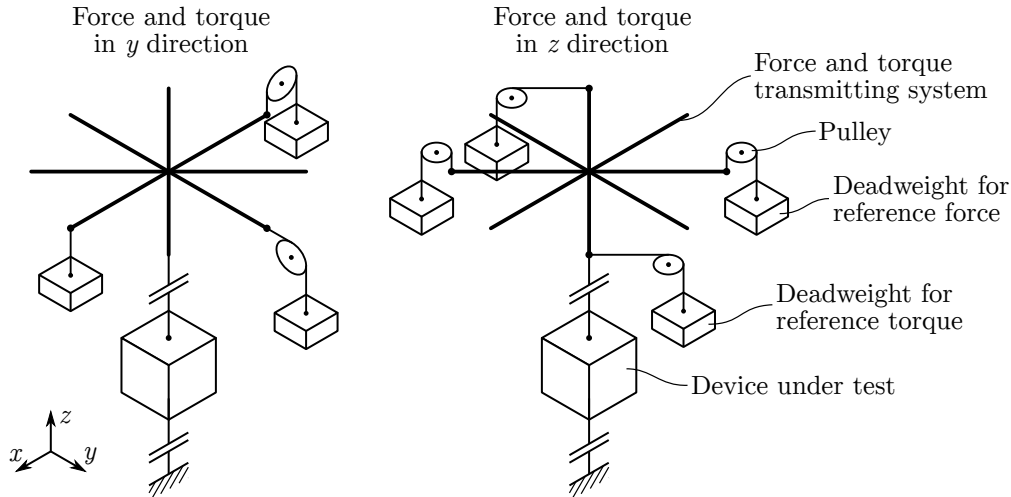


FIGURE 2.5: Six-component force/torque transducer testing machine (GNU) [45].

are generated by two load stacks associated to a two-armed lever system with air bearings. In the figure, the load stacks are indicated by simple deadweights.

Other works have addressed the calibration of multicomponent force and torque transducers in different measuring ranges. For instance, Ferrero et al. [44] have developed a six-component system that operates with forces up to 105 kN and torques up to 2 kN m. This is a deadweight-based multicomponent standard machine that uses different mechanisms based on levers to generate the forces and torques in the desired directions. Kim et al. [45] have developed a system that generates forces and torques in ranges of 50 N to 500 N and 5 N m to 50 N m respectively. This is also a deadweight standard machine and it is basically composed by a transmitting system with levers to generate forces and torques in three orthogonal directions simultaneously. Forces and torques in both positive and negative directions can be generated. The working principle of this system is shown in figure 2.5. On the left-hand side of this picture the system is used to generate a force and a torque component in the y direction and on the right hand side the system is used to generate a force and a torque component along the z direction. There are load stacks of deadweights for all directions and, in the figure, the load stacks are represented by simple weights. This figure is a simplified version of the system and only the weights and components necessary to generate the forces/torques in the respective directions are represented.

At the NASA Langley Research Center different calibration setups have been designed as well. The Single-Vector Force Balance Calibration System (SVS) can be used to calibrate six-component transducers and generate forces and torques up to 700 N and 28 N m respectively [46]. This system is shown in figure 2.6. With this system a single weight stack is used to generate a combined force and torque vector. Since the forces and torques are generated by using the local gravity acceleration, the force vector is always vertical, i.e. parallel to the gravity direction, and the torque vector is always horizontal, i.e. orthogonal to the gravity direction. The orientation system is used to change the orientation of the test transducer in space and with the force and torque generation system it is

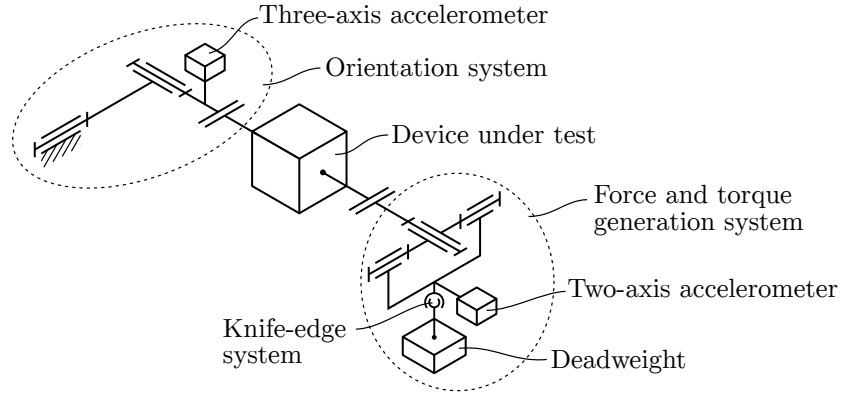


FIGURE 2.6: Single-Vector Force Balance Calibration System (NASA-SVS) [46, 47].

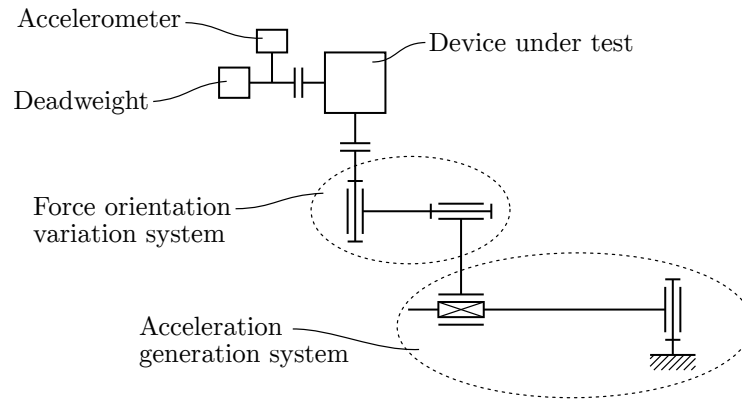


FIGURE 2.7: Variable Acceleration Force Calibration System (NASA-VACS) [48].

possible change the magnitude and position of the applied force. The three-axis accelerometer is used to measure the orientation of the multicomponent transducer in space. This information is used to determine the relative direction of the force applied to the transducer. The two-axis accelerometer is used to determine the orientation of the force and torque generation system in space. In this way, the position of the force applied by the load stack can be determined. This information is used to determine the magnitude and direction of the torque applied to the transducer. Since the geometry of the force and torque generation system is not symmetric, positioning errors cause different achievable uncertainties for measuring the torques in different directions. For this reason the torque in x direction has the highest uncertainty.

The Variable Acceleration Force Calibration System (VACS) can be used to generate forces and torques up to 130 N and 13 N m respectively [48]. This system is shown in figure 2.7. This machine is also based on deadweights. The reference forces and torques are generated by the gravity acceleration and the centrifugal acceleration caused by a rotational system. By changing the rotational velocity and the distance between the deadweight and the rotational axis it is possible to change the magnitude of the force generated by the centrifugal acceleration. The force orientation variation system is used to change the orientation of the test transducer in space and, in this way, change the direction of the force and torque

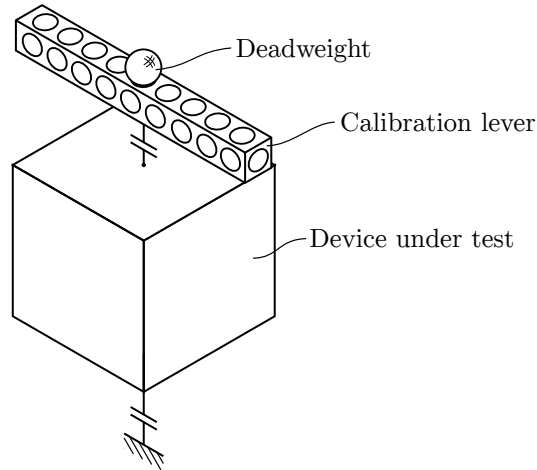


FIGURE 2.8: Multicomponent calibration setup with lever and multiple mass positions (TU Ilmenau) [12].

applied to the test transducer. By changing the direction and magnitude of the force applied to the transducer, the magnitude of the torque can be changed as well. The accelerometer is used to determine the orientation of the test transducer in space.

For forces and torques in the range of 0.6 N and 31 mN m a calibration setup was designed at the Technische Universität Ilmenau [12]. With this system it is possible to generate forces and torques with a relative expanded uncertainty ($k=2$) of 2.1×10^{-4} and 4.7×10^{-3} respectively. This system uses a calibration lever with defined positions. By placing a stainless steel sphere with known mass and density in different positions it is possible to generate defined forces and torques. The magnitude of the force is determined by the weight of the sphere. The magnitude of the torque depends of the weight and position of the sphere. By sequentially changing the orientation of the transducer in space it is possible to change the relative direction of the force applied and calibrate all components of the transducer successively.

Table 2.1 shows these systems with the respective relative expanded ($k=2$) measurement uncertainties that can be achieved for both force and torque measurements [26]. A common fact for all systems mentioned here is that the forces and torques are realized either by deadweights or by calibrated force/torque transducers. For the systems based on deadweights there is an additional difficulty to apply horizontal forces, which are normally generated in the vertical, i.e., gravity acceleration direction. In this case, it is necessary to use additional mechanisms with levers, bearings or pulleys, to conduct the forces, or rotate the force transducer in order to align the direction to be calibrated with the gravity direction. Alternatively, the test forces by the deadweight can be generated by moving the transducer with a known acceleration along the desired direction [48]. It is also possible to overcome these difficulties by using calibrated force/torque transducers as measurement standards, which can operate in any orientation. However, the force and torque transducers are usually calibrated by using deadweight machines and limited by the uncertainties obtained with these calibration systems.

TABLE 2.1: Multicomponent calibration setups and relative expanded measurement uncertainties (k=2).

System*	F_x	F_y	F_z	M_x	M_y	M_z
PTB-2 [43]	-	-	1 MN	-	-	2 kN m
	-	-	($2.0 \cdot 10^{-5}$)	-	-	($3.9 \cdot 10^{-4}$)
PTB-6 [13]	10 kN	10 kN	10 kN	1 kN m	1 kN m	1 kN m
	($1.6 \cdot 10^{-4}$)	($1.4 \cdot 10^{-4}$)	($1.5 \cdot 10^{-4}$)	($2.0 \cdot 10^{-4}$)	($2.0 \cdot 10^{-4}$)	($1.6 \cdot 10^{-4}$)
INRiM [44]	6 kN	6 kN	105 kN	2 kN m	2 kN m	2 kN m
	($6 \cdot 10^{-4}$)	($6 \cdot 10^{-4}$)	($4 \cdot 10^{-5}$)	($1 \cdot 10^{-3}$)	($1 \cdot 10^{-3}$)	($1 \cdot 10^{-3}$)
GNU [45]	500 N	500 N	500 N	50 N m	50 N m	50 N m
	($8.6 \cdot 10^{-4}$)	($8.6 \cdot 10^{-4}$)	($1.2 \cdot 10^{-5}$)	($8.6 \cdot 10^{-4}$)	($8.6 \cdot 10^{-4}$)	($1.7 \cdot 10^{-3}$)
NASA-SVS [46, 47]	220 N	350 N	700 N	11 N m	28 N m	14 N m
	($2.0 \cdot 10^{-4}$)	($2.0 \cdot 10^{-4}$)	($1.8 \cdot 10^{-4}$)	($1.3 \cdot 10^{-3}$)	($4.6 \cdot 10^{-4}$)	($4.8 \cdot 10^{-4}$)
NASA-VACS [48]	90 N	-	130 N	-	13 N m	-
	($1.3 \cdot 10^{-2}$)	-	($7.5 \cdot 10^{-3}$)	-	($8.4 \cdot 10^{-3}$)	-
TU Ilmenau [12]	0.6 N	0.6 N	0.6 N	31 mN m	31 mN m	31 mN m
	($2.1 \cdot 10^{-4}$)	($2.1 \cdot 10^{-4}$)	($2.1 \cdot 10^{-4}$)	($4.7 \cdot 10^{-3}$)	($4.7 \cdot 10^{-3}$)	($4.7 \cdot 10^{-3}$)

*The names used in this description refer to the institutions where the systems were developed.

2.3 KIBBLE BALANCE EXPERIMENTS

A comprehensive review on Kibble balances is provided in [27]. This section is intended to give a short overview on the origin of the Kibble balance technique, the basic operational principle and the aspects relevant for the present work.

In 1976 Brian Kibble published measurement results of the gyromagnetic ratio of the proton γ'_p obtained by using an experimental setup with a beam balance [49]. With the technology of that time, the constant γ'_p could be used to measure magnetic fields B precisely and realize the SI ampere with an uncertainty of about 1 ppm. In this publication, the beam balance is used in association with a current-carrying coil to determine the magnetic field generated by a permanent magnet. This is basically done by measuring the Lorentz force caused by the interaction between the magnetic field and the electric current in the coil. The current is determined by measuring the voltage drop over a resistor with known resistance value. A water sample with protons is located in the same magnetic field. The ratio of the precession frequency of the protons, which is measured in the same experiment, to the magnetic field gives the gyromagnetic ratio of the proton γ'_p .

In the same publication, a different way of realizing the ampere unit of electric current is suggested. The idea is to use the same apparatus but with minor modifications. The gradient of the magnetic flux in the coil in a direction perpendicular to both coil and magnetic field, which is equal to the magnetic field multiplied by the length of the conductor Bl , is determined with two methods: In the first method a current flows in the conductor and both Lorentz force F and electric current i are measured. This is the same case described previously here, but the force and current information are used to determine the product Bl and not only the magnetic field B :

$$Bl = \frac{F}{i}. \quad (2.1)$$

This method is nowadays known as the weighing mode for Kibble balances. In the second method the mechanism of the beam balance is used to move the coil in the same direction as the force F generated in the first experiment. However, in this case, there is no current flowing in the coil and due to the Faraday's law of induction there is a voltage u induced in the coil, which is proportional to the velocity v . By measuring both induced voltage and velocity, the product Bl can be determined again:

$$Bl = \frac{u}{v}. \quad (2.2)$$

This method is nowadays known as the velocity mode for Kibble balances. In the original suggestion of Brian Kibble, the results of both experiments could be used in combination with an SI ohm derived from the calculable capacitor to realize the SI ampere. Since this approach does not depend on the determination of the gyromagnetic ratio of the proton, the proton sample and the system used to measure the precession frequency are not necessary. The Josephson effect [50] and the Quantum Hall effect [51], which were discovered in the years of 1962 and 1980 respectively, enabled the establishment of more stable standards for voltage and electric resistance. The combination of these effects with the principle proposed by Brian Kibble represented a new possibility to determine the Planck constant with very low uncertainties by using a macroscopic mass. This idea is described in the literature as the Kibble balance.

Figure 2.9 shows basic components of a Kibble balance. It is composed by a weighing mechanism which has a balance wheel, a knife-edge, two electromagnetic actuators with permanent magnets and a weighing pan with a mass lift. This weighing mechanism is very similar to the mechanism used in the NIST-4 Kibble balance [52]. One of the electromagnetic actuators is used to control the balance during the velocity mode and the other is used to control the balance during the weighing mode. These are the auxiliary and main actuators respectively, which contain the auxiliary and main coils shown in figure 2.9. The permanent magnet of the main actuator is designed in a way to generate a very uniform magnetic field in the position of the coil. For the NIST-4 Kibble balance, this actuator has an actuator constant of about 709 N A^{-1} . Laser interferometers are used to measure the position and angle of the main coil and electrostatic actuators are used to control the rotation of the weighing pan. The system is inside a vacuum chamber and, for the case of the NIST-4, it can operate in a pressure of about 0.1 mPa. A precise determination of the local gravity acceleration is also necessary and, for this reason, an absolute gravimeter is installed near to the instrument.

For the operation of the Kibble balance switching systems for changing between velocity mode and weighing mode are necessary. During the velocity mode the main coil is connected to a voltage measuring system with a programmable Josephson voltage standard (PJVS) and a digital voltmeter (DVM). The auxiliary coil, which is used to control the balance, is connected to a programmable current source (PCS). By using the signal provided by the laser interferometer in association with a control system, the angle of the balance wheel and the position of the main coil can be controlled to any desired level in the moving range. Since the current flowing in the auxiliary coil could generate an induced voltage in the main coil and cause a measurement deviation, it is important to have sufficient

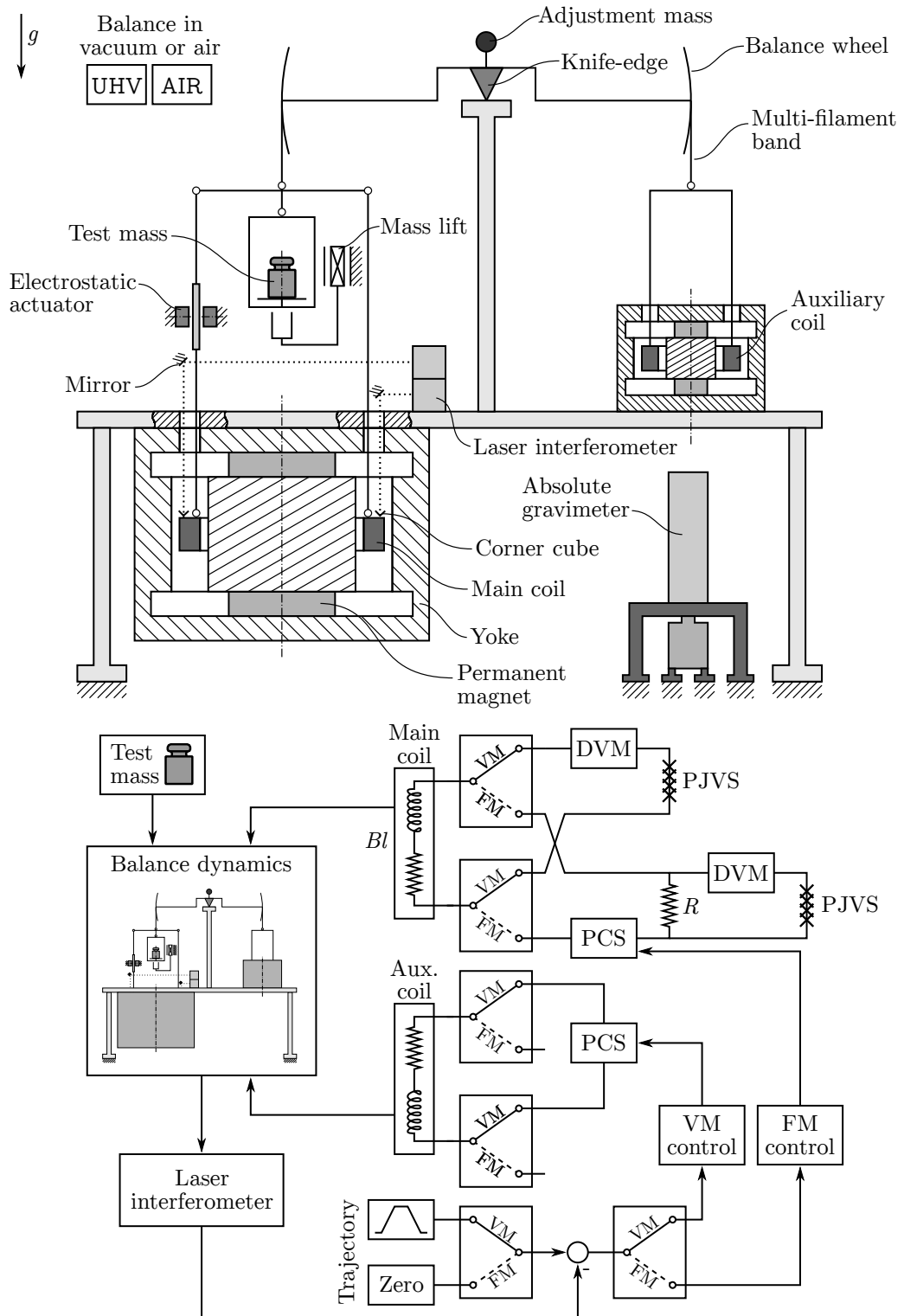


FIGURE 2.9: Example of the Kibble balance experiment.

distance between both electromagnetic actuators. During the weighing mode, the main coil is connected to a programmable current source in series with a reference resistor R . By measuring the voltage drop u_R over this resistor with a programmable Josephson voltage standard and a voltmeter it is possible to precisely determine the current i flowing in the main coil. The position of the coil is also controlled by using a feedback strategy with the signals provided by the laser interferometers but, in this case, the position is kept constant.

By using the local value for the gravity acceleration obtained with the absolute gravimeter in combination with equations (2.2) and (2.1) it is possible to obtain the following expression:

$$m = \frac{1}{g} \frac{u_R u}{R v}, \quad (2.3)$$

which relates the mass measurement with the measurement of electrical voltage, resistance, velocity and acceleration. In this work the same idea is applied to the force and torque measurements but, in this case, the determination of the local gravity acceleration is not necessary as described in the next section.

There are several aspects of the Kibble balance that must be regarded for the traceable mass measurement. There is a small difference in the value of the actuator constant determined during the velocity mode and the value determined during the weighing mode. This difference is caused by the currents flowing in the coil during the weighing mode, which change the magnetic field generated by the permanent magnet. This is known in the Kibble balance literature as the coil-current effect [53]. During the velocity mode, if the coil is not moved in a precise linear trajectory, voltages are induced in the coil due to movement components in other directions. These induced voltages cause a deviation in the measurement of the actuator constant and are not desired. These deviations are known in the Kibble balance literature as the coil-motion effects [54]. Similar problems are present in the multicomponent transducer presented here and these aspects must be regarded for the force and torque measurement as well.

Several laboratories worldwide are implementing the Kibble balance technique, including the the Bureau International des Poids et Mesures (BIPM) [55, 56], the Korea Research Institute of Standards and Science (KRISS) [57], the Laboratoire National de Métrologie et d'Essais (LNE) [58], in France, the Federal Institute of Metrology (METAS) [59], in the Swiss Confederation, the Measurement Standard Laboratory of New Zealand (MSL) [60], the National Institute of Metrology (NIM) [61], in the People's Republic of China, the National Institute of Standards and Technology (NIST) [62], in the United States of America, the National Physics Laboratory (NPL) [63], in the United Kingdom, the National Research Council (NRC) [64], in Canada and the Ulusal Metroloji Enstitüsü (UME) [65], in Turkey. The NRC and the NIST have published the results for the determination of the Planck constant with lowest uncertainty by using the Kibble balance. These laboratories have achieved uncertainties of about 9 ppb [30] and 13 ppb [29] respectively.

The Planck-Balance [66] is a device based on the Kibble balance principle and is being developed at the Technische Universität Ilmenau in cooperation with the Physikalische-Technische Bundesanstalt. The main purpose of this device is the realization of the kilogram unit after the redefinition of the SI. There are two

versions of this balance being developed: the PB-2 which is intended to be used for calibrating weights of class E2 and the PB-1 which is intended to be used for calibrating weights of class E1.

The use of the Kibble balance principle for the force and torque measurement has several advantages. It is not necessary to use mass prototypes to calibrate the transducers, the presence and determination of the local gravity acceleration is not necessary, the transducer can be calibrated in any orientation in space and the calibration procedure is more practical and can be integrated in the force and torque transducer. Furthermore, this principle has the potential to reduce the uncertainty for both force and torque measurements.

CHAPTER 3

DESCRIPTION OF THE INSTRUMENT

In this chapter, a description of the system and its components is provided, a mathematical model is derived and the control system design is explained. The description of the system considers the main components of the instrument and its operational procedure. Under the assumption of rigid body behavior, a mathematical model is derived. This model is used for the control system design and the uncertainty analysis for both force and torque measurements.

3.1 MAIN COMPONENTS AND OPERATION

The main component of the system is a levitating servo controlled element with six position sensors and twelve voice coil actuators attached to it (figure 3.1). The voice coil actuators are divided in two groups of six actuators each: coils I and coils II. The system has also two operating modes, called the calibration mode and the sensing mode. By using a multi-input multi-output (MIMO) control system, the signals from the six position sensors and the forces generated by six voice coil actuators of one group, it is possible to control the position and angle of the sensing element to any desired level inside the range of motion. In the calibration mode, coils II are used to generate the control forces and sine wave reference trajectories are used for the position and angles. The use of a sine wave as reference trajectory during the calibration mode has already been described in [60,

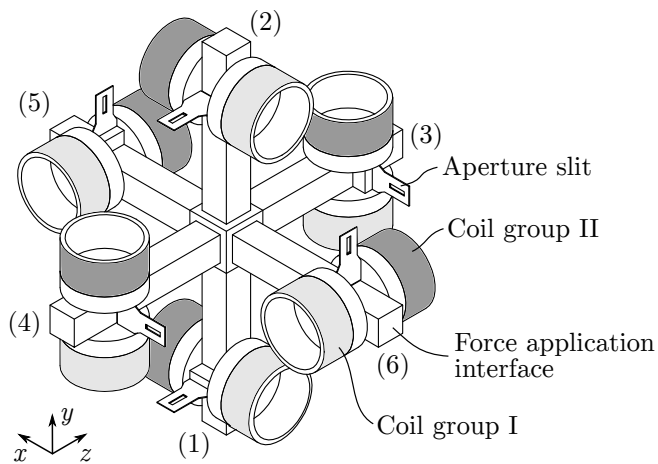


FIGURE 3.1: The sensing element with the coils of the actuators and the aperture slits.

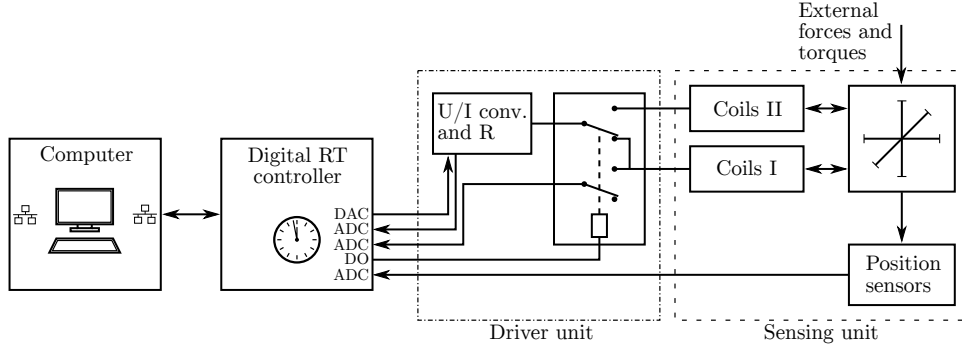


FIGURE 3.2: System plan with the main components. The dashed line represents the sensing unit of the transducer, with the sensing element, the position sensors and the coils, and the dash dotted line represents the driver unit, with U/I converters, measuring resistors and switching system. Further components of the system are the digital real-time controller and a computer.

[65, 67] for different Kibble balance experiments. In this mode, coils I are in a open circuit state and are connected to the digital voltmeters only. While the sensing element moves with the given trajectory, the voltages induced in the coils I are measured. The calibration coefficients for the force and torque measurements can be determined by using the amplitude of the induced voltages and the amplitude of the linear and angular velocities, which were measured during the velocity mode. In the sensing mode, the coils I are used to generate the control forces and the sensing element is controlled to a constant position and angle. In this mode, the coils II are used to generate an offset force that compensates the weight force of the sensing element. External forces and torques acting on the sensing element are compensated by the control system and can be determined by measuring the currents flowing in the coils I and using the calibration factors determined in the calibration mode. A six coil system that operates only in the sensing mode was already described in [12, 68]. The system described in this work was initially designed to measure forces and torques in a range of $\pm 2 \text{ N}$ and $\pm 0.1 \text{ N m}$ respectively with a maximal relative expanded measurement uncertainty ($k=2$) of 1×10^{-4} . In order to achieve this uncertainty, all components of the system (figure 3.2) have to fulfill specific requirements of stability and linearity and some of them need to be measured traceable to the SI. This includes the position sensors, the resistance standards, voltage measuring systems and time reference. An evaluation of the achievable measurement uncertainty and a verification of these results are provided in chapters 4 and 5 respectively.

Figure 3.2 shows all components of the transducer, including the computer, the digital real-time controller, the driver unit and the sensing unit. The driver unit contains the voltage-to-current (U/I) converters, measuring resistors, the switching system and the interfaces to sensing unit and computer. The sensing unit contains the sensing element, the voice coil actuators, the position measuring system and the interfaces to the driver unit and the force/torque application. It also contains a temperature measuring system for the magnet system, an air pressure measuring system and a relative humidity measuring system, which are

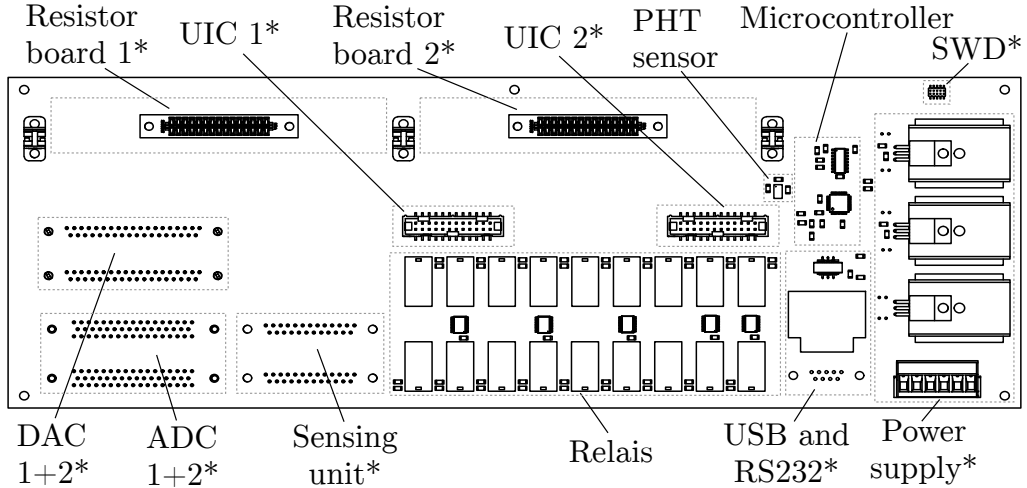


FIGURE 3.3: Main board of the transducer's driver unit. Components indicated with an asterisk represent connectors.

not shown in the figure.

The digital real-time controller is equipped with a 64-bit processor, two 16-bit analog-digital conversion modules with 16 channels each, two 16-bit digital-analog modules with 6 channels each and a digital board with 96 general purpose inputs/outputs. These components are listed in appendix A, as CPU-B, ADC-B, DAC-B and GPIO-B respectively. The controller communicates with the computer through an optical cable interface. With the computer it is possible to program the controller, control the measurements and fetch the measurement data from the controller. Both real-time computer and controller are commercially available off-the-shelf products. The driver unit and the sensing unit are development of the Technische Universität Ilmenau. In the next subsections more details about these components are provided. Additionally, more details about the control system operational procedure are provided later.

3.1.1 DRIVER UNIT

The task of the driver unit of the transducer is to provide the following functions to the system:

- Interface between the real-time digital controller and the sensing unit
- Voltage to current conversion to drive the actuators
- Current to voltage conversion for the measurement of the electric current in the actuators
- Temperature, air pressure and humidity monitoring
- Power supply and voltage regulation for some components of the system
- Switching system for changing between calibration mode and sensing mode

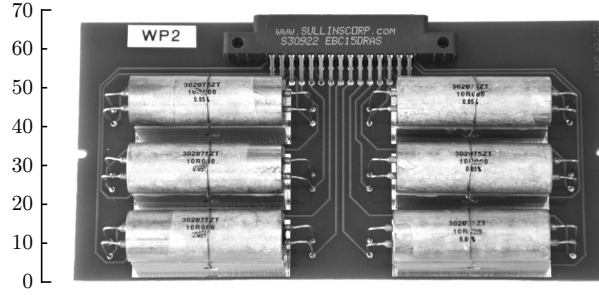


FIGURE 3.4: Resistor board used for the current measurement.
The ruler in the left hand side shows the length in millimetres.

The driver unit was designed by using a modular concept with the objective to simplify the assembly process of the transducer, possible system upgrades and the system maintenance. All components are attached to the main board of figure 3.3. That includes two voltage to current conversion modules with 6 converters each, two resistor boards with six precision resistors each, the DAC and ADC modules of the real time controller, the sensing unit of the transducer and the power supply. Additionally, the main board of the driver unit includes the switching system with 18 relays, a pressure-humidity-temperature (PHT, appendix A) sensing component, USB/RS232 communication interface and a microcontroller. The microcontroller is responsible for the serial communication of the driver unit and sensing element with the real-time controller, for the control of the switching system, and for fetching the temperature, pressure and humidity measurements from the PHT sensor.

Two pluggable resistor boards with six precision resistors each are used for measuring the electrical current in the twelve voice coil actuators. Hermetically sealed foil resistors with 4 terminal lead are used (PFR, appendix A) in this boards. With the objective to simplify the calibration of the resistors, pluggable boards are used. These boards were designed and assembled following guidelines of the manufacturer. One of these resistor board is shown in figure 3.4. The calibration of such resistor board is described in section 4.3.

The 2-pole relays used in the switching system are a special version with low thermal electromotive force (RLY, appendix A). Several investigations and comparisons with other relays were performed with these components to evaluate their performance. The results are shown in [69] and the relays used in this work exhibit the best performance achieved. The system contains 18 relays, thereof 12 are used to connect the voice coil actuators to the voltage-to-current converters and 6 are used to connect the coils of group I or II to the voltage measuring system with six analog-to-digital converters. The voltage-to-current converters used in this work are the same as used in [12] but with minor changes performed in order to improve the robustness of the system. In the modified version, possible short-circuit points present on the first version of the converter were eliminated. These U/I converters are grouped in two modules with six converters each. In this way, the twelve voice coil actuators of the sensing unit can be simultaneously used.

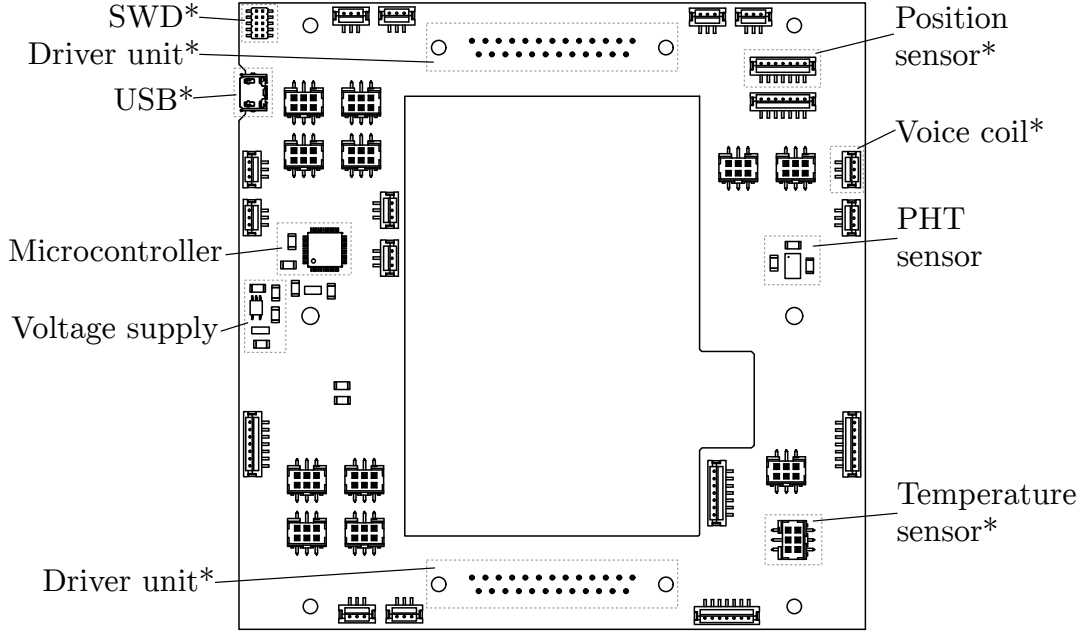


FIGURE 3.5: Main board of the sensing unit of the multicomponent transducer. Components indicated with an asterisk represent connectors.

3.1.2 SENSING UNIT

The sensing unit contains the sensing element shown in figure 3.1, the magnet systems of the electromagnetic actuators, the electronics for the position measurement system, 12 temperature sensors for the magnet systems and a sensing module for air pressure, humidity and temperature (PHT, appendix A). The components of the sensing unit are inside a cube-shaped aluminum frame and attached to the main board shown in figure 3.5.

The voice coil actuators of the sensing unit are based on a commercial system already used in a previous version of the multicomponent transducer [12] (VCA, appendix A). During some preliminary investigations performed with these commercial actuators two major improvement possibilities were identified: the actuator constant of about 4.5 N/A could be increased to 21 N/A by reducing the wire diameter and raising the number of turns in the coil; by changing the material of the coil form from aluminum to a non-conducting material the voltage noise induced in the coil could be drastically reduced. By increasing the actuator constant of the actuators, the amplitude of the voltages induced in the coils during the calibration mode could be increased. In this way, for a voltmeter with a given absolute measurement resolution, the relative resolution for the voltage measurement can be reduced. The new coils manufactured have about 700 turns of insulated copper wires with 80 μm diameter and polyoxymethylen forms. The coil DC resistance is about 190 Ω . The magnet system of the actuators contain NdFeB permanent magnets. Although the original magnet systems from the commercial actuators were used in this transducer, similar magnet systems compatible with the coil were designed, manufactured and tested. Gold wires

with 25 μm diameter are used to conduct the electrical current from the transducer frame to the electromagnetic actuators. The wire diameter was chosen in a way to minimize the stiffness caused by the gold wires and to allow the maximal current of 100 mA for each actuator. This procedure is described with details in subsection 3.2.6.

Since the strength of the magnetic field generated by the permanent magnets depend on the temperature, a temperature sensor for each permanent magnet was integrated in the multicomponent transducer. With the digital temperature sensors used (TPS, appendix A) the temperature of the magnet systems can be measured with an uncertainty of 0.1 $^{\circ}\text{C}$ and a resolution of 0.01 $^{\circ}\text{C}$, as specified in the component datasheet. The PHT sensor used is the same as in the main board of the driver unit.

The position and angle measuring system has six aperture slit displacement sensors. Each displacement sensor is composed by the aperture slit, an LED and a differential photodiode [70]. The LED and the differential photodiode used are shown in appendix A as LED-PS and DPD-PS respectively. Both LED and photodiode are fixed to the frame of the transducer and the aperture slit is attached to sensing element. The displacement of the aperture slit can be determined by measuring the intensity of the light in each receiver of the photodiode. This is done by measuring the output currents of both receivers. An electronic with a transimpedance amplifier, which is integrated in the sensing unit of the multicomponent transducer, is used to accomplish this task. This electronic was designed at in the Institute of Process Measurement and Sensor Technology of the Technische Universität Ilmenau.

3.1.3 TRANSDUCER FUNCTIONALITY

The only mechanical connection between the sensing element and the transducer rack is given by the wires used to conduct the electric currents to the actuators. As shown in subsection 3.2.6, these wires are responsible for a very small stiffness in the system. As observed in section 3.2, for a stiffness equal to zero the system has all poles in the origin of the complex plane. Physically that means a system without a defined asymptotically stable state or configuration. This is not common for force and torque transducers, that usually have a transfer function with a defined compliance and damping, which define a stable rest state. When all power amplifier are in off state, the sensing element does not levitate and rests in a position touching the rack of the transducer. Another relevant point is that, depending on the application of the transducer, some components or modules may be added to the sensing element in order to perform the measurement task. These components change the mass, the inertia torque and the position of the center of mass of the force transducer. These quantities are therefore unknown before the transducer is started. In order to turn the transducer on and bring it to normal operation state, a system activation routine should be executed which is based on the following steps:

- Load a control gain set which is robust enough to bring the sensing element to the levitating state, also when some additional mass changes its characteristics or an external force or torque is being applied to the system.

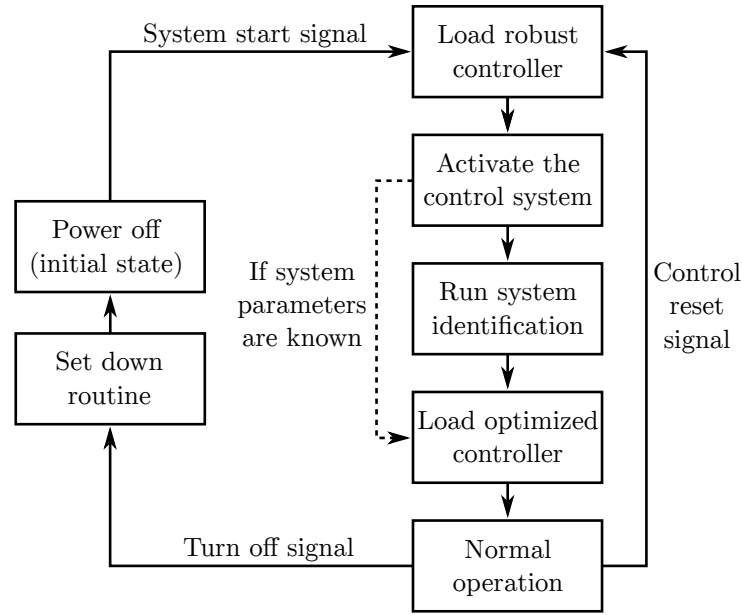


FIGURE 3.6: Control system activation routine used to levitate the sensing element and bring the transducer into operation.

- Activate the control system and enable the output stage for the six voice coil actuators. By doing so, the poles of the transducer are changed, and depending on the structure of the control system some poles are even added, in a way to define an asymptotically stable state. The system stabilizes at the home position, where all displacement sensors have an output voltage of zero volts.
- Run the system identification task to determine the mass, inertia torques and position of the center of mass of the sensing element. If these parameters are already known, it is not necessary to run the system identification task.
- Load a new set of control settings for standard operation. These control settings depend on the load state of the sensing element and should be designed in a way that the system's sensitivity against mechanical disturbances is minimized, while its dynamic response remains compatible with the application requirements.

The task-flow of the system activation routine is shown in figure 3.6. There are two type of trigger signals that are responsible for executing this routine: the system start signal and the control reset signal. For the system activation routine two control systems must be designed and implemented: a robust control for system initialization and an optimized control for the force/torque measurement task. This problem is addressed in section 3.3, where for a single control structure two sets of parameters determined. These sets correspond to the robust and optimized variations of the control system. A system identification routine responsible for determining the position of the center of mass, the inertia torques and the mass of the sensing element should be implemented as well. This problem is addressed in section 3.3.4. In order to turn the system to power off state, when all actuators are deactivated, a turn off signal has to be released. This

signal executes the set down routine, which softly sets the sensing element down and turn off the actuators. For both control design and system identification a mathematical model is used. In the next section a description for this model is provided.

3.2 MATHEMATICAL MODEL

A mathematical model for the transducer is derived which can be used for the simulation of system behavior, control system design, system identification, uncertainty analysis and identification of improvement possibilities by means of design changes. This model is basically composed by the mechanical hardware of the transducer, the voice coil actuators and the position sensors. In this section mathematical models for these components are provided and some further considerations are mentioned. Initially, generic non-linear models are derived and, under some specific assumptions, simplified linear versions for the models are provided. At the end of this chapter a linear state-space model for the transducer is shown.

3.2.1 MECHANICAL HARDWARE

Starting point for obtaining the dynamic equations for the mechanical hardware of the transducer is the application of 2nd Newton's Law for both linear and angular directions of the sensing element. Three main reference frames are defined for deriving the dynamic equations of the system: the frame A , which is fixed to the rack of the transducer, the frame B , which is fixed to the center of mass of the sensing element, and the inertial frame I . Additionally, the reference frame O is defined, which is fixed to the geometric center of the sensing element and is parallel to the frame fixed to B . This frame is used in sections 3.2.2-3.2.4 for modelling the actuators and the position sensors. Figure 3.7 shows the reference frames defined here. In previous work [12] no distinction was made between the reference frames A and I and the transducer rack was assumed to be stationary to the inertial frame. In practice, effects of ground vibrations generate accelerations in frame A and this assumption does not hold. Furthermore, in some applications the transducer can be attached to non-stationary bodies and the distinction between inertial frame and rack frame becomes more important.

The mathematical notation used to describe the model is the same as defined in [71, p. xv]. The sensing element is assumed to be a rigid body with constant mass m . The following differential equation is obtained for the linear directions considering the inertial frame I ¹:

$$\begin{bmatrix} m & 0 & 0 \\ 0 & m & 0 \\ 0 & 0 & m \end{bmatrix} {}^I \ddot{\mathbf{x}}_B = {}^I \mathbf{F}_c + {}^I \mathbf{F}_d + {}^I \mathbf{F}_g + {}^I \mathbf{F}_{ut} + {}^I \mathbf{F}_s, \quad (3.1)$$

¹This procedure is described in [71, p. 1101]. The inertial frame I defined here is equivalent to the global frame G of this literature reference.

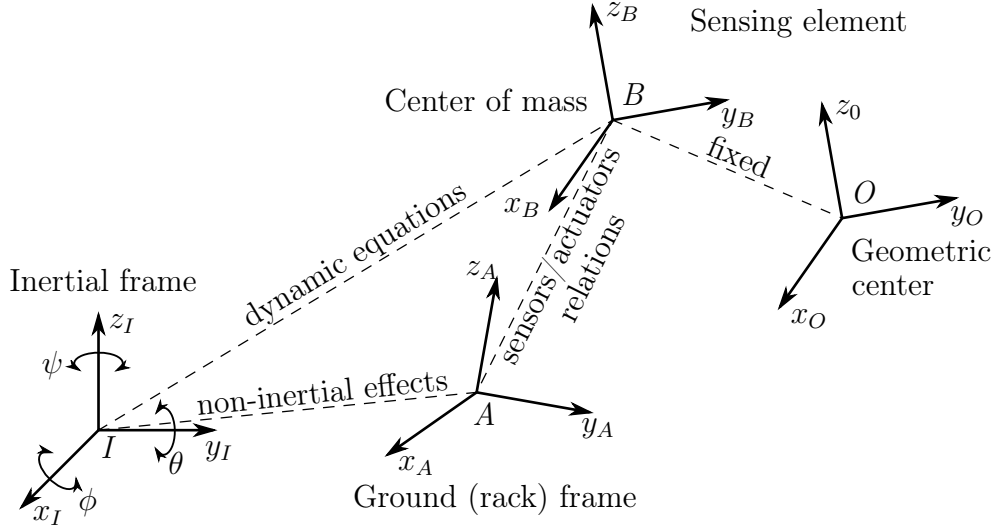


FIGURE 3.7: Reference frames used for deriving the mathematical model for the transducer.

where ${}^I\mathbf{x}_B \in \mathbb{R}^3$ is the position vector of the center of mass of the sensing element, ${}^I\ddot{\mathbf{x}}_B$ is the second derivative of this vector or the acceleration of the sensing element, ${}^I\mathbf{F}_c \in \mathbb{R}^3$ is the force vector related to the system's compliance, which is caused by the gold wires, ${}^I\mathbf{F}_d \in \mathbb{R}^3$ is the force vector related to damping, originated by air friction and magnetic effects, ${}^I\mathbf{F}_g \in \mathbb{R}^3$ is the vector of gravitational force, ${}^I\mathbf{F}_{ut} \in \mathbb{R}^3$ is the vector containing the forces generated by the actuators and ${}^I\mathbf{F}_s \in \mathbb{R}^3$ contains the disturbance forces. The left superscripts I indicate that these quantities are expressed relative to the inertial frame. For ${}^I\ddot{\mathbf{x}}_B$, the double derivative is taken in the inertial reference frame as well. Forces originally determined for the transducer reference frame B can be described in the inertial reference frame by means of the following transform:

$${}^I\mathbf{F} = {}^I\mathbf{R}_B {}^B\mathbf{F}, \quad (3.2)$$

where ${}^I\mathbf{R}_B$ is the rotation matrix. There are several possibilities to define this matrix and, in this work, it is given by three successive global rotations with angles ϕ_B , θ_B and ψ_B about the axis x_I , y_I and z_I respectively. In this way, the roll-pitch-yaw matrix is obtained [71, p. 370]:

$${}^I\mathbf{R}_B = \begin{bmatrix} c\psi_B c\theta_B & c\psi_B s\theta_B s\phi_B - s\psi_B c\phi_B & s\psi_B s\phi_B + c\psi_B s\theta_B c\phi_B \\ s\psi_B c\theta_B & s\psi_B c\phi_B + s\phi_B s\psi_B s\theta_B & s\psi_B s\theta_B c\phi_B - s\phi_B c\psi_B \\ -s\theta_B & c\theta_B s\phi_B & c\phi_B c\theta_B \end{bmatrix}, \quad (3.3)$$

where the symbols s and c correspond to the sine and cosine trigonometric functions respectively.

The rotational equation of motion for the transducer can be expressed as [71, p. 1072]:

$${}^B\mathbf{M} = {}^B\dot{\mathbf{L}} + {}^B\boldsymbol{\omega}_B \times {}^B\mathbf{L}, \quad (3.4)$$

where ${}^B\boldsymbol{\omega}_B$ is the angular velocity of the sensing element with respect to the inertial frame I and expressed in the reference frame B . The angular momentum

of the sensing element is given by:

$${}^B\mathbf{L} = {}^B\mathbf{I} {}^B\boldsymbol{\omega}_B \quad (3.5)$$

The symbol ${}^B\dot{\mathbf{L}}$ represents the time derivative of the angular momentum ${}^B\mathbf{L}$ taken in the reference frame B . The mass moment matrix ${}^B\mathbf{I} \in \mathbb{R}^{3 \times 3}$ of the transducer is determined for the reference frame B , whose origin is fixed to the center of mass, and can be expressed as:

$${}^B\mathbf{I} = \begin{bmatrix} I_{xx} & I_{xy} & I_{xz} \\ I_{yx} & I_{yy} & I_{yz} \\ I_{zx} & I_{zy} & I_{zz} \end{bmatrix} \quad (3.6)$$

Since this matrix is time-invariant, the following expression is obtained for the derivative of the angular momentum:

$${}^B\dot{\mathbf{L}} = {}^B\mathbf{I} {}^B\dot{\boldsymbol{\omega}}_B \quad (3.7)$$

With (3.5) and (3.7), the expression (3.4) can be rewritten as:

$${}^B\mathbf{I} {}^B\dot{\boldsymbol{\omega}}_B = -{}^B\boldsymbol{\omega}_B \times ({}^B\mathbf{I} {}^B\boldsymbol{\omega}_B) + {}^B\mathbf{M}_c + {}^B\mathbf{M}_d + {}^B\mathbf{M}_{ut} + {}^B\mathbf{M}_s \quad (3.8)$$

The torque vector ${}^B\mathbf{M}_c \in \mathbb{R}^3$ is related to the system's compliance and ${}^B\mathbf{M}_d \in \mathbb{R}^3$ is related to the damping torques. ${}^B\mathbf{M}_{ut} \in \mathbb{R}^3$ is the torque vector generated by the actuators and ${}^B\mathbf{M}_s \in \mathbb{R}^3$ is the total disturbance torque. By defining

$${}^B\boldsymbol{\omega}_B = [\omega_x \quad \omega_y \quad \omega_z]^T \quad (3.9)$$

the following equation can be obtained:

$$\begin{aligned} {}^B\boldsymbol{\omega}_B \times ({}^B\mathbf{I} {}^B\boldsymbol{\omega}_B) = & \\ & - \begin{bmatrix} (I_{yy} - I_{zz})\omega_y\omega_z + I_{yz}(\omega_z^2 - \omega_y^2) + \omega_x(\omega_z I_{xy} - \omega_y I_{xz}) \\ (I_{zz} - I_{xx})\omega_z\omega_x + I_{xz}(\omega_x^2 - \omega_z^2) + \omega_y(\omega_x I_{yz} - \omega_z I_{xy}) \\ (I_{xx} - I_{yy})\omega_x\omega_y + I_{xy}(\omega_y^2 - \omega_x^2) + \omega_z(\omega_y I_{xz} - \omega_x I_{yz}) \end{bmatrix} \end{aligned} \quad (3.10)$$

The differential equation that relates the angles ϕ_B , θ_B and ψ_B with the angular rotation ${}^B\boldsymbol{\omega}_B$ can be obtained through the same process described in [71, p. 385]:

$$\begin{bmatrix} \dot{\phi}_B \\ \dot{\theta}_B \\ \dot{\psi}_B \end{bmatrix} = \begin{bmatrix} 1 & \sin \phi_B \tan \theta_B & \cos \phi_B \tan \theta_B \\ 0 & \cos \phi_B & -\sin \phi_B \\ 0 & \sin \phi_B \sec \theta_B & \cos \phi_B \sec \theta_B \end{bmatrix} {}^B\boldsymbol{\omega}_B \quad (3.11)$$

The position ${}^I\mathbf{x}_A$ and rotation matrix ${}^I\mathbf{R}_A$ of the transducer frame are assumed to be predefined. The equations (3.1), (3.8) and (3.11) describe the motion of the sensing element of the multicomponent force and torque transducer. Since the range of motion in the angular directions ϕ_B , θ_B and ψ_B is smaller than 2 mrad, it is possible to perform a linearization of the dynamic equations of the system with the objective to obtain a simple model with a tolerable error. This process is described in the next section.

Model simplification for the mechanical hardware

A simple linear model for the mechanical hardware of the multicomponent transducer is desired to simplify the control design, the system identification and the analysis of the system. This model can be obtained by establishing some assumptions, performing a linearization of the equations (3.3), (3.10) and (3.11) and using the results with equations (3.1) and (3.8).

By assuming very small rotations of the reference frame B relative to the inertial frame, or in other words assuming that ϕ_B , θ_B and ψ_B are near to zero, the rotation matrix (3.3) can be written as an identity matrix and the following expression is obtained for (3.1):

$$\begin{bmatrix} m & 0 & 0 \\ 0 & m & 0 \\ 0 & 0 & m \end{bmatrix} {}^I \ddot{\mathbf{x}}_B = {}^B \mathbf{F}_c + {}^B \mathbf{F}_d + {}^B \mathbf{F}_g + {}^B \mathbf{F}_{ut} + {}^B \mathbf{F}_s, \quad (3.12)$$

Due to the symmetry of the sensing element, the components I_{xy} , I_{xz} and I_{yz} of the inertia matrix (3.6) are relatively small and can be assumed equal zero:

$$I_{xy} = 0, \quad I_{xz} = 0, \quad I_{yz} = 0 \quad (3.13)$$

Also due to the geometry of the sensing element, the components I_{xx} , I_{yy} and I_{zz} have a very similar magnitude. In this way it is reasonable to assume that the component (3.10) of the equation (3.8) is equal to zero and the following linear expression is obtained:

$${}^B \mathbf{I} {}^B \dot{\boldsymbol{\omega}}_B = {}^B \mathbf{M}_c + {}^B \mathbf{M}_d + {}^B \mathbf{M}_{ut} + {}^B \mathbf{M}_s \quad (3.14)$$

By using the same assumption of small rotations, the equation (3.11) can be written as

$${}^I \dot{\boldsymbol{\phi}}_B = \begin{bmatrix} \dot{\phi}_B \\ \dot{\theta}_B \\ \dot{\psi}_B \end{bmatrix} = \begin{bmatrix} 1 & 0 & 0 \\ 0 & 1 & 0 \\ 0 & 0 & 1 \end{bmatrix} {}^B \boldsymbol{\omega}_B \quad (3.15)$$

In order to obtain a single system of differential equations for the hole system, which will be used for the state-space representation, the following vector is defined:

$$\mathbf{x} = \begin{bmatrix} {}^I \mathbf{x}_B \\ {}^I \dot{\mathbf{x}}_B \\ {}^I \boldsymbol{\phi}_B \\ {}^I \dot{\boldsymbol{\phi}}_B \end{bmatrix} \quad (3.16)$$

with this vector the following linear state-space model that considers the six degrees of freedom of the sensing element can be obtained:

$$\dot{\mathbf{x}} = \mathbf{A}\mathbf{x} + \mathbf{B}\mathbf{u} \quad (3.17)$$

$$\mathbf{y} = \mathbf{C}\mathbf{x} \quad (3.18)$$

where $\mathbf{u} \in \mathbb{R}^6$ represents the inputs of the system and can be written as

$$\mathbf{u} = \mathbf{u}_c + \mathbf{u}_d + \mathbf{u}_g + \mathbf{u}_{ut} + \mathbf{u}_s \quad (3.19)$$

with the following components:

$$\begin{aligned} \mathbf{u}_c &= \begin{bmatrix} {}^B \mathbf{F}_c \\ {}^B \mathbf{M}_c \end{bmatrix}, \mathbf{u}_d = \begin{bmatrix} {}^B \mathbf{F}_d \\ {}^B \mathbf{M}_d \end{bmatrix}, \mathbf{u}_g = \begin{bmatrix} {}^B \mathbf{F}_g \\ \mathbf{0}_{3 \times 1} \end{bmatrix}, \\ \mathbf{u}_{ut} &= \begin{bmatrix} {}^B \mathbf{F}_{ut} \\ {}^B \mathbf{M}_{ut} \end{bmatrix}, \mathbf{u}_s = \begin{bmatrix} {}^B \mathbf{F}_s \\ {}^B \mathbf{M}_s \end{bmatrix} \end{aligned} \quad (3.20)$$

The system matrix \mathbf{A} is given as

$$\mathbf{A} = \begin{bmatrix} \mathbf{0}_{3 \times 3} & \mathbf{I}_3 & \mathbf{0}_{3 \times 3} & \mathbf{0}_{3 \times 3} \\ \mathbf{0}_{3 \times 3} & \mathbf{0}_{3 \times 3} & \mathbf{0}_{3 \times 3} & \mathbf{0}_{3 \times 3} \\ \mathbf{0}_{3 \times 3} & \mathbf{0}_{3 \times 3} & \mathbf{0}_{3 \times 3} & \mathbf{I}_3 \\ \mathbf{0}_{3 \times 3} & \mathbf{0}_{3 \times 3} & \mathbf{0}_{3 \times 3} & \mathbf{0}_{3 \times 3} \end{bmatrix} \quad (3.21)$$

where \mathbf{I}_n is an identity matrix of size n . The input matrix \mathbf{B} is given as

$$\mathbf{B} = \begin{bmatrix} \mathbf{0}_{3 \times 3} & \mathbf{0}_{3 \times 3} \\ \frac{1}{m} \mathbf{I}_3 & \mathbf{0}_{3 \times 3} \\ \mathbf{0}_{3 \times 3} & \mathbf{0}_{3 \times 3} \\ \mathbf{0}_{3 \times 3} & {}^B \mathbf{I}^{-1} \end{bmatrix} \quad (3.22)$$

The vector \mathbf{y} comprises the angle and center of mass position of the sensing element:

$$\mathbf{y} = \begin{bmatrix} {}^I \mathbf{x}_B \\ {}^I \phi_B \end{bmatrix}, \quad (3.23)$$

and the output matrix \mathbf{C} is given as

$$\mathbf{C} = \begin{bmatrix} \mathbf{I}_3 & \mathbf{0}_{3 \times 3} & \mathbf{0}_{3 \times 3} & \mathbf{0}_{3 \times 3} \\ \mathbf{0}_{3 \times 3} & \mathbf{0}_{3 \times 3} & \mathbf{I}_3 & \mathbf{0}_{3 \times 3} \end{bmatrix}. \quad (3.24)$$

In order to obtain a complete model for the transducer it is still necessary to model the forces and torques included in these equations, which are given by the vectors \mathbf{u}_c , \mathbf{u}_d , \mathbf{u}_g , \mathbf{u}_{ut} and \mathbf{u}_s . Furthermore, it is also necessary to relate the output of the aperture slit position sensors to the vector \mathbf{y} . These aspects are described in the next subsections of this chapter.

3.2.2 ACTUATORS' FORCES AND TORQUES

There are twelve voice coil actuators present in the system. Figure 3.8 shows a drawing with one of these actuators, which are basically composed by a permanent magnet, a magnetic flux guide and a coil mounted in a form. Such a voice coil actuator should ideally generate only a force component along its geometrical axis of symmetry and generate no torque component about any point over this axis. The magnitude of the force is theoretically proportional to the current. However, due to imperfections in both coil and magnetic field, in a real case

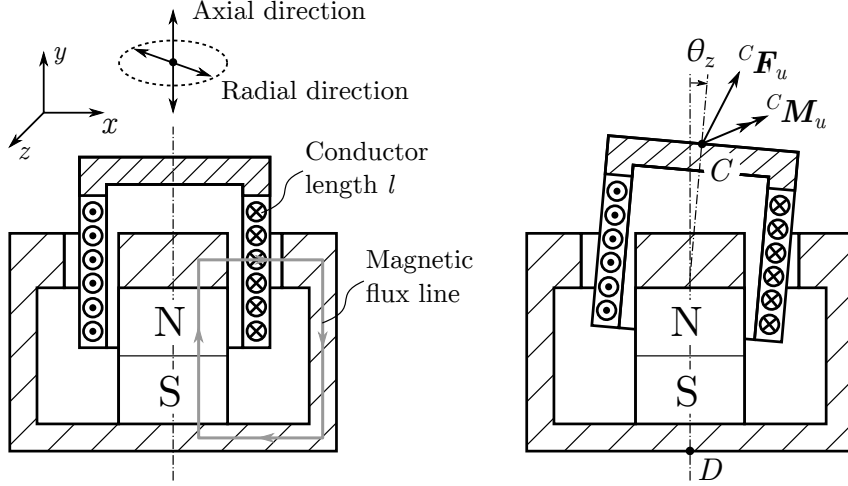


FIGURE 3.8: Cutaway drawing of voice coil actuator used in the system. In the left hand side, the actuator is shown with its permanent magnet, the magnetic flux guide and the coil. In the right hand side, the coil is rotated with an angle θ_z about the z axis. The reference points C and D , fixed respectively to the coil form and the magnet system, and the force and torque vectors generated by the coil are also indicated.

there is a force and a torque vector generated by the actuator and the magnitude of the forces and torques depend not only on the electrical current flowing in the coil, but also on the relative position and angle of the coil to the magnet system [72]. Additionally, there is a temperature dependency of the magnetic field generated by the magnetic material [73], which also affects the forces and torques. Since the current flowing in the coil also affects the magnetic field, the force and torques generated by the coil are not a simple proportional function of the electrical current. This is known as the coil-current effect [53].

The forces and torques generated by the actuators are described here as a function of the electrical current, the position and angle of the coil relative to the permanent magnet and the temperature. The directions of the forces and torques are determined initially for the reference frame C , which is stationary to the frame B . The origin of C is indicated in figure 3.8. The force generated by a voice coil is given as

$${}^C\mathbf{F}_u = F_u(i, {}^D\mathbf{x}_C, {}^D\phi_C, T_{ms}) \begin{bmatrix} f_{ux} \\ f_{uy} \\ f_{uz} \end{bmatrix} \frac{1}{\sqrt{f_{ux}^2 + f_{uy}^2 + f_{uz}^2}} \quad (3.25)$$

and the torque relative to C is given as

$${}^C\mathbf{M}_u = M_u(i, {}^D\mathbf{x}_C, {}^D\phi_C, T_{ms}) \begin{bmatrix} m_{ux} \\ m_{uy} \\ m_{uz} \end{bmatrix} \frac{1}{\sqrt{m_{ux}^2 + m_{uy}^2 + m_{uz}^2}}. \quad (3.26)$$

The magnitude of the force and torque vectors is given by $F_u \in \mathbb{R}$ and $M_u \in \mathbb{R}$ respectively and the directions are described by the coordinates f_{ux} , f_{uy} , f_{uz} ,

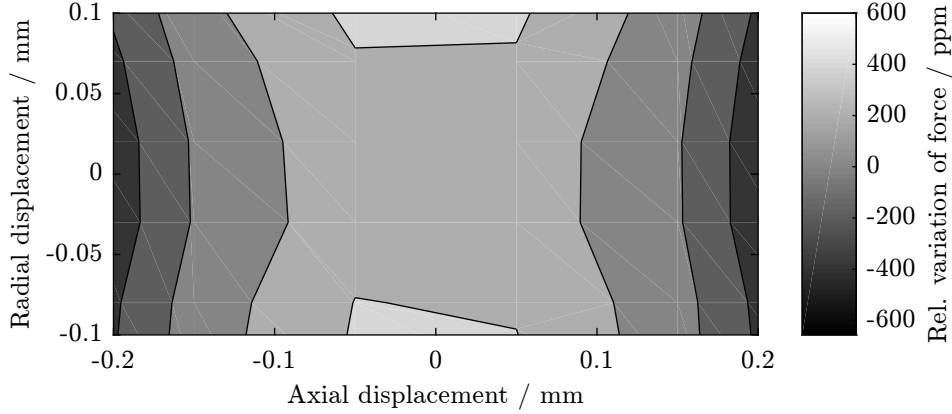


FIGURE 3.9: Magnitude of the force generated by the voice coil actuator as a function of the axial and radial position [26].

m_{ux} , m_{uy} and $m_{uz} \in \mathbb{R}$. The variable $i \in \mathbb{R}$ contains the current flowing in the voice coil actuator, ${}^D\mathbf{x}_C \in \mathbb{R}^3$ contains the position of the reference point C relative to the coordinate frame fixed to the magnet system at D and ${}^D\phi_C \in \mathbb{R}^3$ contains the angle of the coil also relative to the coordinate frame fixed to D . The temperature distribution in the magnet system is assumed to be uniform and equal to $T_{ms} \in \mathbb{R}^+$.

The position of the coil relative to the magnet system frame D is given as:

$${}^D\mathbf{x}_C = {}^D\mathbf{R}_A {}^A\mathbf{R}_I ({}^I\mathbf{x}_C - {}^I\mathbf{x}_D) \quad (3.27)$$

where the position of the point C , which is fixed to the coil, relative to the inertial reference frame is given by

$${}^I\mathbf{x}_C = {}^I\mathbf{x}_B + {}^I\mathbf{R}_B {}^B\mathbf{x}_C \quad (3.28)$$

and the position of the point D , which is fixed to the magnet system, relative to the inertial reference frame is given by

$${}^I\mathbf{x}_D = {}^I\mathbf{x}_A + {}^I\mathbf{R}_A {}^A\mathbf{x}_D \quad (3.29)$$

The relative angle ${}^D\phi_C$ is determined through the rotation matrix ${}^D\mathbf{R}_C$ according to the process described in [71, p. 435]

$${}^D\mathbf{R}_C = {}^D\mathbf{R}_A {}^A\mathbf{R}_I {}^I\mathbf{R}_B {}^B\mathbf{R}_C \quad (3.30)$$

where the matrices ${}^D\mathbf{R}_A$ and ${}^B\mathbf{R}_C$ are time-invariant, ${}^I\mathbf{R}_B$ is given by equation (3.3) and, as described in the last section, the matrix ${}^A\mathbf{R}_I$ is predefined.

Figure 3.9 shows a measurement result with the relative deviation of the force generated by a coil as a function of both radial and axial displacements. This information is used in order to determine the function F_u , which is contained in equation (3.25), for the voice coil actuators.

Equations (3.25) and (3.26) contain the force and torque generated by a voice coil actuator described in the reference frame C . Since the forces and torques in

equation (3.17) are described in the reference frame B , the following transformations are necessary:

$${}^B\mathbf{F}_u = {}^B\mathbf{R}_C {}^C\mathbf{F}_u \quad (3.31)$$

$${}^B\mathbf{M}_u = {}^B\mathbf{R}_C {}^C\mathbf{M}_u + {}^B\mathbf{x}_C \times ({}^B\mathbf{R}_C {}^C\mathbf{F}_u) \quad (3.32)$$

The rotation matrix ${}^B\mathbf{R}_C$ is used to transform a vector from the reference frame C to the frame B . It can be described in a similar way as (3.3), but in this case the transformation matrix is static. The vector ${}^B\mathbf{x}_C$ contains the position coordinates of the coil relative to reference frame B .

With the objective to obtain a relatively simple model for the system that can be used for the design of the control system and system identification, a simplified version of the model for the voice coil actuators is obtained under some assumptions.

Model simplification for the actuators

It is known that, due to the design of the voice coil actuator, the force generated in the axial direction has the highest magnitude. It is possible to assume that only a force component in this direction is generated. Furthermore, as described in [12], the position and angle dependency of the forces generated by the actuators is relatively small and can be neglected. In fact, during the sensing mode, the position and angle of the sensing element are kept constant by the control system and, in theory, there is no measurement deviation caused by this position and angle dependency. By using these assumption, the following expression for the force generated by the voice coil actuator can be obtained:

$${}^C\mathbf{F}_u = \begin{bmatrix} 0 \\ k_{Bl}(i, T_{ms})i \\ 0 \end{bmatrix}, \quad (3.33)$$

where k_{Bl} is the actuator constant of the actuator, which depend on the temperature of the permanent magnet and the current flowing in the coil. The influence of the current flowing in the coil in the actuator constant is described in the literature as the coil-current effect (section 2.3). Furthermore, for this simplified model, the torques generated by the voice coil actuator are also neglected, i.e.

$${}^C\mathbf{M}_u = \mathbf{0}_{3 \times 1}. \quad (3.34)$$

In publications about Kibble balances [27] this actuator constant is usually given as the direct product of the magnetic flux B by the conductor length l . In these balances the magnet system is designed in a way to produce a magnetic field as uniform as possible in the region occupied by the coil, and the range of motion of the coil during the velocity mode is normally several millimeters. For instance, the coil of the NIST-4 can move more than 40 mm during the velocity mode [52]. This is not the case for the magnet system used in this work, and the magnetic flux density here is not as uniform as in traditional Kibble balances. For this reason, the calibration factor of the electromagnetic actuator is given by k_{Bl} , which corresponds to the integration of a non-uniform magnetic flux density

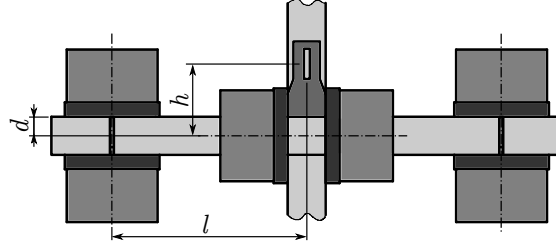


FIGURE 3.10: Dimensional parameters l , h and d of the sensing element.

B along the axial direction. Since the range of motion of the coil is much lower here ($90\text{ }\mu\text{m}$) the design requirements of the magnet system are lowered and a non-uniform B can be tolerated [26].

The sensing element of the transducer contains 12 voice coil actuators in different positions and orientations. In order to obtain the magnitude and direction of the forces and torques generated by these actuators in the sensing element, the equations (3.31) and (3.32) have to be evaluated for all coils. The total forces and torques in the sensing element are given by the following expressions:

$${}^B\mathbf{F}_{ut} = \sum_{k=1}^{12} {}^B\mathbf{F}_{uk} \quad (3.35)$$

$${}^B\mathbf{M}_{ut} = \sum_{k=1}^{12} {}^B\mathbf{M}_{uk} \quad (3.36)$$

where the vectors ${}^B\mathbf{F}_{uk}$ and ${}^B\mathbf{M}_{uk}$ represent the individual forces and torques generated by the voice coil actuators. With the equations (3.35) and (3.36), the expression for \mathbf{u}_c in (3.20) can be evaluated. The relative position and angle of the coils to the frame B , which is fixed to the center of mass of the sensing element, is given in table 3.1. This information is necessary for the evaluation of equations (3.31) and (3.32). In this table, the quantities x_G , y_G and z_G indicate the position of the geometric center of the sensing element also expressed in the reference frame B . The following additional quantities are present in this table:

$$\begin{aligned} l_1 &= l + y_G; & l_2 &= l - y_G; & l_3 &= l - z_G \\ l_4 &= l + z_G; & l_5 &= l - x_G; & l_6 &= l + x_G \\ d_1 &= d + x_G; & d_2 &= d + y_G; & d_3 &= d + z_G \\ d_4 &= d - x_G; & d_5 &= d - y_G; & d_6 &= d - z_G \end{aligned}$$

The dimensions l and d are defined as shown in figure 3.10. The forces and torques generated by the twelve voice coil actuators are related to the currents by the following expression:

$$\mathbf{u}_c = \mathbf{T}_c \mathbf{K}_i \mathbf{i}_c, \quad (3.37)$$

where the vector

$$\mathbf{i}_c = [i_{I1} \ i_{I2} \ \dots \ i_{I6} \ i_{II1} \ i_{II2} \ \dots \ i_{II6}]^T \quad (3.38)$$

TABLE 3.1: Position and angle of the voice coil actuators relative to the sensing element.

Actuator	Position			Angle		
	${}^B x_C$	${}^B y_C$	${}^B z_C$	${}^B \phi_C$	${}^B \theta_C$	${}^B \psi_C$
I-1	$-d_1$	$-l_1$	$-z_G$	0	0	-90°
I-2	$-d_1$	l_2	$-z_G$	0	0	-90°
I-3	$-x_G$	$-d_2$	l_3	0	0	0
I-4	$-x_G$	$-d_2$	$-l_4$	0	0	0
I-5	l_5	$-y_G$	$-d_3$	90°	0	0
I-6	$-l_6$	$-y_G$	$-d_3$	90°	0	0
II-1	d_4	$-l_1$	$-z_G$	0	0	90°
II-2	d_4	l_2	$-z_G$	0	0	90°
II-3	$-x_G$	d_5	l_3	180°	0	0
II-4	$-x_G$	d_5	$-l_4$	180°	0	0
II-5	l_5	$-y_G$	d_6	-90°	0	0
II-6	$-l_6$	$-y_G$	d_6	-90°	0	0

comprises the currents in each voice coil actuator. The subscripts of the vector components associate the current values to the voice coil actuators as shown in figure 3.1. The matrix \mathbf{K}_i is diagonal and contains the twelve values for the actuator constant:

$$\mathbf{K}_i = \text{diag} (k_{Bl-I1}, \dots, k_{Bl-I6}, k_{Bl-II1}, \dots, k_{Bl-II6}) . \quad (3.39)$$

The transformation matrix

$$\mathbf{T}_c = [\mathbf{T}_{c-I} \quad \mathbf{T}_{c-II}] \quad (3.40)$$

is composed by the following matrices:

$$\mathbf{T}_{c-I} = \begin{bmatrix} 1 & 1 & 0 & 0 & 0 & 0 \\ 0 & 0 & 1 & 1 & 0 & 0 \\ 0 & 0 & 0 & 0 & 1 & 1 \\ 0 & 0 & -l_3 & l_4 & -y_G & -y_G \\ -z_G & -z_G & 0 & 0 & -l_5 & l_6 \\ l_1 & -l_2 & -x_G & -x_G & 0 & 0 \end{bmatrix} \quad (3.41)$$

$$\mathbf{T}_{c-II} = \begin{bmatrix} -1 & -1 & 0 & 0 & 0 & 0 \\ 0 & 0 & -1 & -1 & 0 & 0 \\ 0 & 0 & 0 & 0 & -1 & -1 \\ 0 & 0 & l_3 & -l_4 & y_G & y_G \\ z_G & z_G & 0 & 0 & l_5 & -l_6 \\ -l_1 & l_2 & x_G & x_G & 0 & 0 \end{bmatrix} \quad (3.42)$$

The matrix \mathbf{T}_c is used to describe the directions of the generated forces/torques in the reference frame B of the sensing element fixed to the center of mass.

Since the dynamic equations of the system are derived for the center of mass, it is necessary to express the matrix \mathbf{T}_c in this way. However, for most of the applications of the multicomponent transducer, it is desired to measure the forces and torques relative to some geometric reference. The expression of the forces and torques for the geometric center of the sensing element is possible by using the following transformation matrix:

$$\mathbf{T}_{co} = [\mathbf{T}_{co-I} \quad \mathbf{T}_{co-II}] \quad (3.43)$$

By evaluating the following expression the forces and torques generated by the voice coil actuators can be determined for the geometric center of the sensing element:

$$\mathbf{u}_{co} = \mathbf{T}_{co} \mathbf{K}_i \mathbf{i}_c \quad (3.44)$$

The matrix \mathbf{T}_{co} is composed by the following matrices:

$$\mathbf{T}_{co-I} = \begin{bmatrix} 1 & 1 & 0 & 0 & 0 & 0 \\ 0 & 0 & 1 & 1 & 0 & 0 \\ 0 & 0 & 0 & 0 & 1 & 1 \\ 0 & 0 & -l_{I3} & l_{I4} & 0 & 0 \\ 0 & 0 & 0 & 0 & -l_{I5} & l_{I6} \\ l_{I1} & -l_{I2} & 0 & 0 & 0 & 0 \end{bmatrix} \quad (3.45)$$

$$\mathbf{T}_{co-II} = \begin{bmatrix} -1 & -1 & 0 & 0 & 0 & 0 \\ 0 & 0 & -1 & -1 & 0 & 0 \\ 0 & 0 & 0 & 0 & -1 & -1 \\ 0 & 0 & l_{II3} & -l_{II4} & 0 & 0 \\ 0 & 0 & 0 & 0 & l_{II5} & -l_{II6} \\ -l_{II1} & l_{II2} & 0 & 0 & 0 & 0 \end{bmatrix} \quad (3.46)$$

The parameters l_{I1}, \dots, l_{I6} and l_{II1}, \dots, l_{II6} have approximately the same value as l . However, they represent the real values of this quantities for the different coils. This distinction was performed in the matrix \mathbf{u}_{co} only, and not for the matrix \mathbf{u}_c , because these matrices are used for different objectives. The matrix \mathbf{u}_c is used for the design and implementation of the control system and the precise determination of the parameter l for the coils is not necessary. The matrix \mathbf{u}_{co} is used for the determination of the forces and torques measured and the parameter l has be known with the uncertainty required.

As explained in section 3.1, the measurement of the induced voltages in coils I during the calibration mode is necessary. In the next subsection, a model for the determination of the voltages induced in the voice coil actuators based on the relative movement of coil and permanent magnets is provided.

3.2.3 INDUCED VOLTAGES IN THE ACTUATORS

Due to the Faraday's law of induction, a movement of the coil of the actuators causes an induced voltage in the coil. If we assume that the coil moves ideally along its geometric axis, the induced voltage depends only on the velocity in this

direction. However, as described in [54], in a real case there is a velocity component in all directions which affect the induced voltage. Additionally, temperature changes affect the magnetic field generated by the permanent magnet and also the induced voltage.

The induced voltage is described here as a function of the velocity of the movement, the relative position and angle of the coil to the magnet system and the temperature of the magnet system:

$$u_u({}^D\dot{\mathbf{x}}_C, {}^D\boldsymbol{\omega}_C, {}^D\mathbf{x}_C, {}^D\boldsymbol{\phi}_C, T_{ms}) \quad (3.47)$$

where ${}^D\dot{\mathbf{x}}_C$ contains the velocity of the point C of the coil relative to the reference frame fixed to D and ${}^D\boldsymbol{\omega}_C$ contains the angular velocity of the coil with respect to the frame D and expressed in this same frame. The determination of the quantities ${}^D\mathbf{x}_C$ and ${}^D\boldsymbol{\phi}_C$ was explained in the previous section.

The velocity of the point C relative to the point D is given by

$${}^D\dot{\mathbf{x}}_C = {}^D\dot{\mathbf{R}}_I ({}^I\mathbf{x}_C - {}^I\mathbf{x}_D) + {}^D\mathbf{R}_I ({}^I\dot{\mathbf{x}}_C - {}^I\dot{\mathbf{x}}_D) \quad (3.48)$$

The time derivative of the rotation matrix ${}^D\mathbf{R}_I$ is given by

$${}^D\dot{\mathbf{R}}_I = {}^D\tilde{\boldsymbol{\omega}}_I {}^D\mathbf{R}_I \quad (3.49)$$

where ${}^D\tilde{\boldsymbol{\omega}}_I$ is the angular velocity matrix. As described in [71, p. 695], for an angular velocity vector

$$\boldsymbol{\omega} = \begin{bmatrix} \omega_1 \\ \omega_2 \\ \omega_3 \end{bmatrix} \quad (3.50)$$

the angular velocity matrix is given by:

$$\tilde{\boldsymbol{\omega}} = \begin{bmatrix} 0 & -\omega_3 & \omega_2 \\ \omega_3 & 0 & -\omega_1 \\ -\omega_2 & \omega_1 & 0 \end{bmatrix} \quad (3.51)$$

The angular velocity of the inertial frame relative to the reference frame fixed to the magnet system at D , whose determination is necessary in order to evaluate the equation (3.49), is given by

$${}^D\boldsymbol{\omega}_I = -{}^D_I\boldsymbol{\omega}_D = -{}^D\mathbf{R}_A {}^A_I\boldsymbol{\omega}_A \quad (3.52)$$

For the evaluation of the equation (3.47) it is also necessary to determine the angular velocity of the coil relative to the magnet system:

$${}^D\boldsymbol{\omega}_C = {}^D_I\boldsymbol{\omega}_C - {}^D_I\boldsymbol{\omega}_D = {}^D_I\boldsymbol{\omega}_B - {}^D_I\boldsymbol{\omega}_A = {}^D\mathbf{R}_B {}^B_I\boldsymbol{\omega}_B - {}^D\mathbf{R}_A {}^A_I\boldsymbol{\omega}_A \quad (3.53)$$

The model shown here for the induced voltages in the actuators considers the movement of the coil relative to the magnet system in the six degrees of freedom simultaneously. However, during the calibration mode, the sensing element is moved in the six degrees of freedom separately. By considering this aspect it is possible to obtain a simplified version of the model for the induced voltages.

Model simplification for the induced voltages

During the calibration mode, in order to determine the calibration factors for the multicomponent transducer, the sensing element is moved with a sine wave reference trajectory in the six degrees of freedom. For the movement in x direction, the following voltages are obtained for the actuators 1 and 2 of the coil group I:

$$u_{I1} = u_{I10} \sin(\omega_0 t) = k_{Bl-I1} x_0 \omega_0 \sin(\omega_0 t) \quad (3.54)$$

$$u_{I2} = u_{I20} \sin(\omega_0 t) = k_{Bl-I2} x_0 \omega_0 \sin(\omega_0 t) \quad (3.55)$$

where x_0 represents the amplitude of motion, ω_0 represents the frequency of motion and t represents the time. For the movement in y direction, the following voltages are obtained for the actuators 3 and 4 of the coil group I:

$$u_{I3} = u_{I30} \sin(\omega_0 t) = k_{Bl-I3} y_0 \omega_0 \sin(\omega_0 t) \quad (3.56)$$

$$u_{I4} = u_{I40} \sin(\omega_0 t) = k_{Bl-I4} y_0 \omega_0 \sin(\omega_0 t) \quad (3.57)$$

where y_0 represents the amplitude of motion. For the movement in z direction, the following voltages are obtained for the actuators 5 and 6 of the coil group I:

$$u_{I5} = u_{I50} \sin(\omega_0 t) = k_{Bl-I5} z_0 \omega_0 \sin(\omega_0 t) \quad (3.58)$$

$$u_{I6} = u_{I60} \sin(\omega_0 t) = k_{Bl-I6} z_0 \omega_0 \sin(\omega_0 t) \quad (3.59)$$

where z_0 is the amplitude of motion. For the successive angular motion of the levitating element in the directions ϕ , θ and ψ , the following expressions for the induced voltages can be obtained:

$$u_{I1l} = u_{I1l0} \sin(\omega_0 t) = k_{Bl-I1} l_{I1} \psi_0 \omega_0 \sin(\omega_0 t) \quad (3.60)$$

$$u_{I2l} = -u_{I2l0} \sin(\omega_0 t) = -k_{Bl-I2} l_{I2} \psi_0 \omega_0 \sin(\omega_0 t) \quad (3.61)$$

$$u_{I3l} = -u_{I3l0} \sin(\omega_0 t) = -k_{Bl-I3} l_{I3} \phi_0 \omega_0 \sin(\omega_0 t) \quad (3.62)$$

$$u_{I4l} = u_{I4l0} \sin(\omega_0 t) = k_{Bl-I4} l_{I4} \phi_0 \omega_0 \sin(\omega_0 t) \quad (3.63)$$

$$u_{I5l} = -u_{I5l0} \sin(\omega_0 t) = -k_{Bl-I5} l_{I5} \theta_0 \omega_0 \sin(\omega_0 t) \quad (3.64)$$

$$u_{I6l} = u_{I6l0} \sin(\omega_0 t) = k_{Bl-I6} l_{I6} \theta_0 \omega_0 \sin(\omega_0 t) \quad (3.65)$$

for the amplitudes of motion ϕ_0 , θ_0 and ψ_0 .

The following expressions for the determination of the actuator constant for the six voice coil actuators of the group I can be obtained by using the equations (3.54)-(3.59):

$$k_{Bl-I1} = \frac{u_{I10}}{x_0 \omega_0}, \quad k_{Bl-I2} = \frac{u_{I20}}{x_0 \omega_0} \quad (3.66)$$

$$k_{Bl-I3} = \frac{u_{I30}}{y_0 \omega_0}, \quad k_{Bl-I4} = \frac{u_{I40}}{y_0 \omega_0} \quad (3.67)$$

$$k_{Bl-I5} = \frac{u_{I50}}{z_0 \omega_0}, \quad k_{Bl-I6} = \frac{u_{I60}}{z_0 \omega_0} \quad (3.68)$$

The following equations can be obtained for determining the parameters l_{11}, \dots, l_{16} , which are necessary for the traceable torque measurement:

$$l_{11} = \frac{u_{11l0}}{k_{Bl-11}\psi_0\omega_0}, \quad l_{12} = \frac{u_{12l0}}{k_{Bl-12}\psi_0\omega_0} \quad (3.69)$$

$$l_{13} = \frac{u_{13l0}}{k_{Bl-13}\phi_0\omega_0}, \quad l_{14} = \frac{u_{14l0}}{k_{Bl-14}\phi_0\omega_0} \quad (3.70)$$

$$l_{15} = \frac{u_{15l0}}{k_{Bl-15}\theta_0\omega_0}, \quad l_{16} = \frac{u_{16l0}}{k_{Bl-16}\theta_0\omega_0} \quad (3.71)$$

For the implementation of the control system and the integrated calibration, it is necessary to measure the position and angle of the sensing element. In the next section a mathematical model for the position measurement with the aperture slit sensors is provided.

3.2.4 POSITION MEASUREMENT

As explained in the section 3.1.2, the position and angle measuring system is composed by six aperture slit position sensors. Figure 3.11 shows this system. Each aperture slit sensor is composed by a LED, a dual photodiode and the aperture slit itself. The LED and the dual photodiode are fixed to the frame of the transducer and the aperture slit is fixed to the sensing element. The aperture slit is located between the LED and the dual photodiode. The movement of the aperture slit in the measurement direction causes a change in the light intensity received by each photodiode. This light intensity is given by the intersection between the radiant sensitive areas and the LED light shown in figure 3.11. By measuring the current in each photodiode, which is proportional to the light intensity, and calculating the difference between these currents, it is possible to determine the displacement of the aperture slit in the measurement direction. The current in each photodiode is amplified by using a transimpedance electronics and measured with a digital voltmeter. The output voltages for the upper and bottom photodiodes are given by u_{up} and u_{bot} respectively. The position signal is given by the voltage difference $u_{ps} = u_{up} - u_{bot}$, which is proportional to the current difference. Since the sensitivity of the photodiodes and the luminous efficacy of the LED depends on the temperature, there is a temperature dependency of the voltage difference. The effects of the temperature dependency in the position measurement can be reduced by compensating the changes in the voltage difference by using the sum of the voltages, or the total light intensity received by the photodiodes. The displacement information provided by the six aperture slits is used to determine the position and angle of the sensing element relative to the reference frame A . For modeling the aperture slit position sensor, two additional reference frames are defined. The reference frame E , is fixed to the center of the aperture slit, and the reference frame F , which is fixed to the dual photodiode. The position of both frames is shown in figure 3.11. The output of the sensors depend on the position ${}^F\mathbf{x}_E$ and angle ${}^F\phi_E$ of the aperture slit relative to F and the temperature T_{ps} . This output is given as:

$$u_{ps} = k_{ps}({}^F\mathbf{x}_E, {}^F\phi_E, T_{ps}) {}^Fy_E, \quad (3.72)$$

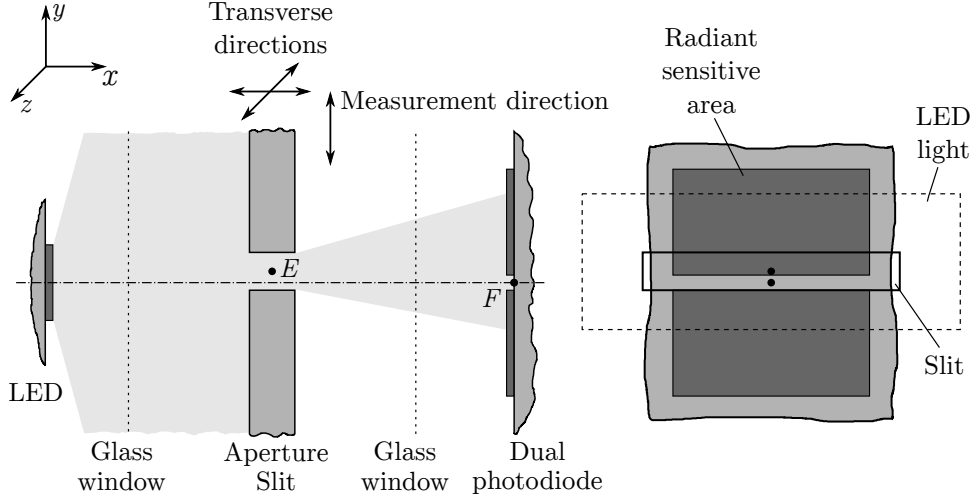


FIGURE 3.11: Position sensor with LED, aperture slit and dual photodiode [70]. On the right hand side the dual photodiode with the projection of the slit and the light from the LED is shown.

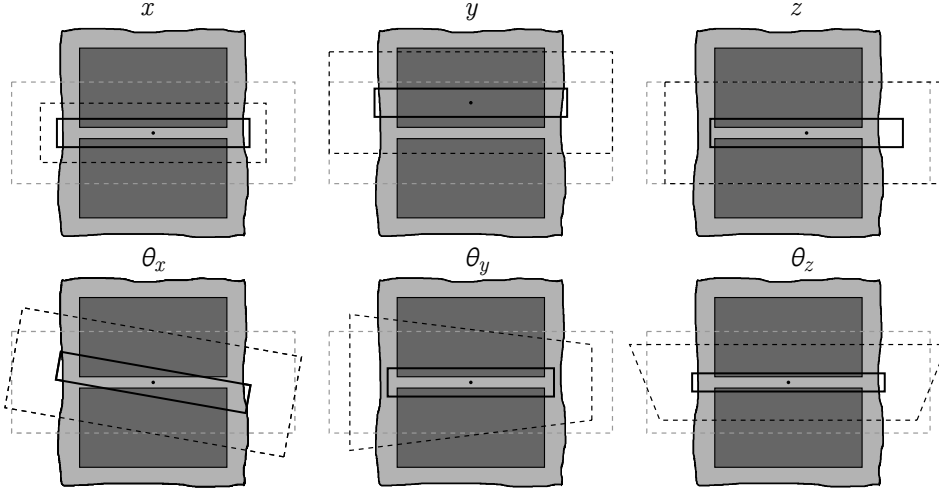


FIGURE 3.12: Light received by the dual photodiode after a linear or angular displacement of the aperture slit in different directions.

where k_{ps} represents the sensitivity of the aperture slit position sensor and $^F y_E$ is the displacement in the measurement direction.

A precise and simple mathematical description for the position measuring system is desired. However, several aspects of the LEDs, the dual-photodiodes and the geometry of the problem complicate the modeling procedure. The LEDs emit light in a range between -120° to 120° , and the intensity of the light emitted depends on the direction. The sensitivity of the dual photodiodes also depends on the direction of the light received. As shown in figure 3.12, the aperture slit can move in all six degrees of freedom. In this figure, gray and black colors represent the LED light before and after the movement respectively. Depending on the direction, this movement can affect the light intensity received by the photodiodes and the position measurement. For the movement in $+x$ direction there is a reduction in the light intensity received by the photodiodes. Since this

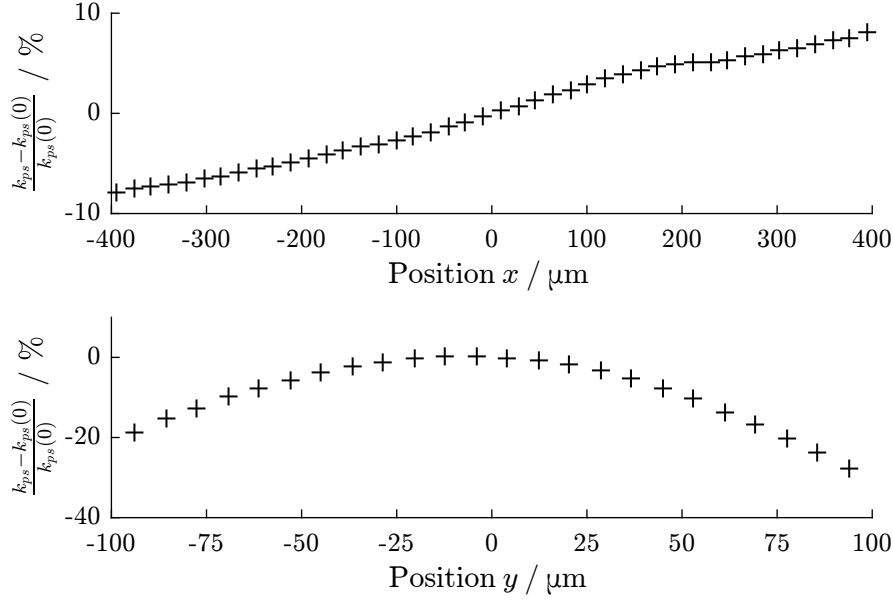


FIGURE 3.13: Sensitivity of the position sensor as a function of the displacement in transverse and measurement directions.

reduction is theoretically equal for both diodes, there is no change in the zero-position indication. However, this change in the light intensity causes a variation in the sensitivity of the position measurement system. For a movement in $+y$ direction the upper photodiode receives clearly more light than the photodiode on bottom. Since this is the measurement direction, this change is desired. There is also a change in the overall light intensity/direction, which causes a variation in the sensitivity of the position sensor. A variation in z direction of the slit causes in theory no change in the light intensity received by the photodiodes. This is valid for small changes in position, when the slit width is larger than the width of the photodiode sensitive area. A rotation θ_x in x direction or θ_y in y direction causes in theory no change in the light intensity difference received by the diodes. However, changes in the sensitivity of the position sensor are possible. A rotation θ_z in z direction can cause changes in both light intensity difference and overall light intensity in the dual photodiode. A measurement result with k_{ps} as a function of the displacement in x and y directions is shown in figure 3.13. This result was obtained by positioning the aperture slit with a high-precision two axis linear stage (appendix A, LS2A) and measuring the currents flowing in the photodiodes. In this figure, it is possible to observe the change in the sensitivity of the position sensors predicted during the analysis with figure 3.12. In figure 3.11 the LED and the dual photodiode are assumed to be in perfect position and alignment. In reality, the relative position and angle between these components are determined by manufacturing and assembling tolerances. These aspects of the position sensors increase the complexity of the model.

With the objective to identify the effects of the nonlinearities of the aperture slit sensors in the position and angle measurements, preliminary experiments were performed with a laser interferometer by using same measuring setup described in section 4.1. These experiments showed that the nonlinearities in both position and angle measurement can be approximated with a third order polynomial. This

information can be used to obtain a simplified model for the aperture slit sensors, which is described in the next section.

Simplified model for position and angle measurement

A simple mathematical representation for the position sensors is desired for the design and implementation of the control system. Results of preliminary experiments performed with the multicomponent transducer showed that the following mathematical description for the sensor has the necessary precision and is compatible with some practical requirements. Each aperture slit position sensor provides the position in one coordinate. The position and angle of the geometric center O of the sensing element, without considering the nonlinearities and temperature dependency of the position sensor, can be determined with the following expression:

$$\mathbf{y}_p = \mathbf{T}_{po} \mathbf{K}_p \mathbf{u}_{ps} \quad (3.73)$$

where the vector

$$\mathbf{u}_{ps} = [u_{ps1} \ u_{ps2} \ u_{ps3} \ u_{ps4} \ u_{ps5} \ u_{ps6}] \quad (3.74)$$

contains the output voltages of each position sensor. The matrix with the gains of the position sensors, which relates the voltage measurements to the position measurements, is given by:

$$\mathbf{K}_p = \text{diag}(K_{p1}, \dots, K_{p6}) \quad (3.75)$$

The components of this matrix are defined as:

$$\begin{aligned} K_{p1} &= \frac{1}{k_{ps1}({}^F\mathbf{x}_E = {}^F\mathbf{x}_{E0}, {}^F\phi_E = {}^F\phi_{E0}, T_{ps} = T_{cal})} \\ &\vdots \\ K_{p6} &= \frac{1}{k_{ps6}({}^F\mathbf{x}_E = {}^F\mathbf{x}_{E0}, {}^F\phi_E = {}^F\phi_{E0}, T_{ps} = T_{cal})} \end{aligned} \quad (3.76)$$

where ${}^F\mathbf{x}_{E0}$ and ${}^F\phi_{E0}$ represent the position and angle of the aperture slits when all six position sensors have an output voltage equal to zero and T_{cal} is the temperature of these sensors during the determination of the parameters K_{p1}, \dots, K_{p6} .

The matrix \mathbf{T}_{po} relates the six output positions of the aperture slit sensors to the position and angle of the sensing element. The position is measured relative to the geometric center of the sensing element. This center is defined by the point where the three axes of the sensing element intersect. By assuming small angular movements and doing a linear approximation, this matrix is given as:

$$\mathbf{T}_{po} = \begin{bmatrix} 1 & 0 & 0 & 0 & h & -l \\ 1 & 0 & 0 & 0 & h & l \\ 0 & 1 & 0 & -l & 0 & h \\ 0 & 1 & 0 & l & 0 & h \\ 0 & 0 & 1 & h & 0 & -l \\ 0 & 0 & 1 & h & 0 & l \end{bmatrix}^{-1} \quad (3.77)$$

where the parameters h and l are shown in figure 3.10. The vector \mathbf{y}_p contains the three position coordinates and angles of the sensing element relative to the rack of the transducer:

$$\mathbf{y}_p = \begin{bmatrix} {}^A\hat{\mathbf{x}}_O \\ {}^A\hat{\boldsymbol{\phi}}_O \end{bmatrix} = [\hat{x} \quad \hat{y} \quad \hat{z} \quad \hat{\theta}_x \quad \hat{\theta}_y \quad \hat{\theta}_z]^T \quad (3.78)$$

As described previously, the position sensors have a nonlinear behavior. These nonlinearities cause cross-talk and deviations in the position coordinates and angles of \mathbf{y}_p . For this reason, the components of this vector are indicated with carets. This behavior can be described by using the following equation with a third-order approximation:

$${}^A\mathbf{y}_O = \begin{bmatrix} {}^A\mathbf{x}_O \\ {}^A\boldsymbol{\phi}_O \end{bmatrix} = \mathbf{K}_{p1}\mathbf{y}_{p1} + \mathbf{K}_{p2}\mathbf{y}_{p2} + \mathbf{K}_{p3}\mathbf{y}_{p3} \quad (3.79)$$

where the vectors \mathbf{y}_{p1} , \mathbf{y}_{p2} and \mathbf{y}_{p3} are given as:

$$\mathbf{y}_{p1} = [\hat{x} \quad \hat{y} \quad \hat{z} \quad \hat{\theta}_x \quad \hat{\theta}_y \quad \hat{\theta}_z]^T \quad (3.80)$$

$$\mathbf{y}_{p2} = [\hat{x}^2 \quad \hat{y}^2 \quad \hat{z}^2 \quad \hat{\theta}_x^2 \quad \hat{\theta}_y^2 \quad \hat{\theta}_z^2]^T \quad (3.81)$$

$$\mathbf{y}_{p3} = [\hat{x}^3 \quad \hat{y}^3 \quad \hat{z}^3 \quad \hat{\theta}_x^3 \quad \hat{\theta}_y^3 \quad \hat{\theta}_z^3]^T \quad (3.82)$$

The vector ${}^A\mathbf{y}_O$ contains the corrected position and angle coordinates. A practical problem is found when trying to determine the matrices \mathbf{K}_p , \mathbf{T}_{po} , \mathbf{K}_{p1} , \mathbf{K}_{p2} and \mathbf{K}_{p3} precisely. In order to determine the parameters of these matrices the system has to be in operation and the parameters can be measured, for instance, by using a laser interferometer. However, these matrices are necessary in order to properly start the operation of the transducer. The following strategy is used in this case: the matrices \mathbf{K}_p and \mathbf{T}_{po} are estimated by using the geometric properties of the transducer and the properties of the LEDs and photodiodes of the position sensors. With both matrices it is possible to start the operation of the transducer without knowing the parameters of matrices \mathbf{K}_{p1} , \mathbf{K}_{p2} and \mathbf{K}_{p3} . Although the system is in operation and the sensing element is levitating, the position and angle coordinates are not defined accurately. After that, a calibration of the position and angle measuring system is performed and these matrices are determined. This calibration procedure is described with details in section 4.1.

The position and angle given by the vector ${}^A\mathbf{y}_O$ are determined for the geometric center of the sensing element. However, the position and angle in the dynamic equations of the system (3.17) and (3.18) are given for the center of mass of the sensing element. For this reason it is necessary to determine the position and angle of the sensing element for the center of mass as well. This is possible by using the following transformation:

$${}^A\mathbf{x}_B = {}^A\mathbf{x}_O - {}^A\mathbf{R}_B {}^B\mathbf{x}_O \quad (3.83)$$

$${}^A\boldsymbol{\phi}_B = {}^A\boldsymbol{\phi}_O \quad (3.84)$$

where the vector with the coordinates of the geometric center expressed in the reference frame B is given as:

$${}^B\mathbf{x}_O = [x_G \ y_G \ z_G]^T \quad (3.85)$$

By defining

$${}^A\mathbf{y}_B = \begin{bmatrix} {}^A\mathbf{x}_B \\ {}^A\phi_B \end{bmatrix} \quad (3.86)$$

and assuming that the angles of the sensing element relative to the transducer rack are very small, so that

$${}^A\mathbf{R}_B = \begin{bmatrix} 1 & -{}^A\psi_B & {}^A\theta_B \\ {}^A\psi_B & 1 & -{}^A\phi_B \\ -{}^A\theta_B & {}^A\phi_B & 1 \end{bmatrix}, \quad (3.87)$$

the following expression can be obtained for determining the angle and center of mass position of the sensing element relative to the reference frame fixed to the rack of the transducer:

$${}^A\mathbf{y}_B = \mathbf{T}_{bo}^{-1}({}^A\mathbf{y}_O - \mathbf{y}_G), \quad (3.88)$$

where the matrix \mathbf{T}_{bo} is given by:

$$\mathbf{T}_{bo} = \begin{bmatrix} 1 & 0 & 0 & 0 & z_G & -y_G \\ 0 & 1 & 0 & -z_G & 0 & x_G \\ 0 & 0 & 1 & y_G & -x_G & 0 \\ 0 & 0 & 0 & 1 & 0 & 0 \\ 0 & 0 & 0 & 0 & 1 & 0 \\ 0 & 0 & 0 & 0 & 0 & 1 \end{bmatrix} \quad (3.89)$$

and the vector \mathbf{y}_G is given as:

$$\mathbf{y}_G = [x_G \ y_G \ z_G \ 0 \ 0 \ 0]^T \quad (3.90)$$

Since the equations (3.17) and (3.18) contain the position and angle of the sensing element for the inertial frame of reference, the following transformations are necessary:

$${}^I\mathbf{x}_B = {}^I\mathbf{x}_A + {}^I\mathbf{R}_A {}^A\mathbf{x}_B \quad (3.91)$$

$${}^I\phi_B = {}^I\phi_A + {}^A\phi_B \quad (3.92)$$

The angle of the transducer rack relative to the inertial frame is also assumed to be very small, so that:

$${}^I\mathbf{R}_A = \begin{bmatrix} 1 & -{}^I\psi_A & {}^I\theta_A \\ {}^I\psi_A & 1 & -{}^I\phi_A \\ -{}^I\theta_A & {}^I\phi_A & 1 \end{bmatrix} \quad (3.93)$$

With the results from equations (3.91) and (3.92) it is possible to determine the vector \mathbf{y} as defined in (3.23). The vectors ${}^I\mathbf{x}_A$ and ${}^I\phi_A$ represent the position

and angle of the transducer rack relative to the inertial frame. These quantities are very often unknown and assumed to be constant. This assumption is reasonable for most of the applications, when the transducer is fixed to some stationary reference. However, for some applications this is not the case and the accelerations of the transducer rack have to be regarded. A further simplification is possible, which can be used to make the control system design procedure even simpler. The position of the sensing element relative to the transducer rack is limited to $\pm 90 \mu\text{m}$ in all direction. For this small range of motion, the product of the angles ${}^I\phi_A$, ${}^I\theta_A$ and ${}^I\psi_A$ with the position coordinates can be neglected and the equation (3.91) is equal to:

$${}^I\mathbf{x}_B = {}^I\mathbf{x}_A + {}^A\mathbf{x}_B \quad (3.94)$$

With this approximation and the equation (3.92) the following expression can be obtained:

$$\mathbf{y} = \mathbf{y}_s + {}^A\mathbf{y}_B \quad (3.95)$$

where, as described previously, \mathbf{y} is the position and angle of the sensing element relative to the inertial reference frame, \mathbf{y}_s is the position and angle of the transducer rack relative to the inertial reference frame and ${}^A\mathbf{y}_B$ is the position and angle of the sensing element relative to the transducer rack, which represents the position and angle measured with the aperture slit sensors.

In order to obtain a complete model for the multicomponent transducer it is still necessary to model the forces generated by the gravity acceleration and the forces and toques generated by the metallic wires. Additionally, some further considerations are necessary, such as the damping effects in the system. These aspects are described in the next subsections.

3.2.5 EFFECTS OF GRAVITY ACCELERATION

The local gravity acceleration acting in the system is responsible for generating a force in the center of mass of the sensing element. The magnitude of this force is given by the product of the mass of the sensing element with the magnitude of the local gravity acceleration. The force direction is parallel to the gravity acceleration. Since the state space model given by equations (3.17) and (3.18) is derived for the center of mass of the sensing element, there is no torque generated by the gravity force in the system.

The input vector \mathbf{u}_g of the system, which is responsible for the gravity force contribution, is given as:

$$\mathbf{u}_g = mg \begin{bmatrix} \gamma_x & \gamma_y & \gamma_z & 0 & 0 & 0 \end{bmatrix}^T \quad (3.96)$$

where the variables γ_x , γ_y and γ_z indicate the direction of the gravitational force expressed in the inertial reference frame I . This direction is given in a way that:

$$\sqrt{\gamma_x^2 + \gamma_y^2 + \gamma_z^2} = 1 \quad (3.97)$$

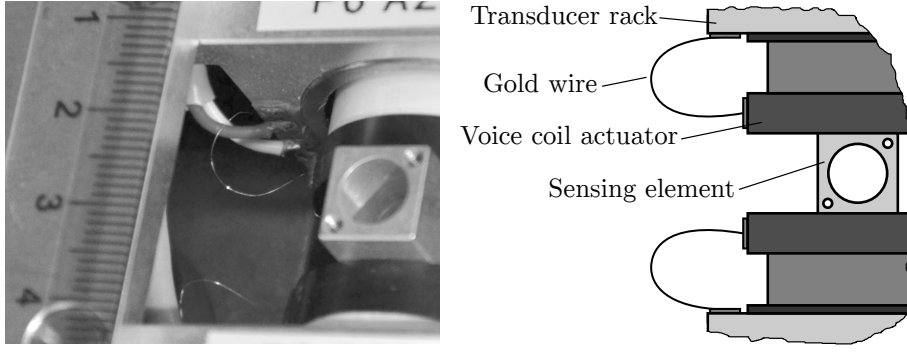


FIGURE 3.14: Picture and drawing showing the form of the gold wires used to transmit the electrical current to the electromagnetic actuators. The ruler in the left hand side shows the length in centimetres.

3.2.6 METALLIC WIRES

Thin wires are used to transmit the electric current from the frame of the transducer to the coils of the actuators. The stiffness of these wires is responsible for causing restoring forces and torques when the sensing element is moved. Offset forces and torques can also be generated by these wires, which are caused by a pretension. Assuming that, during a measurement task, the pretension in the wires is constant and the position and angle of the sensing element do not change, there is no deviation caused in both force and torque measurements by the stiffness of the wires. This is the case for several applications of the multicomponent transducer. However, for some specific applications, such as the micromachining, the sensing element has to be moved during the force measurement task. For this reason it is desired to minimize the stiffness caused by the wires. Since the stiffness is related to the sensitivity of the transducer [74], a low stiffness for the wires is also an advantage for the resolution of both force and torque measurement.

A mathematical model for the stiffness of the wires is derived with the objective to estimate the restoring forces generated. The wires are fixed to both transducer frame and sensing element. The tip fixed to the sensing element can move in all six degrees of freedom. In the real case the stiffness of the wires depends on several aspects, such as the geometry of the wires, the direction of movement, the exact material of the wire and the temperature. In the multicomponent transducer the wires are bent in the form shown in figure 3.14. A model based on the linear beam theory is proposed here to estimate the maximal stiffness for each wire. It uses the expression for the elastic deflection at the free end of a cantilever beam loaded with a force at the same end. The model proposed here is given by:

$$c_{\max} = \frac{3}{l_s^3} EI_a, \quad (3.98)$$

where E is the Young's modulus for the material, l_s is the effective length of the wire, which is defined here as the half of the wire length $l = 20$ mm

$$l_s = \frac{l}{2}, \quad (3.99)$$

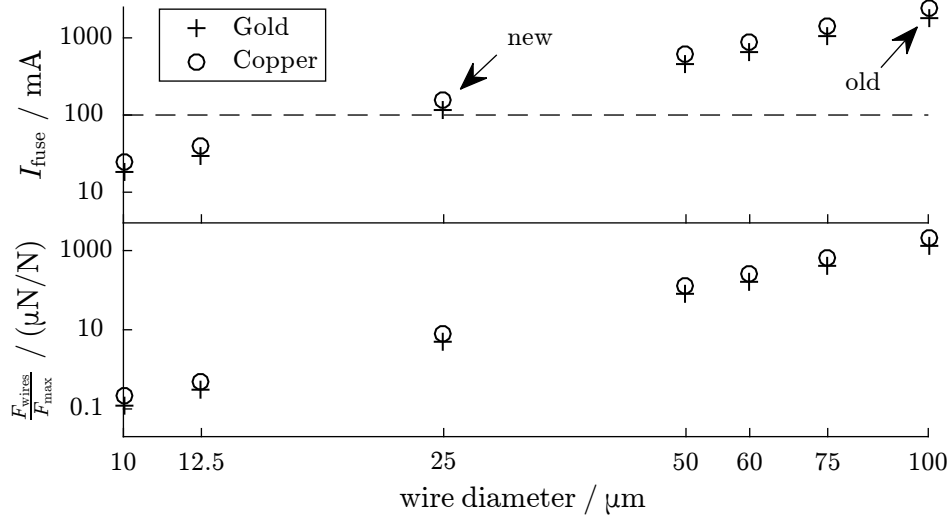


FIGURE 3.15: Fusing current and maximal relative force ($F_{\text{max}} = 2\text{ N}$) as a function of the wire diameter. The maximum operating current of 100 mA is indicated with a dashed line. Only diameters from commercially available wires are displayed.

and I_a is the second moment of area for the cross section of the wire, which is given as

$$I_a = \frac{\pi}{64} D_{\text{wire}}^4. \quad (3.100)$$

The quantity D_{wire} is the diameter of the wire. The maximal force generated by the wires, which is given by the maximal displacement for the sensing element of $\Delta x = 90\text{ }\mu\text{m}$, is estimated to be:

$$F_{\text{wires}} = n_{\text{wires}} c_{\text{max}} \Delta x \quad (3.101)$$

where $n_{\text{wires}} = 24$ is the number of wires used. Two materials are typically used as conductors in precision scales: gold and copper. The Young's modulus for these materials are given as 81 GPa and 117 GPa respectively. The length of the wires is predetermined in the initial design of the transducer and the diameter can be freely chosen. The stiffness of the wires can be minimized by reducing the diameter. However, by reducing the diameter, the electrical resistance of the wires increases and, for the maximal current of 100 mA, there is a bottom limit for the wire diameter where the wire fusing occurs. The fusing current, which was evaluated in [75], is related to the diameter by the following expression:

$$I_{\text{fuse}} = M \frac{A}{l} = \frac{\pi M}{4l} D_{\text{wire}}^2, \quad (3.102)$$

with the metal constant M equal to $4.685\text{ }\mu\text{A/m}$ for gold and $6.314\text{ }\mu\text{A/m}$ for copper. Figure 3.15 shows both fusing current for each wire and the maximal overall force generated by the wires as a function of the wire diameter. In this figure, only wire diameters for commercial products are shown (GCW, appendix A). It can be observed that, for a fusing current of 100 mA, the minimum possible diameter is 25 μm. For both gold and copper wires the maximum force caused

by the wires has a order of magnitude of $10 \mu\text{N/N}$. The previous version [12] of the EMFC multicomponent transducer was equipped with $100 \mu\text{m}$ wires and, by reducing this diameter, the stiffness was reduced by a factor of about 100. The change in the electrical resistance of the metallic wires was from 0.043Ω to about 1.0Ω . This change is very small relative to the coil resistance of about 200Ω .

For the mathematical model used in the design of the control system the forces and torques generated by the wires will be neglected. In this case, the input vector \mathbf{u}_c of the system, which represents the compliance term, is given as:

$$\mathbf{u}_c = \mathbf{0}_{6 \times 1} \quad (3.103)$$

3.2.7 FURTHER CONSIDERATIONS

There are further aspects of the multicomponent transducer which must be considered in the mathematical model, including the voltage-to-current converters, the damping caused by eddy currents induced in the sensing element and effects of ground vibrations.

The voltage-to-current (U/I) converters are the same as developed in [12] and the performance of these converters was extensively evaluated in that work. A diagram with the frequency response of the converters [12, p. 65] shows that, for frequencies below 1 kHz, the gain of the transfer function is constant. Since the operation range for both force and torque measurements is under 100 Hz, the U/I converters can be modeled as a constant gain.

The sensing element of the multicomponent transducer is made of aluminum. When this sensing element moves, interaction forces between the aluminum parts and the magnetic field from the permanent magnets arise. These forces are caused by the interaction between eddy currents flowing in the sensing element and the magnetic field of the permanent magnet. They depend on the velocity of the sensing element and have an opposite direction relative to the movement. The effects of these damping forces generate measurement deviations for measuring dynamic forces, when the sensing element is moving with relative high velocities. These damping forces are neglected in the mathematical model presented here. A further contribution to the damping of the system is the air friction with the sensing element of the transducer [76]. These effects of damping will also be neglected for the model used for the control system design. In this case, the input vector \mathbf{u}_d , which represents the damping term, is given as:

$$\mathbf{u}_d = \mathbf{0}_{6 \times 1} \quad (3.104)$$

Ground vibrations also affect the measurement of forces and torques and can be included in the model if desired by using the variable \mathbf{y}_s of equation (3.95). An extensive description of ground vibrations is given in [77], with typical frequency and amplitude ranges together with different causes for the vibrations.

3.2.8 THE PLANT

In the previous sections, mathematical models for the main components of the multicomponent transducer were described, including the mechanical hardware,

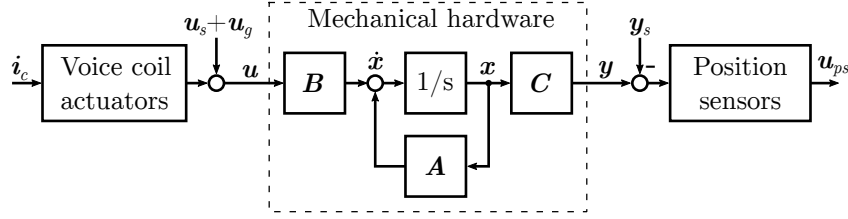


FIGURE 3.16: Block diagram for the multicomponent transducer in open loop.

the electromagnetic actuators and the optical position sensors. Figure 3.16 shows a block diagram with these components. The main equations for the mechanical hardware of the transducer are given by (3.17) and (3.18). The expression describing the forces and torques generated by the voice coil actuators is given by (3.37) and the model for the position and angle measurement with the aperture slit sensors is described by (3.95) together with (3.88), (3.79) and (3.73). The symbol s represents the complex variable used for the Laplace transform and $1/s$ represents an integrator in s -domain.

In order to derive this model, rigid body behavior was assumed for the sensing element and the angular motions were assumed to be smaller than 2 mrad. The inertia matrix of the sensing element was assumed to be diagonal and the linear movement of the sensing element relative to the transducer rack was assumed to be smaller than 90 μm . Several other assumptions were applied to the voice coil actuators and the position sensors, which are described in sections 3.2.2 and 3.2.4 respectively. The stiffness of the metallic wires used to transmit the electric current to the actuators and the damping effects in the system were neglected. This model is a basis for the control system design and system identification procedure described in the next section.

3.3 CONTROL SYSTEM

In this section a description of the control system design and the system identification routine is provided. Basically two controllers are used in the multicomponent transducer: a robust controller responsible for levitating the sensing element during the system activation routine and an optimized used for the precise force and torque measurement. The system identification routine is necessary for the determination of some parameters required for the optimized controller. Measurements results showing the achievable force and torque resolution with the control systems are shown. An overview on the implementation of hybrid control systems is also provided with an example of mixed position and force control, used for performing surface micromachining tasks.

3.3.1 DESIGN AND IMPLEMENTATION

The plant model for the multicomponent transducer described in the last section is used for the design of the control system. By applying a Laplace transform to the state-space equations of the mechanical hardware shown in (3.17) and (3.18),

the following equation can be obtained:

$$\mathbf{y}(s) = \mathbf{G}_g(s)\mathbf{u}(s), \quad (3.105)$$

where the matrix transfer function $\mathbf{G}_g(s)$ is given by:

$$\mathbf{G}_g(s) = \frac{1}{s^2} \begin{bmatrix} \frac{1}{m} & 0 & 0 & 0 & 0 & 0 \\ 0 & \frac{1}{m} & 0 & 0 & 0 & 0 \\ 0 & 0 & \frac{1}{m} & 0 & 0 & 0 \\ 0 & 0 & 0 & \frac{1}{I_{xx}} & 0 & 0 \\ 0 & 0 & 0 & 0 & \frac{1}{I_{yy}} & 0 \\ 0 & 0 & 0 & 0 & 0 & \frac{1}{I_{zz}} \end{bmatrix} \quad (3.106)$$

This matrix has six elements on its diagonal, which have the following format:

$$G_i(s) = \frac{1}{a_i s^2} \quad (3.107)$$

where $a_i \in \mathbb{R}$ represents the mass m of the sensing element for $i = 1, 2$ or 3 and the inertia moments I_{xx} , I_{yy} and I_{zz} for $i = 4, 5$ and 6 respectively.

By considering the matrix transfer function $\mathbf{G}_g(s)$, the control system can be designed for the six degrees of freedom separately. In this way there is no need to address the MIMO control system design directly. This problem is reduced to six SISO control design tasks, that can be accomplished by using classic methods of the linear control theory. This simplifies not only the design of the control system, but also its implementation and the system identification task. Furthermore, the outputs and inputs of the matrix transfer function $\mathbf{G}_g(s)$ are expressed in metre (or radian) and newton (or newton metre) respectively, being directly related to the position and angle of the sensing element and the applied forces and torques. That makes the implementation and analysis of the control system more intuitive.

In order to implement the control system designed with (3.106), it is necessary to use the results from (3.37) for the voice coil actuators and from (3.88), (3.79) and (3.73) for the position sensors. This is necessary for the determination of the forces and torques generated by the electromagnetic actuators and the position and angle of the sensing element. However, to obtain these equations the position of the center of mass of the sensing element relative to its geometric center was assumed to be known. This represents a practical difficulty because this position changes when some external component is attached to the sensing element. For this reason the coordinates of the center of mass of the sensing element have to be determined by means of an identification routine, which is described in subsection 3.3.4.

Figure 3.17 shows a block diagram with the structure of the control system for one degree of freedom. In order to control the system a PID control strategy is adopted:

$$H_i(s) = \hat{a}_i \left(K_P + K_I \frac{1}{s} + K_D \frac{N}{1 + N/s} \right), \quad (3.108)$$

where K_P , K_I and K_D correspond to the proportional, integral and derivative gains respectively and N is a filter constant. With this control system it is

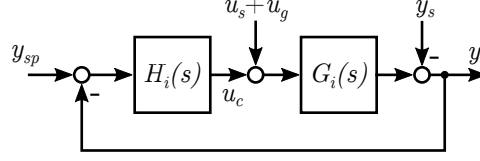


FIGURE 3.17: Structure of the control system for one degree of freedom.

possible to stabilize the transducer's dynamics, regulate its time performance and compensate the external forces and torques simultaneously. Furthermore, its straightforward structure simplifies the parallel implementation for the six degrees of freedom. The variables \hat{a}_i for $i = 1, 2, \dots, 6$ are an estimation for a_i and, for the next steps, they are assumed to be equal.

Two variables are treated as system outputs for the control design: the position or angle y and the controller output u_c . As inputs, the controller reference y_{sp} , the force or torque to be measured u_s , the gravitational force u_g (for an angular direction $u_g = 0$) and the position or angle disturbance y_s are considered. The following equations can be obtained for both system outputs:

$$(1 + G_i H_i) y = G_i H_i y_{sp} + G_i (u_g + u_s) - y_s \quad (3.109)$$

$$(1 + G_i H_i) u_c = H_i (y_{sp} + y_s) - G_i H_i (u_g + u_s) \quad (3.110)$$

By substituting (3.107) and (3.108) in (3.109) and (3.110), the following transfer functions can be obtained:

$$\frac{y(s)}{y_{sp}(s)} = \frac{(K_P + K_D N) s^2 + (K_P N + K_I) s + K_I N}{s^4 + N s^3 + (K_P + K_D N) s^2 + (K_P N + K_I) s + K_I N} \quad (3.111)$$

$$\frac{u_c(s)}{y_s(s)} = \frac{a_i s^2 ((K_P + K_D N) s^2 + (K_P N + K_I) s + K_I N)}{s^4 + N s^3 + (K_P + K_D N) s^2 + (K_P N + K_I) s + K_I N} \quad (3.112)$$

The transfer function (3.111) corresponds to the position or angle as a function of the controller reference. The frequency response of this transfer function contains several characteristics of the system's performance, such as the system's damping and natural frequency. These parameters are used in section 3.3.2 as constraints for the control optimization problem. The transfer function (3.112) describes the controller output as a function of the position or angle disturbance. This transfer function is a measure for the system's sensitivity against position or angle disturbances in the displacement sensor, such as ground vibrations and electromagnetic noises.

As described in subsection 3.1.3, there are two control strategies that must be implemented for the system: A robust controller for the control system activation routine and an optimized controller for normal system operation. Since the controller for normal system operation is executed after an identification task, it is reasonable to assume for the control system design that the position of the center of mass, the inertia torques and the mass of the sensing element are known. That means the assumptions used to obtain equations (3.111) and (3.112) hold

and these equations can be used to design the controller for normal system operation. Through these equations, the disturbance sensitivity of the system can be minimized as described in subsection 3.3.2. However, for the controller used during the system activation more care should be taken. In this case, the exact values for the position of the center of mass, the inertia torques and the mass of the sensing element are unknown and the assumptions used in order to obtain equations (3.111) and (3.112) do not hold anymore. More specifically, the center of mass of the sensing element relative to its geometric center and the variables a_i for $i = 1, \dots, 6$ are not exactly known, and the simple closed-loop control structure of figure 3.17 together with these transfer functions are not valid anymore. The design of the controller for system activation is addressed in section 3.3.3.

3.3.2 CONTROLLER FOR NORMAL SYSTEM OPERATION

The closed loop transfer function of the multicomponent transducer relating the inputs and outputs (3.111) is exclusively determined by the control system parameters. These parameters can be freely chosen during the control design task in order to adjust the system's performance. For that, performance indicators should be properly defined considering the operational requirements of the multicomponent transducer.

The signal to noise ratio of the measured force and torque signals is of major importance for the system. This is because the noise of the measured signal is a limitation to the transducer's resolution. The system has numerous noise sources that contribute to the resulting noise in the output signal, such as ground vibrations, electromagnetic fields and electric noise. The influences of the noise present in the position sensors are described by the transfer function (3.112), and can be reduced by minimizing the following position noise amplification factor:

$$f_G \triangleq \frac{1}{a_i} \lim_{s \rightarrow \infty} \frac{u_c(s)}{y_s(s)} = K_P + K_D N \quad (3.113)$$

This position noise amplification factor is defined in a way that it doesn't depend on the mass or inertia torques of the sensing element. This factor is an upper limit for the gain of the frequency response of (3.112). Figure 3.18 contains both this frequency response and the position noise amplification factor.

Further relevant performance characteristics of the multicomponent transducer are the system's eigenfrequency and damping. The eigenfrequency is related to the frequency bandwidth of the measurable forces and torques. If the frequency spectrum of the signal to be measured is in a frequency interval in the range of the transducer's eigenfrequency and above, the measured signal will be distorted. The frequency response of the multicomponent transducer with its eigenfrequency are shown in figure 3.19. The system's damping ratio is an additional factor that should be regarded. It is a measurement for the system's signal overshoot and is also determined by evaluating the frequency response of (3.111).

Since the measurement signal noise is a limiting factor for the transducer resolution, it is reasonable to design the control system in a way that the position noise amplification factor remains as low as possible. Therefore, the control system design is written as an optimization problem where the position noise

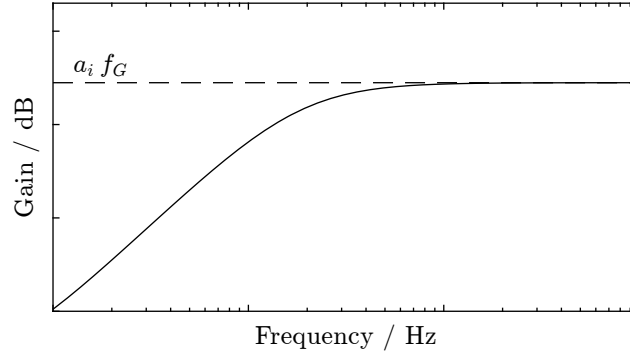


FIGURE 3.18: Frequency response of actuator force to position noise and position noise amplification factor f_G . Refer to equation (3.112).

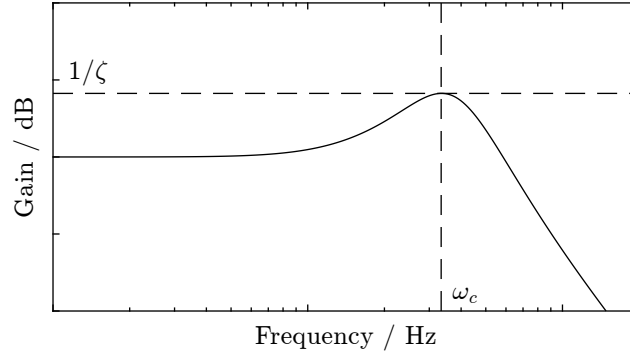


FIGURE 3.19: Frequency response of output position to position reference, eigenfrequency ω_c and damping factor ζ of the multi-component transducer. Refer to equation (3.111).

amplification factor is minimized:

$$\min \quad f_G(K_P, K_D, N) = K_P + K_D N \quad (3.114)$$

$$\text{for } \omega_c^{\min} \leq \omega_c(K_P, K_I, K_D, N) \leq \omega_c^{\max} \quad (3.115)$$

$$\zeta^{\min} \leq \zeta(K_P, K_I, K_D, N) \quad (3.116)$$

Values for the eigenfrequency ω_c and the damping ζ are defined as constraints for the problem, in a way that the transducer dynamics stay compatible with the frequency bandwidth of the forces to be measured. This optimization problem is solved by defining a finite discrete search domain for the control parameters K_P , K_I , K_D and N , and evaluating the system's position noise amplification factor, eigenfrequency and damping for every combination of control parameters in this search domain. This is a simple and feasible method, since the evaluation of the performance indicators can be executed relatively fast by means of efficient computer algorithms. Table 3.2 contains control gains which were determined by using this method for different nominal values of natural frequencies ω_c^N and $\zeta^{\min} = 0.7$. ω_c^{\min} and ω_c^{\max} were defined equal to $0.99\omega_c^N$ and $1.01\omega_c^N$ respectively, what corresponds to a variation of $\pm 1\%$ for ω_c .

TABLE 3.2: Control parameters for $\zeta^{min} = 0.7$.

ω_c^N [Hz]	K_P	K_I	K_D	N
5	872.241	521.383	42.0347	129.056
10	3852.11	384.322	89.0471	300.897
20	14757.4	1474.07	166.798	551.455
30	31357.7	19215.1	254.978	791.611
40	59876.8	5983.82	385.521	1230.35
50	93113.8	9306.87	450.628	1449.98
60	137366	13731.2	543.162	1852.55
70	188954	706829	684.829	2258.82
80	227361	255701	748.574	2256.16

3.3.3 CONTROLLER FOR THE SYSTEM ACTIVATION

For the system activation routine a robust controller should be designed that stays stable and exhibits a reasonable settling time for different transducer load states. Since this controller is not used for force and torque measurements itself, the output signal noise is not regarded during the control system design.

When some external device is attached to the sensing element, its mass, inertia torques and the position of the center of mass change. If these changes are not regarded in the control system design and the center of mass coordinates for the sensing element, as well as the control parameters a_i for $i = 1, 2, \dots, 6$, are not updated, a coupling between the dynamic equations of the system arises.

In order to design the control system, the following approach was used: a controller for one degree of freedom was designed in a process similar to the method explained in section 3.3.2, but without defining the control system design as an optimization problem. In this case, a robust controller was designed by using the root locus method. The stability and robustness of this controller for the system with the coupling can be analyzed by means of computer simulations and later verified by performing experiments with the transducer prototype. If the system with the implemented set of control gains doesn't exhibit the necessary robustness, a new set of parameters is determined in an iterative process.

Because of the problem's complexity, designing the robust controller by analytic approaches is not as simple as the design problem considered in section 3.3.2. The fact that methods based on inspection and trial and error may not lead to an optimal solution is not a problem in this case, because the robust controller is only employed during the system initialization process and the identification task.

3.3.4 PARAMETRIC SYSTEM IDENTIFICATION

The parametric system identification is a task performed during the system activation routine of the transducer and is responsible for identifying the mass, the position of the center of mass and the inertia torques of the sensing element. The system identification task is divided in three steps: in the first step, the mass of the sensing element is determined by means of a static measurement. In this

process, the direction of the gravity force can be obtained as well. In the second step, the position of the center of mass is determined, and in the third step, the inertia torques of the body are measured. For the steps two and three, dynamic identification methods are employed.

When the sensing element is levitating and only the gravity force and the forces/torques of the controller are actuating in the system, a static behavior can be assumed. The following equation can be obtained:

$$0 = \mathbf{u}_c + \mathbf{u}_g \quad (3.117)$$

This equation gives a relationship between the gravity force actuating in the sensing element and the currents in the actuators:

$$\mathbf{u}_g = -\mathbf{T}_c \mathbf{K}_i \mathbf{i}_c \quad (3.118)$$

The following expressions for determining the mass of the sensing element based on the measured currents can be obtained:

$$m = \frac{|\vec{F}|}{|\vec{g}|} = \frac{1}{g} \sqrt{(k_{Bl-I1}i_{I1} + k_{Bl-I2}i_{I2})^2 + \dots + (k_{Bl-I5}i_{I5} + k_{Bl-I6}i_{I6})^2} \quad (3.119)$$

where $|\vec{F}|$ and $|\vec{g}|$ represent the magnitude of the force measured and local gravity acceleration respectively. Since only the group I of voice coil actuators is activated for controlling the position and angle of the sensing element, there are only six currents in this expression. The direction of the gravity force can be determined as well:

$$\gamma_x = \frac{k_{Bl-I1}i_{I1} + k_{Bl-I2}i_{I2}}{mg} \quad (3.120)$$

$$\gamma_y = \frac{k_{Bl-I3}i_{I3} + k_{Bl-I4}i_{I4}}{mg} \quad (3.121)$$

$$\gamma_z = \frac{k_{Bl-I5}i_{I5} + k_{Bl-I6}i_{I6}}{mg} \quad (3.122)$$

For determining the position coordinates of the center of gravity of the sensing element, another identification method was used. This method is shown in figure 3.20, with an example for the y coordinate of the center of gravity. In this example, a value \hat{y}_G for the position coordinate of the center of mass is assumed and the body is oscillated in the x direction. During this oscillation the torque T_z is measured and this is done for different values of \hat{y}_G . When the assumed position for the center of mass \hat{y}_G is equal to the position of the center of mass y_G , the generated torque T_z is equal to zero. This could also be done by oscillating the levitating body in the z direction and measuring the torque T_x . This procedure is analogous for determining the coordinates x and z of the center of mass.

By determining the position of the center of mass of the sensing element, the parameters x_G , y_G and z_G are known and the equations of sections 3.2.2 and 3.2.4 can be used to determine the forces generated by the electromagnetic actuators and the position and angle of the sensing element. The matrix transfer

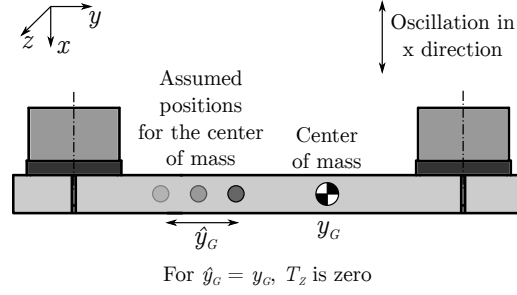


FIGURE 3.20: Principle of the identification procedure used to determine the position of the center of mass of the sensing element.

function (3.106) becomes valid and the six degrees of freedom of the system are decoupled. For the three angular directions, the system has the following closed loop transfer function:

$$G_{Ci} = \frac{y(s)}{y_{sp}(s)} = \frac{(K_P + K_D N)s^2 + (K_P N + K_I)s + K_I N}{\frac{a_i}{\hat{a}_i}(s^4 + Ns^3) + (K_P + K_D N)s^2 + (K_P N + K_I)s + K_I N} \quad (3.123)$$

with $i = 4, 5$ and 6 . In this case, $a_4 = I_{xx}$, $a_5 = I_{yy}$ and $a_6 = I_{zz}$, and the quantities \hat{a}_4 , \hat{a}_5 and \hat{a}_6 have a known initial value that is equal to the inertia torque of the sensing element for the unloaded state.

The inertia torques I_{xx} , I_{yy} and I_{zz} can be determined by measuring the frequency response of the transfer function (3.123) for the directions θ_x , θ_y and θ_z separately. The measured frequency response for the direction i is given as $|\hat{G}_{Ci}(j\omega)|$, and the inertia torque in this direction can be determined by finding an a_i that minimizes the following quadratic error:

$$\varepsilon_i = \int_{\omega_{\min}}^{\omega_{\max}} (|\hat{G}_{Ci}(j\omega)| - |G_{Ci}(j\omega)|)^2 d\omega \quad (3.124)$$

where $|G_{Ci}(j\omega)|$ is the frequency response of the analytic transfer function (3.123). ω_{\min} and ω_{\max} comprise the interval of frequencies in which this identification procedure is applied.

By performing these three identification steps, the system parameters are determined and the optimized controller can be implemented in the multicomponent transducer. In the next section, the system's measurement resolution is analyzed for the sets of control parameters presented in table 3.2.

3.3.5 IMPLEMENTATION RESULTS

The behavior of the multicomponent transducer was analyzed for the control parameters shown in table 3.2. Figures 3.21 and 3.22 show the main results obtained, where the standard deviation of the force and torque measurement is evaluated for the different sets of control parameters. In these figures, both original and filtered signals are displayed. A simple moving average was used for filtering the signals, and the filter order was chosen in a way that the filter cut frequency matches the transducer natural frequency. These results show that original and filtered signals differ in about one order of magnitude, and

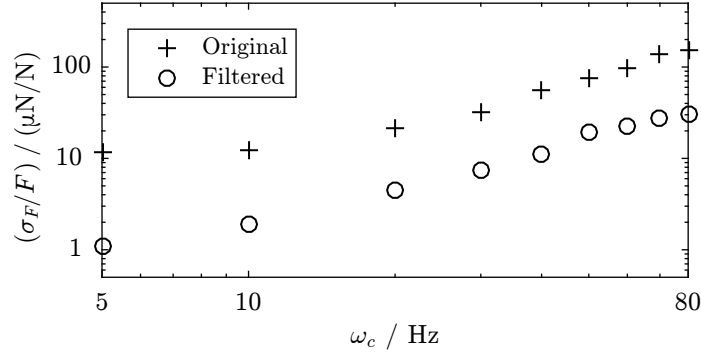


FIGURE 3.21: Standard deviation of the force signal relative to the measuring range for the x direction as a function of the natural frequency ω_c .

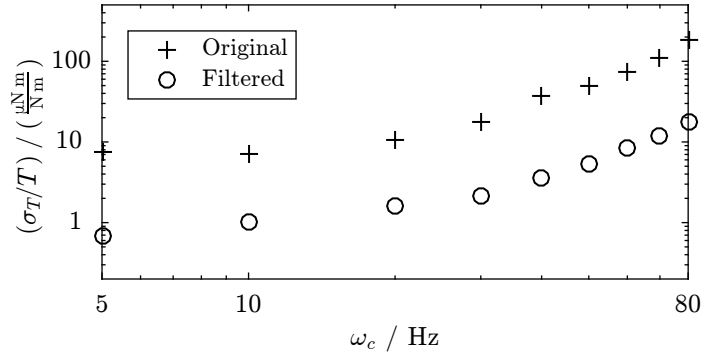


FIGURE 3.22: Standard deviation of the torque signal relative to the measuring range for the z direction as a function of the natural frequency ω_c .

the achievable type A standard uncertainty depends on the natural frequency of the system. For $\omega_c = 80$ Hz, a relative standard deviation of about 30 ppm for the force and 20 ppm for the torque can be achieved, and for $\omega_c = 5$ Hz, these standard deviations are reduced to 1.1 ppm and 0.7 ppm respectively.

The dependence of the standard deviation of the measurement signal on the position noise amplification factor f_G is shown in figure 3.23. All measurements contained in this figure were performed for a system's natural frequency equal to 10 Hz, and both original and filtered signals are displayed. These results confirm the hypotheses that the position noise amplification factor f_G correlates with the standard deviation of the measurement signal, and the possibility to improve the type A standard uncertainty by minimizing f_G .

3.3.6 HYBRID POSITION AND FORCE CONTROL

As described in [7], a multicomponent transducer based on the principle of the electromagnetic force compensation [12] was used to perform a surface micromachining task and simultaneously measure the contact forces and torques between the engraving tool and the surface to be processed. This transducer is very similar

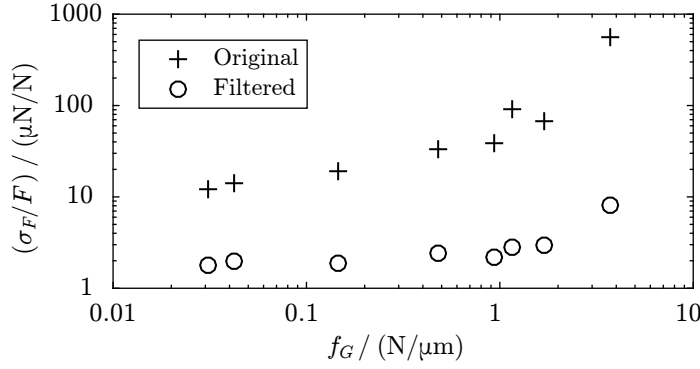


FIGURE 3.23: Standard deviation of the force signal relative to the measuring range for the x direction as a function of the position noise amplification factor. Measurements performed for eigenfrequency $\omega_c = 10$ Hz.

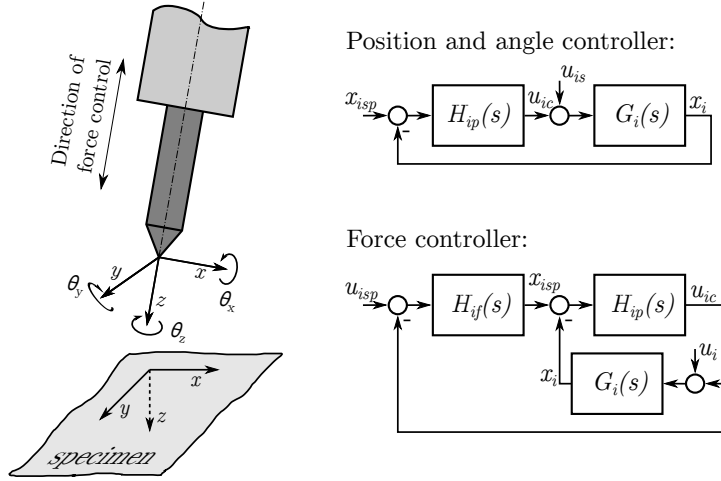


FIGURE 3.24: Control systems implemented in the multicomponent transducer for performing the micromachining tasks.

to the instrument described here, but it does not contain the calibration system and can only operate in the sensing mode. In order to accomplish the micromachining task, two types of control systems were used for the different degrees of freedom: for the linear motion in the direction of the tool tip axis, a force control system was implemented to regulate the contact force, and for the other five directions, position and angle control systems were used. By controlling the contact force, the penetration depth of the engraving tool is changed and, with the position/angle control system, the engraving tool can be moved according to a specified path.

Figure 3.24 contains the engraving tool with a reference frame fixed to its tip. On the right hand side of this figure, the structures of both control systems are shown. The control plant is represented by the transfer function $G_i(s)$, where $i = 1, \dots, 6$ indicates the degree of freedom considered. The degrees of freedom 1, 2 and 3 correspond to the linear directions x , y and z respectively, and the degrees of freedom 4, 5 and 6 correspond to the angular directions θ_x , θ_y and θ_z respectively. The position/angle controller, which is implemented for all directions excluding

z , is a simple feedback control strategy with a PID controller:

$$H_{ip}(s) = K_{Pip} + K_{Iip} \frac{1}{s} + K_{Dip} \frac{1}{N_{ip}s + 1} \quad (3.125)$$

where K_{Pip} , K_{Iip} , K_{Dip} and N_{ip} correspond to the gains of the position control system. For controlling for contact force between the specimen and the engraving tool a force feedback combined with a position feedback control system was used in a similar way as suggested in [78]. The transfer function $H_{ip}(s)$ for the position controller is the same as shown in equation (3.125) and the transfer function for the force feedback is given as:

$$H_{if}(s) = K_{Pif} + K_{Iif} \frac{1}{s} + K_{Dif} \frac{1}{N_{if}s + 1} \quad (3.126)$$

where K_{Pif} , K_{Iif} , K_{Dif} and N_{if} correspond to the gains of the force feedback controller. The results obtained for this application of the multicomponent transducer are described in section 6.3.

CHAPTER 4

EVALUATION OF THE MEASUREMENT UNCERTAINTY

The traceable force and torque measurements with the multicomponent transducer with integrated calibration depend on the traceable position, angle, voltage, resistance and time measurements. In this chapter, the calibration of these single components is described with the determination of the respective measurement uncertainties. This information is used to determine an uncertainty budget for the system and identify the biggest uncertainty contributions to the force and torque measurements.

4.1 POSITION AND ANGLE MEASUREMENT

As described in the previous chapter, during the velocity mode the levitating element moves with a sine wave reference trajectory and the determination of the amplitude of movement is fundamental for the traceable force and torque measurements. For this reason, the position and angle measuring system with the aperture slits, which is integrated in the multicomponent transducer, must be calibrated. A description on this calibration procedure is provided in this section, together with the compensation of nonlinearities and cross-talk effects. Additionally, several aspects for the traceable position measurement with laser interferometer based techniques is shown.

The matrices \mathbf{K}_{p1} , \mathbf{K}_{p2} and \mathbf{K}_{p3} of equation (3.79), which are used in the mathematical model of the aperture slit sensors, must be determined for the accurate position and angle measurement [79]. With the objective to determine the components of these matrices, the measuring setup of figure 4.1 is used. It is composed by a triple beam laser interferometer (TBLI, appendix A), a plane mirror, the multicomponent transducer and a two-axis linear stage (LS2A, appendix A). This measuring setup is inside a climate chamber with controlled temperature, and a table with pneumatic vibration isolation system is used to avoid effects of ground vibrations. In the configuration of figure 4.1 the transducer is assembled with the z direction pointing down along the vertical direction. With this setup it is possible to mount the transducer with the directions x and y also parallel to the vertical or laser direction. This is necessary in order to obtain the full calibration matrix of the transducer considering all components. The linear stage with two axis is used to determine deviations caused by assembly imperfections of the plane mirror. With this stage it was possible to determine that the mirror has a tilt of about $270\mu\text{rad}$ relative to the horizontal direction. Measurement

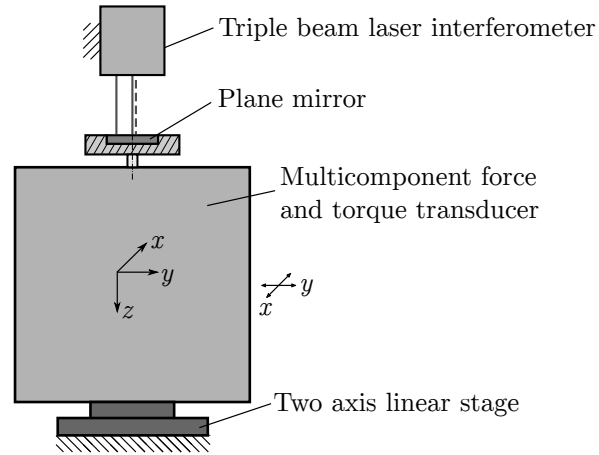


FIGURE 4.1: Experimental setup used for the calibration of the position measuring system.

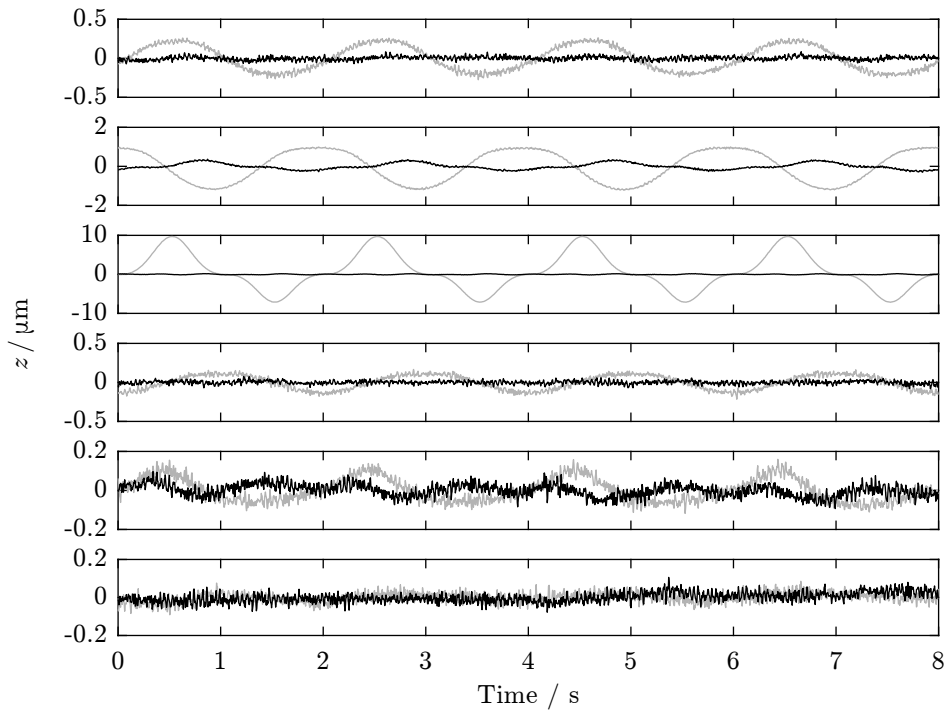


FIGURE 4.2: Component z of the mirror position for movement along different directions. Black color represents the measurements after calibration and gray color before calibration. From up to down: movement in x , y , z , θ_x , θ_y and θ_z directions. A sine wave function with frequency of 0.5 Hz and amplitude of $90\text{ }\mu\text{m}$ or $340\text{ }\mu\text{rad}$ was used as reference trajectory. For the movement in z direction the error relative to the reference trajectory is plotted.

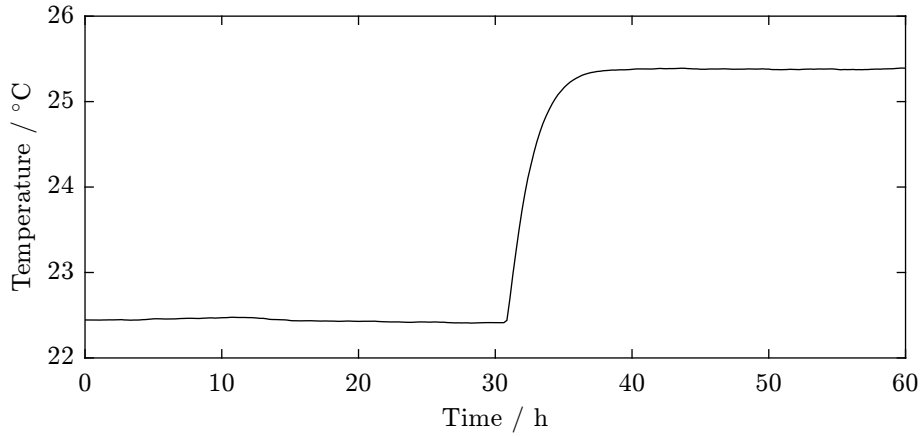


FIGURE 4.3: Temperature measured inside the multicomponent transducer.

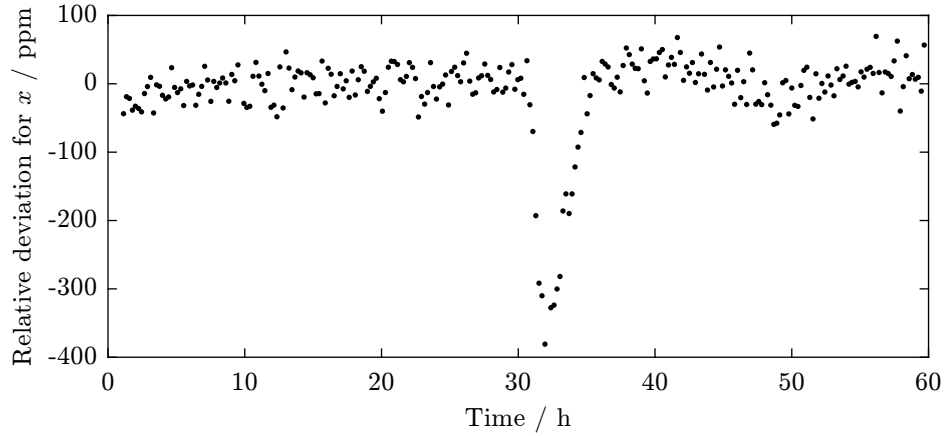


FIGURE 4.4: Deviation between the position measurement with the aperture slit sensor and the laser interferometer.

deviations caused by imperfections in the stage are considerably smaller than the measured tilt and could be neglected. For measuring the cross talk between the different position components this tilt can cause a maximal error of 24 nm. Figure 4.2 shows measurements performed with the transducer mounted as shown in figure 4.1. With the triple beam laser interferometer, the displacement of the mirror along the z direction and the angles θ_x and θ_y can be measured. The results shown here are for six measurements performed considering the z direction. In these measurements, the sensing element of the transducer was moved in all directions. For the directions x , y , θ_x , θ_y and θ_z , the cross talk of the position measurement system was determined and for the z direction the calibration was performed. The transducer was also mounted with the x and y axes parallel to the laser direction and these measurements were repeated. The information obtained was used to determine the matrices \mathbf{K}_{p1} , \mathbf{K}_{p2} and \mathbf{K}_{p3} . In figure 4.2, measurements in gray color were performed before the calibration and measurements in black color were performed after the calibration. The reduction of the cross talk in directions x , y , θ_x and θ_y can be observed in this figure. For the

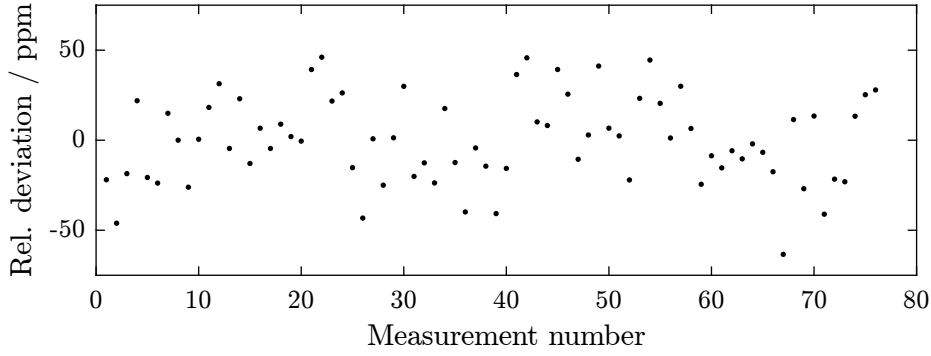


FIGURE 4.5: Repeatability for the position amplitude measurement with the laser interferometer.

z direction, nonlinearities in the position transducer were compensated and the original measurement deviation of about 11 % could be eliminated.

The system was moved with sine wave trajectory with an amplitude of about $32\text{ }\mu\text{m}$ and frequency 10 Hz. With the objective to evaluate the uncertainty for the position measurement during the calibration mode, the amplitude of the movement was measured by using both integrated position sensor and laser interferometer. The temperature was measured inside the transducer and, in order to obtain the results shown here, a temperature compensation was applied. The measurements were repeated for 60 h with a time interval of about 10 min between each measurement. Figure 4.3 shows the temperature measured inside the transducer. For the first half of the measurements, the ambient temperature was controlled at 20°C and, for the second half, 23°C . The temperature inside the transducer is about 2.4°C higher than the ambient temperature. Figure 4.4 shows the relative deviation between the position measurement with the laser interferometer and the aperture slit sensors. A standard deviation of 34 ppm was obtained for this measurements. This value is not considering the first 21 measurements performed after the temperature change. Several aspects influence the uncertainty for the position and angle measurement with the aperture slit sensors. For the traceable position measurement with the aperture slit sensors it is important to have a stable mechanical hardware. Deformations of the aperture slit or changes in mechanical connections can change the calibration parameters for the position measurement.

The laser interferometer can not only be used for measuring the nonlinearities and cross coupling in the position sensors. It is also possible to measure the position of the sensing element during the velocity mode in order to obtain a traceable position measurement. The repeatability of the position measurement with the laser interferometer can be evaluated by using the measurement result shown in figure 4.5. For this measurement an experimental setup very similar to the system shown in figure 4.1 was used, but with a one-beam laser interferometer (SBLI, appendix A). In these measurements the sensing element was moved with a sine-wave trajectory, with $36\text{ }\mu\text{m}$ amplitude and 10 Hz frequency. The relative deviation for the determination of the translation amplitude is shown in figure 4.5. The measurements were repeated several times and a standard deviation smaller

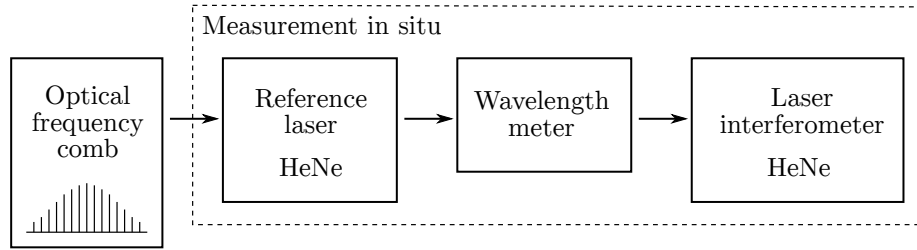


FIGURE 4.6: Procedure used for the traceable measurement of the laser frequency for the laser interferometer.

than 25 ppm was obtained. This standard deviation is used to quantify the measurement repeatability for the translation amplitude. The uncertainty for the angle measurement with the laser interferometer was analyzed as well. Although a one-beam laser interferometer was used, the angle measurement was possible by moving the transducer with the linear stage. In this case, the positioning precision of the linear stage is relevant for the angle determination. According to datasheet information, the linear stage is equipped with an optical linear encoder capable of measuring the position with an uncertainty smaller than 1 μm . For the moving range of 20 mm used during the measurements, that represents a maximal relative uncertainty of 50 ppm. An additional difficulty for measuring the angle with the laser interferometer and plane mirror is the maximal range of motion. Angles up to 0.43' with a repeatability of 450 ppm can be measured with this setup. This repeatability was experimentally determined by using a procedure similar to the determination of the repeatability for the translation amplitude.

Some other important aspects must be regarded for the position measurement with the laser interferometer. Since the position of the geometric center of the sensing element is measured, it is necessary to align the beam with this point in order to avoid measuring deviations caused due to Abbe error. The laser frequency of the laser interferometer must be stable and known within the uncertainty level required. Since the measurements are performed in air, it is also necessary to determine the laser wavelength for these conditions. The measurement of the laser frequency and the determination of the laser wavelength in air are described in the next sections.

4.1.1 MEASUREMENT OF THE LASER FREQUENCY

The frequency of the laser source used in the laser interferometer has to be precisely determined in order to obtain a traceable position measurement. The frequency was measured by using a wavelength meter (WLMET, appendix A), which was previously calibrated by using a calibrated reference HeNe laser (HENEL, appendix A). This procedure is shown in figure 4.6. The frequency f_{ref} of the reference laser was previously determined in a measurement performed with an optical frequency comb (FRCMB, appendix A) and its value is 473 612 541 MHz \pm 2 MHz.

The frequency of the laser interferometer was measured by using this procedure. Table 4.1 shows the measurement results, with the frequency of the reference laser, the wavemeter readouts for both interferometer and reference laser and the frequency of the laser interferometer. The uncertainty contributions are

TABLE 4.1: Uncertainty budget for the laser frequency measurement.

Quantity	Value	Standard uncertainty	Distribution	Uncertainty contribution
f_{ref}	473 612 541 MHz	2 MHz	square	12 %
\hat{f}_{int}	473 612 321 MHz	4 MHz	square	44 %
\hat{f}_{ref}	473 612 097 MHz	4 MHz	square	44 %
f_{int}	473 612 765 MHz	7 MHz		

also shown in this table. The frequency of the laser interferometer was measured equal to 473 612 765 MHz \pm 7 MHz.

The laser frequency of the interferometer can be determined by using the following expression:

$$f_{\text{int}} = f_{\text{ref}} \frac{\hat{f}_{\text{int}}}{\hat{f}_{\text{ref}}} \quad (4.1)$$

where \hat{f}_{int} and \hat{f}_{ref} are the readouts of the wavelength meter.

4.1.2 LASER WAVELENGTH DETERMINATION IN AIR

Since the measurements are performed in air, the laser wavelength λ for the laser interferometer has to be determined for this condition. This is done by evaluating the air refractive index n as in [80] and using the following equation to determine the laser wavelength in air:

$$\lambda = \frac{c}{nf_{\text{int}}} \quad (4.2)$$

where $c = 299\,792\,458$ m/s is the speed of light in vacuum and f_{int} is the laser frequency as determined in the previous section. The refractive index depends on the laser frequency, the air temperature, the relative humidity, the air pressure and the concentration of CO₂. Two methods are used to determine the refractive index with this information: the Ciddor and the Edlén equations. Table 4.2 shows the uncertainty for the determination of the refractive index and wavelength in air by using both methods. These uncertainties were obtained by using the Guide to the Expression of Uncertainty in Measurement [81] and neglecting correlations between the random variables related to the physical quantities. The uncertainties of both equations were neglected as well. The temperature, the relative humidity and the air pressure are measured by using the integrated PHT module of the sensing unit. The uncertainties for the measurement by using this sensor are also shown in table 4.2. For the concentration of CO₂ an estimated value of 3500 $\mu\text{mol/mol}$ with a rectangular uncertainty distribution and limit half-width of 3000 $\mu\text{mol/mol}$ is used. The laser wavelength has an uncertainty contribution smaller than 1.2 ppm for the position measurement with the laser interferometer in air.

TABLE 4.2: Determination of the measurement uncertainty for the air refractive index.

Quantity	Standard uncertainty	Contribution	
		Ciddor	Edlén
Temperature	1.15 °C	84.8 %	89.2 %
Laser Frequency	7 MHz	0.0 %	0.0 %
Relative humidity	17.3 %	3.6 %	2.9 %
Air pressure	115 Pa	7.4 %	7.9 %
Concentration of CO ₂	1730 µmol/mol	4.2 %	-
n_{Ciddor}	1.12×10^{-6}		
$n_{\text{Edlén}}$	1.09×10^{-6}		
λ_{Ciddor}	0.71 pm		
$\lambda_{\text{Edlén}}$	0.69 pm		

The position measured with the laser interferometer is basically obtained by using the following expression:

$$x_{\text{int}} = \frac{\lambda}{2} n_{\text{fringes}} \quad (4.3)$$

where $n_{\text{fringes}} \in \mathbb{R}$ is the interpolated number of fringes measured with the laser interferometer. For this expression, the offset path difference between the laser beams reflected by reference mirror and measurement mirror was neglected. The quantity n_{fringes} has an uncertainty contribution of type A and it is assumed to have a relative standard uncertainty equal to 25 ppm, which is the value obtained with the result shown in figure 4.5. In this way, the combined standard uncertainty for the measurement of the position amplitude with the laser interferometer can be determined. The measurement of the fringes is the biggest uncertainty contribution and the standard uncertainty is equal to 25 ppm as well. For the angle amplitude measurement with the laser interferometer and linear stage a combined standard uncertainty of 453 ppm is obtained considering the maximal range of motion of 0.43'. The relative standard uncertainty for the angle amplitude measurement is bigger than the uncertainty for the translation amplitude by a factor of almost 20. This uncertainty can be improved by using retroreflectors instead of a plane mirror, in a way to increase the range of motion and reduce the relative measurement repeatability. A two-beam laser interferometer can be used as well to eliminate uncertainty contributions from the linear stage.

4.2 VOLTAGE MEASUREMENT

The measurement of the induced voltages in the coils is necessary during the calibration mode and the measurement of the voltage drop in the resistors is necessary during the sensing mode. There are basically two possibilities for the voltage measurement used in this work: the use of the analog to digital converters

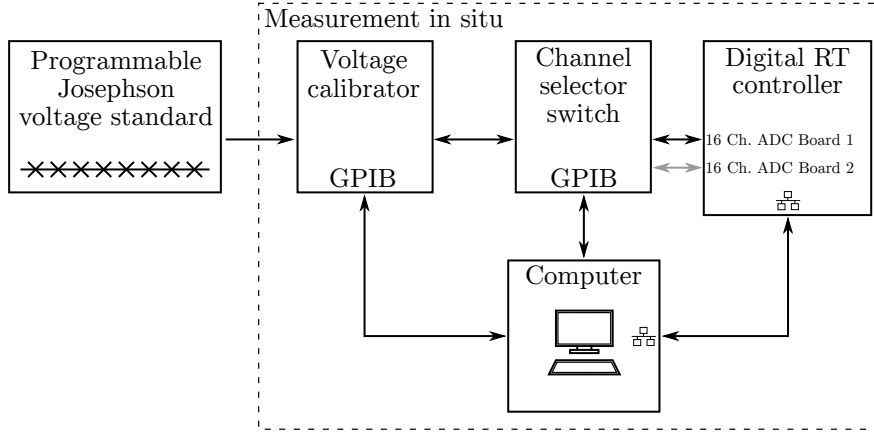


FIGURE 4.7: Experimental setup used for the calibration of the voltage measuring system.

(ADC-B, appendix A) of the real-time controller and the use of a precision digital voltmeter (DVM, appendix A). With the ADC all voltages can be measured simultaneously, however problems of nonlinearities limit the achievable uncertainty for the measurement. The multichannel voltage measurement with the digital voltmeter is possible by using a measurement scanner but, in this case, the simultaneous measurement is not possible. There are three main aspects for the voltage measurement with these devices which contribute to the overall measurement uncertainty: the measurement resolution, the linearity of the instrument and the long-term stability.

The voltage measuring system integrated in the real-time controller is composed by two boards with 16 successive-approximation-register (SAR) analog to digital converters each. Each converter has a measuring resolution of 16 bits and the measuring ranges can be adjusted to ± 5 V, ± 10 V or 0 V to 10 V. The minimal theoretical resolution which can be achieved for one sample is approximately 153 μ V. By using oversampling techniques, such as described in [82], this resolution can be improved to 3 μ V. In order to obtain a consistent voltage measurement, it is necessary to calibrate these ADCs. The following expression is used to describe each converter:

$$u_i = a_i \hat{u}_i + b_i \quad (4.4)$$

where \hat{u}_i is the output of the ADC, a_i is the linear gain of the converter, b_i is the offset and u_i is the calibrated voltage. The measuring setup of figure 4.7 is used to determine the coefficients a_i and calibrate the voltage measuring system of the real-time controller. This setup is composed by a voltage calibrator (VCAL, appendix A), a channel selector switch (MCSCN, appendix A), the real-time controller and a computer. The voltage calibrator was previously calibrated by using a programmable Josephson voltage standard system. This system uses the conventional value of the Josephson constant K_{J-90} to represent the unit volt [83]. With the computer all devices can be controlled automatically and the measurement data can be acquired. Figure 4.8 shows experimental results obtained with this setup. For each measurement a calibration of the ADC channels was

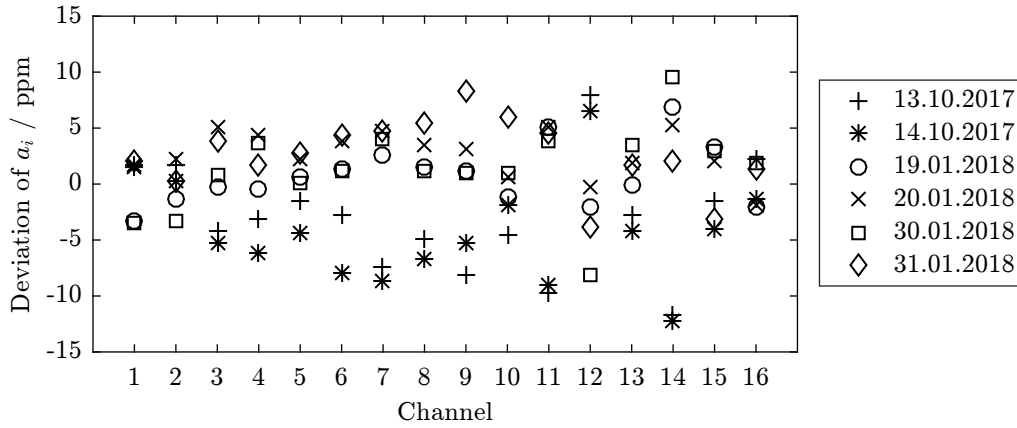


FIGURE 4.8: Deviation of the gain a_i for the ADC channels of board 2. Six calibrations were performed in different days.

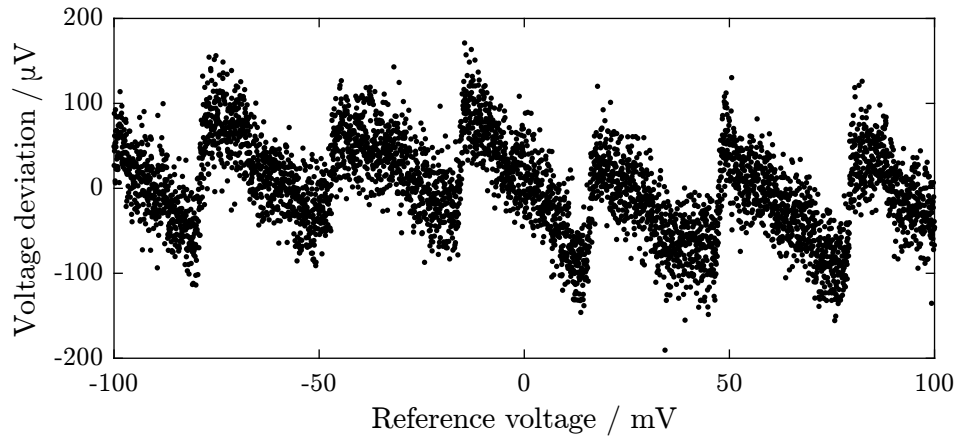


FIGURE 4.9: Deviation of the analog-to-digital converter relative to the digital voltmeter.

performed by using defined voltage levels between -10 V and 10 V in steps of 1 V . The deviations of the calibration parameters a_i for the 16 channels of the ADC board 2 are shown in figure 4.8. These deviations are relative to the mean values of all measurements performed. A maximal deviation of about 12.5 ppm was obtained for the channel 14. For the measurement procedure used in the multicomponent transducer it is not necessary to determine the offset voltages of the instruments. For this reason the coefficients b_i of equation (4.4) are not measured here. However, by using the same procedure, it is also possible to determine these coefficients for other applications.

The results of figure 4.8 can be used to evaluate the time stability of the analog to digital converters of the integrated voltage measuring system. A further aspect which is very relevant is the linearity of the converters. This linearity was evaluated by using an experimental setup very similar to the system shown in figure 4.7, however, instead of the voltage calibrator, a programmable signal generator was used to generate a reference voltage level. Since for this experiment

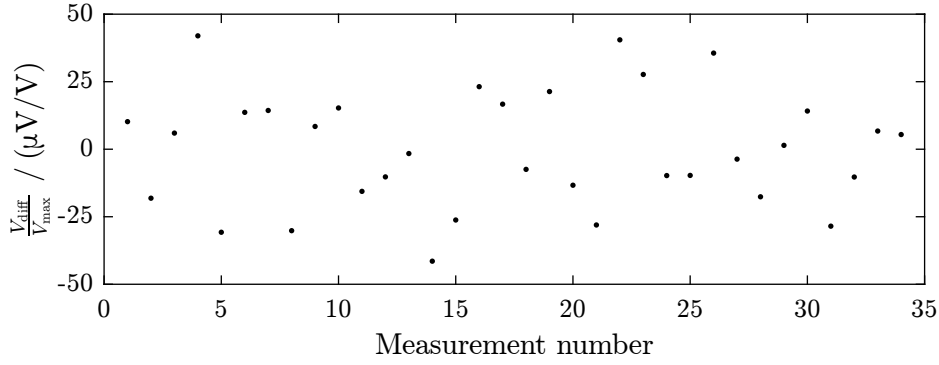


FIGURE 4.10: Repeatability for the measurement of the induced voltage amplitude with the digital voltmeter.

no traceable voltage measurement is necessary, this signal generator was not previously calibrated. Voltage levels in a range of -0.1 V to 0.1 V were measured with the ADC and a precision digital voltmeter. Figure 4.9 shows the measurement results obtained for 5000 voltage levels uniformly distributed in the range mentioned. In this figure, the deviation of the measurements obtained with both instruments is shown as a function of the voltage level applied. Deviations with a sawtooth wave format in a range from $-180\text{ }\mu\text{V}$ to $180\text{ }\mu\text{V}$ can be observed. For the ranges of $\pm 5\text{ V}$ and $\pm 1\text{ V}$ this represents a relative deviation of 36 ppm and 180 ppm respectively. These values for the linearity deviation are consistent with information from the device datasheet.

Another possibility for the voltage measurement is using the digital voltmeter DVM listed in appendix A. Such device has been used in several fields of measuring technology and its performance has been evaluated since several years. This device is also employed in Kibble balance experiments [52]. With this instrument it is possible to measure voltages with a relative uncertainty smaller than 10 ppm for the voltage range of 0.1 V and 6.3 ppm for the voltage range of 1 V . These uncertainty values are determined by the specifications in the datasheet of the digital voltmeter and already consider the aspects of stability, linearity and resolution. For the measurement of the induced voltages in the electromagnetic actuators a different method is used. The induced voltages have a sine wave form and the amplitude of these voltages is determined by fitting a sine wave function to the data measured. Figure 4.10 shows measurement results obtained with this procedure. The voltage measured has originally a frequency of about 10 Hz and an amplitude of about 49 mV . With this measurement result it is possible to evaluate the repeatability for the determination of the induced voltage amplitude, which is approximately 21.5 ppm. In order to obtain the uncertainty for the induced voltage amplitude, the repeatability is combined with the 10 ppm of the voltmeter and the value obtained is approximately 24 ppm.

4.3 RESISTANCE MEASUREMENT

The traceable current measurement is a requirement for the force and torque measurement with the multicomponent transducer. The current measurement

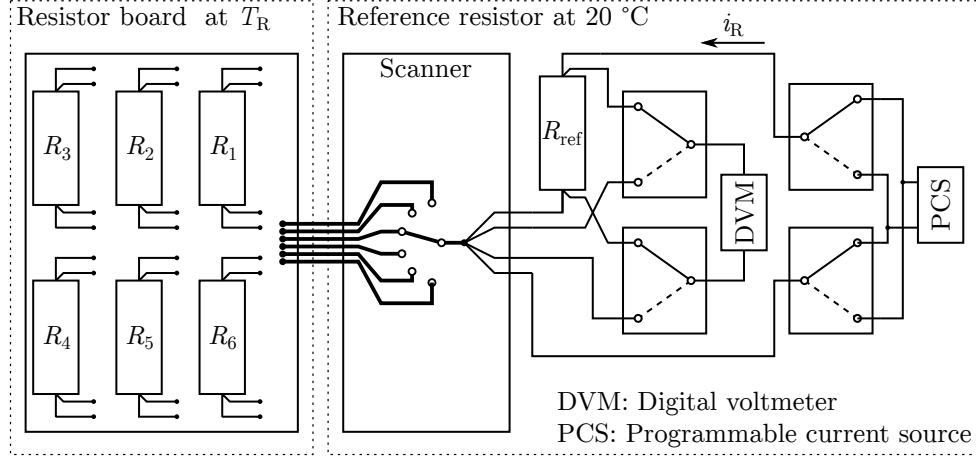


FIGURE 4.11: Measuring setup for the calibration of the resistor board of the multicomponent transducer.

is performed by measuring the voltage drop caused by the currents in reference resistors. For this reason it is necessary to calibrate the resistors used in the system and determine the uncertainties for the respective values of electrical resistance.

Two resistor boards composed by six resistors each are used for the measurement of twelve electrical currents. By using the Ohm's law:

$$V_k = R_k i_k, \quad (4.5)$$

where $k = \{1, \dots, 6\}$ correspond to the resistors of the board 1 and $k = \{7, \dots, 12\}$ correspond to the resistors of the board 2. If the electrical resistance R_k is known, the electrical current i_k can be determined by measuring the voltage V_k . It is known that external temperature differences and self-heating caused by the electrical current change the electrical resistance. Additionally to this temperature dependency, the resistance values are also subject to a time drift. According to information provided by the manufacturer of the resistors, these components have a stabilization time of about four weeks after mounting on a printed circuit board. In this time period, deviations of the resistance value of some ppm can be observed. The electrical resistance of each resistor is given as:

$$R_k = R_k^{\text{cal}} (1 + \alpha_T(\Delta T) + \alpha_i(\Delta i) + \alpha_t(\Delta t)) \quad (4.6)$$

The quantity R_k^{cal} describes the resistance value obtained during the calibration and the quantities ΔT , Δi and Δt are the temperature, electrical current and time differences between calibration and measurement conditions. The functions α_T , α_i and α_t describe the dependency of the electrical resistance on external temperature changes, self-heating due to electrical current and time respectively. The oil filled and hermetically sealed resistors used exhibit a very low air pressure and humidity dependency and, for this reason, these effects are neglected.

The measuring setup of figure 4.11 was used to calibrate the resistor boards of the multicomponent transducer. It is composed by a calibrated reference resistor, a digital voltmeter (DVM, appendix A), a programmable current source (PCS,

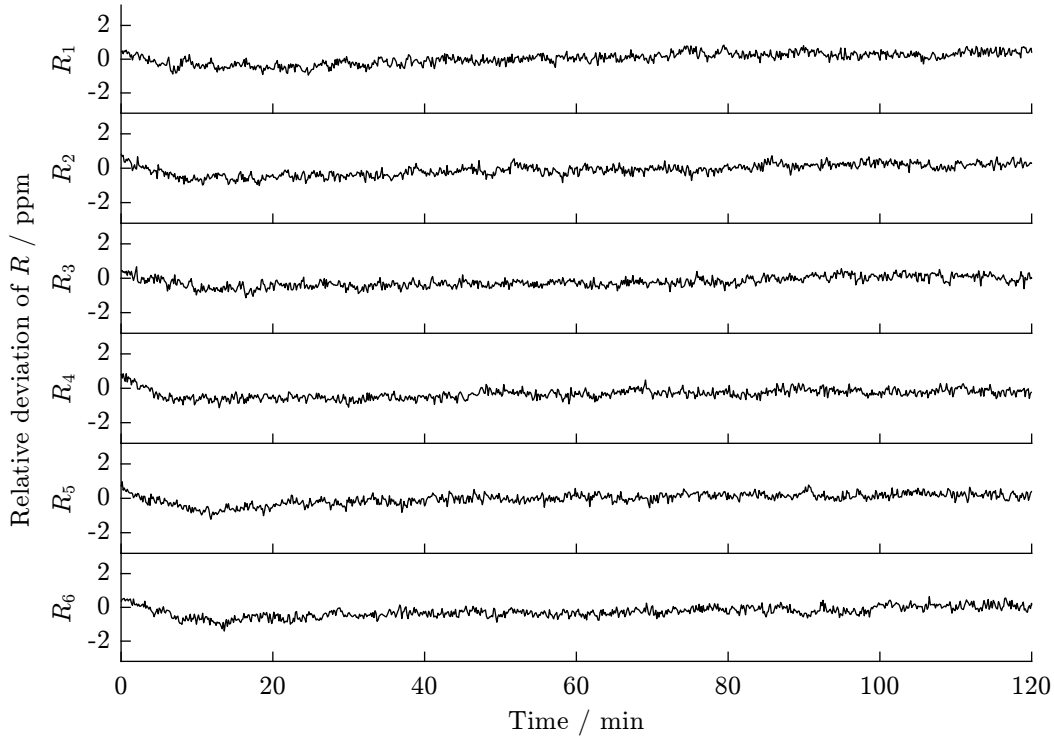


FIGURE 4.12: Relative deviation of the resistance measured in the resistors during a self heating test for a current step of 100 mA.

appendix A), a switching system with a scanner (MCSCN, appendix A) and four relays. The resistor board is located inside a polystyrene box for temperature isolation together with a heating system. In this way, it is possible to perform the calibration of the resistors in conditions very similar to the normal operation during the force/torque measurement with the transducer. The resistor board is connected to the scanner, which is used to select one of the six resistors to be calibrated. The measurement is performed with a four-terminal sensing method and the current-carrying/voltage-sensing electrodes are separated. The PCS, the reference resistor and the resistor to be calibrated are connected in series. With two relays it is possible to invert the direction of the current flowing in the resistors. This is performed in order to eliminate effects caused by thermal electromotive forces generated in the voltage-sensing circuit. The voltage drop in both reference resistor and test resistor have to be measured. This is done with a digital voltmeter connected to two relays. During the calibrations a current $i = 1 \text{ mA}$ was generated by the PCS. The voltage measured in the test resistor k for a positive current direction is given by:

$$V_k^+ = a_1 V_{Rk} + V_0 = a_1 R_k^{\text{cal}} i + V_0 \quad (4.7)$$

The calibration factor of the DVM is given by a_1 , V_0 is an offset voltage, which includes thermal electromotive forces generated in the voltage-sensing circuit and V_{Rk} is the voltage drop in the test resistor caused by the current. The voltage

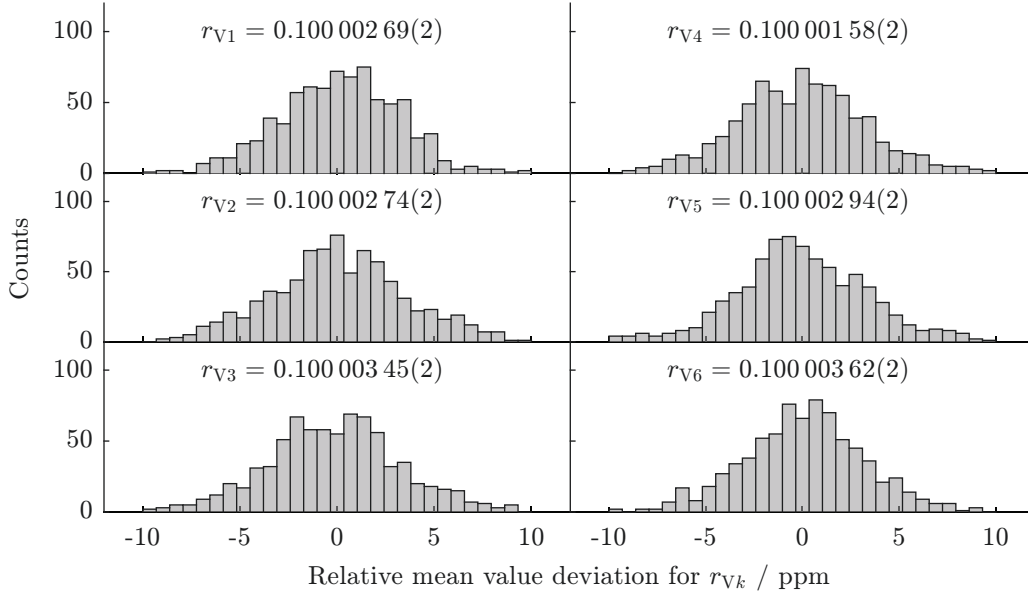


FIGURE 4.13: Values measured for the voltage ratio coefficient r_{V_k} of the six resistors.

measured in the same resistors for the negative current direction is given by:

$$V_k^- = -a_1 V_{Rk} + V_0 = -a_1 R_k^{\text{cal}} i + V_0 \quad (4.8)$$

The following voltages are measured for the reference resistor R_{ref} in positive and negative current directions respectively:

$$V_{\text{ref}}^+ = a_1 V_R + V_0 = a_1 R_{\text{ref}} i + V_0 \quad (4.9)$$

$$V_{\text{ref}}^- = -a_1 V_R + V_0 = -a_1 R_{\text{ref}} i + V_0 \quad (4.10)$$

By using equations (4.7), (4.8), (4.9) and (4.10), the following expression can be obtained for the determination of the electrical resistance R_k^{cal} :

$$R_k^{\text{cal}} = \frac{V_k^+ - V_k^-}{V_{\text{ref}}^+ - V_{\text{ref}}^-} R_{\text{ref}} = r_{V_k} R_{\text{ref}} \quad (4.11)$$

The reference resistor is the same type as the resistors of the resistor board but it has a nominal value of 100Ω . Its electrical resistance also depends on the temperature, electrical current and time:

$$R_{\text{ref}} = R_{\text{ref}}^{\text{cal}} (1 + \alpha_{T,\text{ref}}(\Delta T) + \alpha_{i,\text{ref}}(\Delta i) + \alpha_{t,\text{ref}}(\Delta t)) \quad (4.12)$$

Finally, by using equations (4.6), (4.11) and (4.12), the following expression which describes the resistance value during the current measurement task can be obtained:

$$R_k = r_{V_k} R_{\text{ref}}^{\text{cal}} (1 + \hat{\alpha}_{T,\text{ref}} + \hat{\alpha}_{i,\text{ref}} + \hat{\alpha}_{t,\text{ref}}) (1 + \hat{\alpha}_T + \hat{\alpha}_i + \hat{\alpha}_t) \quad (4.13)$$

The quantities $\hat{\alpha}_{T,\text{ref}}$, $\hat{\alpha}_{i,\text{ref}}$ and $\hat{\alpha}_{t,\text{ref}}$ represent the evaluation of the functions

TABLE 4.3: Resistance values and respective uncertainties for the resistor board 1.

Quantity	Value	Standard uncertainty	Distribution	Uncertainty contribution
r_{V_k}	from figure 4.13	2×10^{-8}	normal	1.1 %
$R_{\text{ref}}^{\text{cal}}$	100.000 177 4 Ω	0.000 001 0 Ω	normal	0.0 %
$\hat{\alpha}_{\text{T,ref}}$	0.000 000 00	0.000 000 23	rectangular	1.5 %
$\hat{\alpha}_{\text{i,ref}}$	0.000 000 00	0.000 000 00	rectangular	0.0 %
$\hat{\alpha}_{\text{t,ref}}$	0.000 000 00	0.000 000 92	rectangular	23.6 %
$\hat{\alpha}_{\text{T}}$	0.000 000 00	0.000 000 69	rectangular	13.3 %
$\hat{\alpha}_{\text{i}}$	0.000 000 00	0.000 001 15	rectangular	36.9 %
$\hat{\alpha}_{\text{t}}$	0.000 000 00	0.000 000 92	rectangular	23.6 %
R_1	10.000 287 Ω	0.000 019 Ω		
R_2	10.000 292 Ω	0.000 019 Ω		
R_3	10.000 363 Ω	0.000 019 Ω		
R_4	10.000 176 Ω	0.000 019 Ω		
R_5	10.000 312 Ω	0.000 019 Ω		
R_6	10.000 380 Ω	0.000 019 Ω		

$\alpha_{\text{T,ref}}$, $\alpha_{\text{i,ref}}$ and $\alpha_{\text{t,ref}}$ for the measurement conditions during calibration of the resistor board and the quantities $\hat{\alpha}_{\text{T}}$, $\hat{\alpha}_{\text{i}}$ and $\hat{\alpha}_{\text{t}}$ represent the evaluation of the functions α_{T} , α_{i} and α_{t} for the measurement conditions during transducer operation. With this measurement procedure the resistance values of the test resistors are traced exclusively to the reference resistor R_{ref} . The determination of the calibration coefficients of the DVM and the traceable current measurement are not required in order to measure the resistance values. It is only necessary to measure the voltage ratio coefficient r_{V_k} for each resistor, which is a dimensionless quantity, and estimate how much the operation and calibration conditions differ. The resistance value of the reference resistor is given in a calibration certificate with a respective uncertainty.

According to the calibration certificate, the reference resistor was originally calibrated at $19.95^\circ\text{C} \pm 0.01^\circ\text{C}$ with a current of 1 mA. During the calibration, a value $R_{\text{ref}}^{\text{cal}} = 100.000\,177\,4(10)\,\Omega$ was obtained for the electrical resistance and a temperature dependency of about 0.4 ppm/K was identified. Since the current used during the calibration of the reference resistor is the same for the calibration of the resistor board, measurement deviations caused by self-heating can be neglected, i.e. $\hat{\alpha}_{\text{i,ref}} \approx 0$. During the calibration of the resistor board the reference resistor was at $20^\circ\text{C} \pm 1^\circ\text{C}$ and, in this way, $|\hat{\alpha}_{\text{T,ref}}| \leq 0.4$ ppm. During the calibration of the reference resistor a deviation of about 0.4 ppm/week was observed and, for a stabilization time of four weeks, a maximal deviation $|\hat{\alpha}_{\text{t,ref}}| \leq 1.6$ ppm is expected.

With the objective to determine the influences of self-heating in the resistor board a measurement was performed. Each resistor was submitted to a current step of 100 mA, which is the maximal current allowed during the operation of the

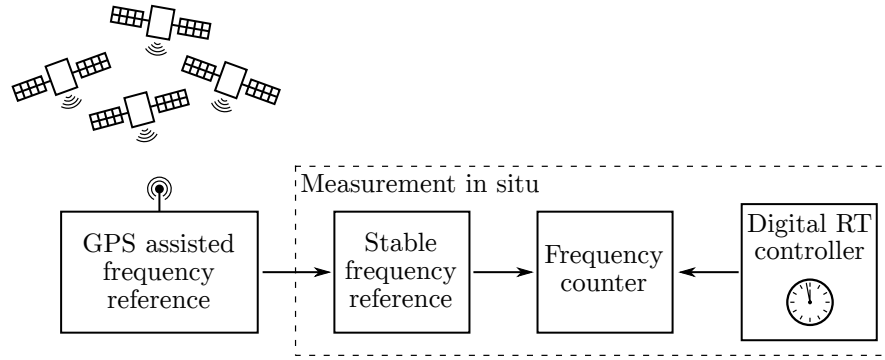


FIGURE 4.14: Setup used for the traceable time measurement.

multicomponent transducer, for two hours and the resistance value was determined by measuring the voltage drop. Figure 4.12 shows the relative resistance deviation in ppm for the six resistors. For these measurements, the deviations caused by the electrical current are smaller than 2 ppm. With this information, the parameter $\hat{\alpha}_i$ is assumed to have a magnitude smaller than 2 ppm. The voltage ratio r_{V_k} was measured for the resistors mounted in the resistor board and the values obtained are shown in figure 4.13. These measurements were performed at the temperature $T_R = 34.5^\circ\text{C}$ for the resistor board. For each resistor, the electrical resistance was measured 792 times in measurements repeated with a period of about 50 s. The uncertainties shown in figure 4.13 were determined by calculating the standard uncertainty for the mean values of the data sets and expanding these uncertainties by a factor of 3. The ambient temperature was changed with the objective to evaluate the temperature dependency and a maximal value of 0.4 ppm/K was observed. Maximal temperature deviations of 3°C are expected between calibration and measurement conditions and the parameter $\hat{\alpha}_T$ is assumed to have a magnitude smaller than 1.2 ppm. Effects caused by time drifts are also assumed to be in a range of 1.6 ppm for the resistors of the resistor board.

With all this information it is possible to determine the resistance values and the respective measurement uncertainties for the resistors according to the equation (4.13). The values obtained for the six resistor of the board 1 are shown in table 4.3. For this determination, the variables r_{V_k} and $R_{\text{ref}}^{\text{cal}}$ were assumed to have a normal distribution with standard uncertainties obtained from measurements and a calibration certificate respectively. The variables related to the measurement conditions were assumed to have a rectangular distribution.

4.4 TIME MEASUREMENT

A time measuring system is used to obtain a traceable time measurement, which is a requirement for the multicomponent force and torque measurements. Figure 4.14 shows the setup used for the time measurement. It is composed by a GPS assisted frequency reference (GPSFR, appendix A), a stable frequency reference, a frequency counter (FCTR, appendix A) and the digital real-time controller used to control the levitating element of the multicomponent transducer. The GPS

TABLE 4.4: Uncertainty budget for the determination of the frequency of movement.

Quantity	Value	Standard uncertainty	Contribution
f_{GPS}	10 000 000.00 Hz	0.03 Hz	99.8 %
f_{cal}	9 999 999.834 Hz	0.002 Hz	0.0 %
f_{RT}	4999.963 68 Hz	0.000 31 Hz	0.2 %
$\hat{\omega}$	10 Hz	-	-
ω	9.999 927 19 Hz	0.000 000 62 Hz	

frequency reference is used to calibrate the stable frequency reference, which contains a ultra stable timebase with temperature control. This is done by measuring the $f_{\text{GPS}} = 10$ MHz output frequency signal from the GPS reference. This frequency has an uncertainty of 5 ppb. The stable frequency reference has an aging rate smaller than 20 ppb per year and a turn-on stability of 5 ppb. This frequency reference is integrated in the frequency counter, which is used to measure the loop frequency of the real-time controller. A clock signal with nominal frequency of 5 kHz is generated by the real-time controller and measured with the counter. For a nominal frequency of movement $\hat{\omega}$, the real frequency of movement ω can be determined by using the following expression:

$$\omega = \hat{\omega} \frac{f_{\text{RT}}}{5 \text{ kHz}} \frac{f_{\text{cal}}}{f_{\text{GPS}}} \quad (4.14)$$

where f_{cal} is the frequency of the GPS assisted reference measured with the counter and f_{RT} is the frequency of the real-time controller also measured with the counter. Table 4.4 shows the uncertainty budget for the determination of the frequency of movement during the velocity mode. The frequency can be determined with a relative standard uncertainty of about 62 ppb.

4.5 FURTHER CONSIDERATIONS

In order to obtain a traceable force and torque measurement with the multicomponent transducer some other considerations are necessary. This includes variations in temperature, air pressure and humidity, the coil-current effect in the electromagnetic actuators and the inductive coupling between the coils. Variations in the temperature cause a change in the actuator constant of the electromagnetic actuators. If these changes are very small between the calibration mode and the sensing mode, these influences can be neglected. In case of significant temperature changes, the integrated temperature sensors can be used to compensate the variations of the actuator constant. The air density depends on the pressure, relative humidity and temperature. Variations in these quantities cause changes in the buoyancy force in the sensing element. These changes can cause measurement deviations in the force and torque measurements and the integrated air pressure, relative humidity and temperature sensors can be used to detect them.

The influences of the coil-current effect and the inductive coupling between the coils are described in the next sections.

4.5.1 COIL-CURRENT EFFECT

The coil-current effect is well-known for Kibble balance experiments and is described with details in [53]. This effect causes a current dependency of the actuator constant, which is given as:

$$k_{Bl} = k_{Bl0}(1 + k_{cc}i) \quad (4.15)$$

Measurement results obtained with the multicomponent transducer show that the coil-current effect is a relevant source of deviation for both force and torque measurements. These measurements are presented in section 5.2. The strategy used in this case is to measure the magnitude of k_{cc} in order to implement a compensation strategy. This quantity can be determined by using the weight force generated by a test mass of unknown value in association with different offset forces generated by the coils of group II. This procedure is described with details in the following.

Assuming the transducer is operating in sensing mode, as described in section 3.1, the coils I are used to control the position and angle of the sensing element and the coils II are used to generate offset forces. If the test mass is not used, there is no constant current flowing in coils I. For any of these coils we have theoretically:

$$i = 0 \quad (\text{without mass}). \quad (4.16)$$

When the test mass is placed on the sensing element, coils I automatically compensate the weight force generated by the test mass. Electrical currents flowing in the coils are responsible for compensating the weight of the test mass:

$$i = i_w \quad (\text{with mass}). \quad (4.17)$$

The coils II can also be used to generate an additional force in order to compensate the weight of the levitating element and cause an offset force, which is compensated by the coils I. In this case, the following currents flows in a coil of group I for the conditions without and with test mass:

$$i = i_{\text{off}} \quad (\text{with offset}) \quad (4.18)$$

$$i = i_{\text{off}} + i_w \quad (\text{with offset and mass}). \quad (4.19)$$

It is important to observe that, if the axis of the coil is perpendicular to the gravity acceleration direction, equation (4.19) is not valid.

The magnitude of the force generated by the same coil in the cases (4.18) and (4.19) is given as:

$$F_{\text{off}} = k_{Bl0}(1 + k_{cc}i_{\text{off}})i_{\text{off}} \quad (4.20)$$

$$F_{\text{off}} + F_w = k_{Bl0}(1 + k_{cc}(i_{\text{off}} + i_w))(i_{\text{off}} + i_w) \quad (4.21)$$

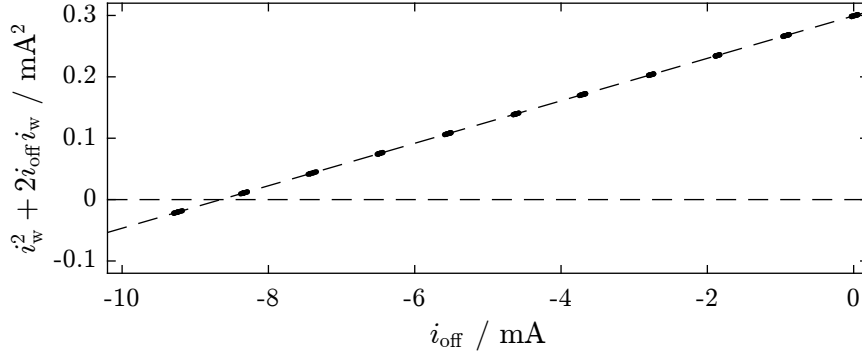


FIGURE 4.15: Measurement performed to determine $i_w^2 + 2i_{\text{off}}i_w$ as a function of the offset current.

By combining both equations, the following expression can be obtained:

$$\frac{F_w}{k_{B10}} = i_w + k_{cc}(i_w^2 + 2i_{\text{off}}i_w) \quad (4.22)$$

Equation (4.22) is the basis for the method used to determine k_{cc} . Since F_w is a force generated by the weight of a test mass, its value is assumed to be very stable. For small temperature deviations it is also possible to assume a constant value for the actuator constant k_{B10} . By using different values for the offset current i_{off} , the current i_w changes. There is a special case when the offset current i_{off} has a magnitude equal to the half of the current i_w magnitude and the term $i_w^2 + 2i_{\text{off}}i_w$ is equal to zero. In this case $i_{\text{off}} = i_{\text{off}0}$, $i_w = i_{w0}$ and

$$i_{w0} = -\frac{1}{i_{\text{off}0}} = \frac{F_w}{k_{B10}} \quad (4.23)$$

Figure 4.15 shows the term $i_w^2 + 2i_{\text{off}}i_w$ as a function of the offset current. This is a measurement result performed with a prototype of the transducer and this result was obtained for the coil 1 of group I. In this figure, a dashed line containing a linear fit for the points measured and another dashed line for the zero values are shown. Both lines cross at $i_{\text{off}} = -8.6515 \text{ mA}$.

With this procedure the ratio F_w/k_{B10} can be determined without measuring the force F_w or the actuator constant k_{B10} . By using (4.22) and (4.23) the following expression can be obtained:

$$k_{cc} = \frac{i_{w0} - i_w}{i_w^2 + 2i_{\text{off}}i_w} \quad (4.24)$$

Figure 4.16 shows measurement results used to determine the coil-current parameter k_{cc} for the coil 1 of group I. 66 measurements were performed for different levels of offset current. The coil-current parameter was measured equal to $7.01(65) \text{ mA}^{-1}$ for this actuator. For the coil 2 of the group I the same measurement was performed and the value obtained is $10.84(51) \text{ mA}^{-1}$. The standard deviation for the mean value of the measurements was used for the determination of the measurement uncertainty. The electrical currents were determined

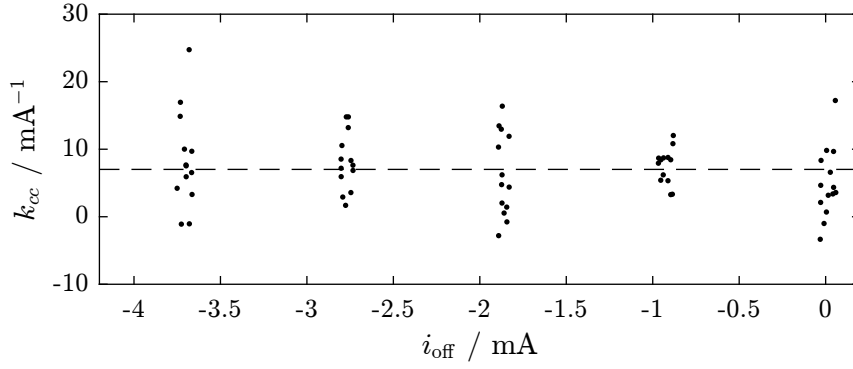


FIGURE 4.16: Measurements used to determine the coil-current parameter k_{cc} for the coil 1 of group I. The value for k_{cc} , which is the mean value of the measurements, indicated with a dashed line.

by measuring the voltage drop on the same resistors described in section 4.3 by using the digital voltmeters described in section 4.2. With these equipment the measurement uncertainties obtained are much lower than the uncertainties of k_{cc} . The uncertainty contributions of the procedure described to determine i_{w0} were neglected as well. By comparing the values for i_{w0} obtained with this procedure with values obtained by the measurement of F_w and k_{B10} , deviations smaller than 50 ppm were obtained. These deviations are three orders of magnitude smaller than the uncertainty for k_{cc} .

4.5.2 INDUCTIVE COUPLING BETWEEN COILS

During the calibration mode the sensing element of the multicomponent transducer is moved with a sine wave reference trajectory by using the actuators of the group II and the voltages induced in the coils of group I are measured simultaneously (section 3.1). The alternating currents flowing in the coils II generate induced voltages in the coils I as well. These voltages cause a measurement deviation in the determination of the actuator constant. Due to the inductive coupling between the coils the following dependency arises:

$$\hat{u}_{ind0} = u_{ind0}(1 + k_{ic}\omega_0^2), \quad (4.25)$$

where u_{ind0} is the induced voltage caused by the movement of the coil in the magnetic field and \hat{u}_{ind0} is this voltage added to the induced voltage caused by the inductive coupling, which is the measured voltage. This causes the following dependency of the actuator constant on the frequency of movement:

$$\hat{k}_{B10} = k_{B10}(1 + k_{ic}\omega_0^2) \quad (4.26)$$

Figure 4.17 shows a measurement result used to determine the inductive coupling coefficient k_{ic} for the coil 1 of group I. For this coil the coefficient was measured equal to $-0.311(10)\mu\text{rad}^{-2}$. This value was determined by fitting a function with the same format as equation (4.26) to the data shown in figure 4.17 by using the method of least squares. The uncertainty value was determined

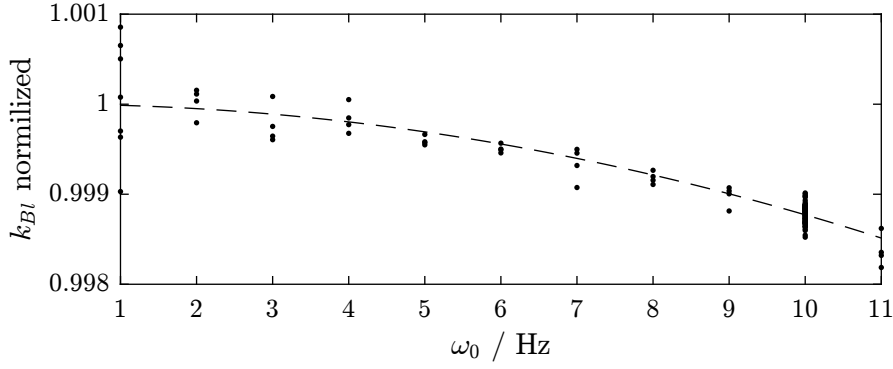


FIGURE 4.17: Measurements used to determine the effect of inductive coupling in the voice coil actuators.

by performing this fitting to different subsets of the data set and observing the variations in k_{ic} . For the coil 2 of group I this value was measured equal to $-0.290(10) \mu\text{rad}^{-2}$ by using the same method.

4.6 UNCERTAINTY BUDGED

In this section the uncertainty for the force and torque measurement with the multicomponent transducer is determined. For this determination, the mathematical model for the transducer, which is described in section 3.2, and the individual uncertainty contributions explained in this chapter are used.

As described in section 3.1, during the sensing mode the coils I of the multicomponent transducer are used to control the sensing element and compensate the external forces and torques applied to it. By using equation (3.44) it is possible to determine the measured forces and torques for the x , y and z directions:

$$F_x = k_{Bl-11}i_{11} + k_{Bl-12}i_{12} \quad (4.27)$$

$$F_y = k_{Bl-13}i_{13} + k_{Bl-14}i_{14} \quad (4.28)$$

$$F_z = k_{Bl-15}i_{15} + k_{Bl-16}i_{16} \quad (4.29)$$

$$T_x = -l_{13}k_{Bl-13}i_{13} + l_{14}k_{Bl-14}i_{14} \quad (4.30)$$

$$T_y = -l_{15}k_{Bl-15}i_{15} + l_{16}k_{Bl-16}i_{16} \quad (4.31)$$

$$T_z = l_{11}k_{Bl-11}i_{11} - l_{12}k_{Bl-12}i_{12} \quad (4.32)$$

where the actuators constants $k_{Bl-11}, \dots, k_{Bl-16}$ and the parameters l_{11}, \dots, l_{16} are given by the equations (3.66)-(3.71). The following expressions can be obtained which are used to determine the forces and torques measured with the multicomponent transducer based on the position, angle, voltage, electrical resistance and time measurements:

$$F_x = \frac{u_{110}}{x_0\omega_0} \frac{u_{R1}}{R_1} + \frac{u_{120}}{x_0\omega_0} \frac{u_{R2}}{R_2} \quad (4.33)$$

$$F_y = \frac{u_{130}}{y_0\omega_0} \frac{u_{R3}}{R_3} + \frac{u_{140}}{y_0\omega_0} \frac{u_{R4}}{R_4} \quad (4.34)$$

$$F_z = \frac{u_{150}}{z_0\omega_0} \frac{u_{R5}}{R_5} + \frac{u_{160}}{z_0\omega_0} \frac{u_{R6}}{R_6} \quad (4.35)$$

$$T_x = -\frac{u_{1310}}{\phi_0\omega_0} \frac{u_{R3}}{R_3} + \frac{u_{1410}}{\phi_0\omega_0} \frac{u_{R4}}{R_4} \quad (4.36)$$

$$T_y = -\frac{u_{1510}}{\theta_0\omega_0} \frac{u_{R5}}{R_5} + \frac{u_{1610}}{\theta_0\omega_0} \frac{u_{R6}}{R_6} \quad (4.37)$$

$$T_z = \frac{u_{1110}}{\psi_0\omega_0} \frac{u_{R1}}{R_1} - \frac{u_{1210}}{\psi_0\omega_0} \frac{u_{R2}}{R_2} \quad (4.38)$$

The coil-current effect and the inductive coupling, which are described in sections 4.5.1 and 4.5.2 respectively, also have to be considered for the determination of the measured forces and torques. For the force measurement in x direction and for the torque measurement in z direction, the following expressions can be obtained by combining (4.33) and (4.38) with (4.25) and (4.15):

$$F_x = \frac{\hat{u}_{110}}{x_{011}\omega_0} \frac{u_{R1}}{R_1} \frac{1 + k_{cc11}(u_{R1}/R_1)}{1 + k_{ic11}\omega_0^2} + \frac{\hat{u}_{120}}{x_{012}\omega_0} \frac{u_{R2}}{R_2} \frac{1 + k_{cc12}(u_{R2}/R_2)}{1 + k_{ic12}\omega_0^2} \quad (4.39)$$

$$T_z = \frac{\hat{u}_{1110}}{\psi_0\omega_0} \frac{u_{R1}}{R_1} \frac{1 + k_{cc11}(u_{R1}/R_1)}{1 + k_{ic11}\omega_0^2} - \frac{\hat{u}_{1210}}{\psi_0\omega_0} \frac{u_{R2}}{R_2} \frac{1 + k_{cc12}(u_{R2}/R_2)}{1 + k_{ic12}\omega_0^2} \quad (4.40)$$

Equations (4.39) and (4.40) represent the measurement model for the force and torque measurements respectively. These equations are used to determine the measurement uncertainty using the standard method described in the guide to the expression of uncertainty in measurement (GUM, [81]). For this uncertainty estimation, the cross-correlation between the variables is neglected as performed in [84]. Tables 4.5 and 4.6 on page 83 contain the uncertainty budgets for the force and torque measurements respectively. In each table the measurement uncertainty is determined for three conditions: the design specifications, the setup 1 and the setup 2. The system was originally designed to measure forces and torques in a range of 2 N and 0.1 N m with maximal relative expanded uncertainty ($k=2$) of 1×10^{-4} for both force and torque measurements. The uncertainty values used for the design specifications have already been published in [26]. In the measurement with the setup 1 the voltages are measured with the analog-to-digital converters of the real-time controller and the position and angle are measured with the aperture slit sensors. For the setup 2 the voltages are measured with a precision digital voltmeter and the position and angle are measured with a laser interferometer.

For the force measurement with the setup 1, a relative standard uncertainty of 0.13 % can be achieved for the range of 2.2 N. That represents a standard uncertainty of about 2.9 mN. The biggest uncertainty contribution in this case is the uncertainty for the induced voltage measurement. This high uncertainty is caused by the nonlinearities of the analog-to-digital converters shown in figure 4.9. The induced voltage is a sine-wave function with a frequency of 10 Hz and amplitude of 49 mV. For the standard uncertainty determination, the peak-to-peak amplitude of 98 mV is considered. The maximal deviation of 180 μ V caused by the nonlinearities in the voltage measurement represent a relative standard uncertainty of 0.18 %. Experimental results show that the repeatability for the induced voltage measurement with the analog-to-digital converters is smaller than

40 ppm and, for this reason, this uncertainty contribution is neglected in the induced voltage measurement. The second biggest uncertainty contribution for the force measurement with the setup 1 is caused by the voltage drop measurement. This uncertainty is also caused by the nonlinearities of the analog-to-digital converters. For the setup 2, relative and absolute standard uncertainties of 44 ppm and 97 μN are obtained for the force measurement respectively. The uncertainty contributions related to measuring resistor, movement frequency, inductive coupling and coil-current effect are the same for both setups. The measurement uncertainty is reduced by using the digital voltmeter and the laser interferometer to measure the induced voltage amplitude, the voltage drop and the translation amplitude more precisely. In this case, the biggest uncertainty contribution is the inductive coupling between the actuators and the second biggest contribution is the coil-current effect. The measurement of the translation amplitude and the induced voltage amplitude are the third and fourth biggest contributions respectively. For the torque measurement an additional difficulty is given by the angle measurement using the laser interferometer. As described in section 4.1, the range of motion is limited to 124 μrad and a relative standard uncertainty of 453 ppm is obtained for the angle measurement with the laser interferometer. Although the angle measurement with the aperture slit position sensors exhibits a much better repeatability, the measurement uncertainty is limited by the uncertainty obtained with the laser interferometer, which is used to calibrate the aperture slit sensors. For this reason, the standard uncertainty for the rotation amplitude is the same for both setups. The limitation in the amplitude of movement causes a reduction in the induced voltage amplitude during the calibration mode. For the torque measurement with the setup 1 a relative standard uncertainty of 0.75 % is obtained for a torque of about 0.11 N m, which represents a standard uncertainty of 0.82 mN m. The biggest uncertainty contribution in this case is the measurement of the induced voltage amplitude. The measurement uncertainty for the induced voltage amplitude in the torque measurement is obtained by assuming that the absolute standard uncertainty for this quantity remains constant and is the same for both force and torque measurements. For the torque measurement with the setup 2 a relative and absolute standard uncertainties of 460 ppm and 51 $\mu\text{N m}$ are obtained respectively. The biggest uncertainty contribution in this case is the angle measurement with the laser interferometer. The second biggest contribution is caused by the induced voltage amplitude. This uncertainty is also obtained by assuming that the absolute standard uncertainty for this quantity is the same for both force and torque measurements.

For the force measurement, the measurement uncertainty obtained is smaller than all systems listed in table 2.1. However, several changes can be performed in the system with the objective to improve the uncertainty for both force and torque measurements. That includes the elimination of the inductive coupling in the system by means of a design changes, the minimization of the coil-current effect by measuring the coil-current coefficient with a better uncertainty, the improvement of the range of motion of the system to reduce the relative uncertainty of both translation amplitude and induced voltage amplitude and the improvement of the induced voltage amplitude by raising the actuator constant. In order

TABLE 4.5: Uncertainty budget for the force measurement.

Description	Variable	Design specification			Setup 1			Setup 2		
		Value	σ_{rel}	Cont.	Value	σ_{rel}	Cont.	Value	σ_{rel}	Cont.
Induced voltage amp.	$\hat{u}_{I10}, \hat{u}_{I20}$	37 mV	27 ppm	7.5 %	49 mV	0.18 %	96.0 %	49 mV	24 ppm	15.2 %
Voltage drop	u_{R1}, u_{R2}	0.5 V	40 ppm	16.5 %	0.5 V	360 ppm	4.0 %	0.5 V	10 ppm	4.2 %
Translation amplitude	x_{0I1}, x_{0I2}	30 μm	34 ppm	45.8 %	36 μm	34 ppm	0.0 %	36 μm	25 ppm	16.6 %
Measuring resistor	R_1, R_2	10 Ω	10 ppm	1.0 %	10 Ω	1.9 ppm	0.0 %	10 Ω	1.9 ppm	0.0 %
Movement frequency	ω_0	10 Hz	10 ppm	4.1 %	10 Hz	60 ppb	0.0 %	10 Hz	60 ppb	0.0 %
Inductive coupling	k_{icI1}, k_{icI2}	-	-	-	$-0.3 \mu\text{rad}^{-2}$	3.2 %	0.0 %	$-0.3 \mu\text{rad}^{-2}$	3.2 %	41.4 %
Coil-current coefficient	k_{ccI1}, k_{ccI2}	-	-	-	7 mA^{-1}	9.3 %	0.0 %	7 mA^{-1}	9.3 %	22.6 %
Force measurement	F_x	2 N	50 ppm		2.2 N	0.13 %		2.2 N	44 ppm	

TABLE 4.6: Uncertainty budget for the torque measurement.

Description	Variable	Design specification			Setup 1			Setup 2		
		Value	σ_{rel}	Cont.	Value	σ_{rel}	Cont.	Value	σ_{rel}	Cont.
Induced voltage amp.	$\hat{u}_{I1I0}, \hat{u}_{I2I0}$	37 mV	27 ppm	7.5 %	8.4 mV	1.05 %	99.6 %	8.4 mV	140 ppm	4.6 %
Voltage drop	u_{R1}, u_{R2}	0.5 V	40 ppm	16.5 %	0.5 V	360 ppm	0.0 %	0.5 V	10 ppm	0.0 %
Rotation amplitude	ψ_0	580 μrad	34 ppm	45.8 %	124 μrad	453 ppm	0.4 %	124 μrad	453 ppm	94.8 %
Measuring resistor	R_1, R_2	10 Ω	10 ppm	1.0 %	10 Ω	1.9 ppm	0.0 %	10 Ω	1.9 ppm	0.0 %
Movement frequency	ω_0	10 Hz	10 ppm	4.1 %	10 Hz	60 ppb	0.0 %	10 Hz	60 ppb	0.0 %
Inductive coupling	k_{icI1}, k_{icI2}	-	-	-	$-0.3 \mu\text{rad}^{-2}$	3.2 %	0.0 %	$-0.3 \mu\text{rad}^{-2}$	3.2 %	0.4 %
Coil-current coefficient	k_{ccI1}, k_{ccI2}	-	-	-	7 mA^{-1}	9.3 %	0.0 %	7 mA^{-1}	9.3 %	0.2 %
Torque measurement	T_z	0.1 N m	50 ppm		0.11 N m	0.75 %		0.11 N m	460 ppm	

to improve the uncertainty for the torque measurement, the changes listed in section 3.2.4 can be performed, including the use retroreflectors instead of a plane mirror, in a way to increase the range of motion and reduce the relative measurement repeatability, and the use of a two-beam laser interferometer to eliminate uncertainty contributions from the linear stage.

CHAPTER 5

VERIFICATION OF THE RESULTS

With the objective to verify the integrated calibration used in the multicomponent transducer, the force measurement based on this procedure is compared with the force measurement based on traditional calibration procedures, which use dead-weights. A description of the measuring setup is provided here and measurement results are shown.

5.1 DESCRIPTION OF THE MEASURING SETUP

A sketch of the measuring setup used to perform the verifications is shown in figure 5.1. A picture of the same setup is shown in figure 5.2. It is composed by the multicomponent transducer with integrated calibration, a load changer with a test mass, a laser interferometer and a two-axis linear stage. The test mass is an aluminum ring with 35 g and has three positions which can be used to place additional masses. For the measurements performed here, three stainless steel spheres with about 14 g each were used. The laser interferometer was used for the traceable position measurement. The two-axis linear stage was used to adjust the position of the sensor relative to the laser beam in order to perform the traceable position and angle measurement as described in section 4.1. This measuring setup is in air inside a climate chamber with controlled temperature. The test masses were determined by doing comparison measurements with a calibrated 50 g E1 reference weight. For these measurements, an analytical balance (appendix A, SMAB) with resolution of 0.01 mg and maximal linearity deviation of 0.1 mg was used and air buoyancy corrections were performed. Table 5.1 contains the uncertainty budget for the determination of the mass of the aluminum ring. The relative standard uncertainty of the force generated by this mass is about 2.4 ppm. For the stainless steel spheres uncertainties with the same magnitude were obtained. The local gravity acceleration was measured by the Federal Agency for Cartography and Geodesy of Germany (BKG) equal to $9.810\,140\,3(18)\,\text{ms}^{-2}$. For the adjustment of the laser verticality an alcohol pool was used as reflector as described in [27]. The intensity of the laser beam was used as indicator for the verticality during the adjustment. With this method, the angle of the laser can be adjusted relative to the gravity acceleration direction with a maximal deviation of $1.5'$. The E1 reference weight used to perform the measurements has a relative standard uncertainty of 0.35 ppm. The measurement of air pressure, temperature and humidity are necessary during the calibration of the test weight and also during the verification measurements. These uncertainties are listed in table 5.1 as well. Since the measurement of these quantities is performed by using

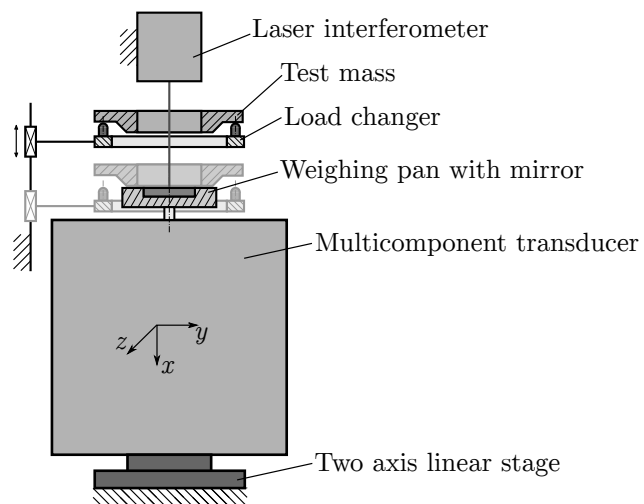


FIGURE 5.1: Sketch of verification setup with the test mass, load changer and laser interferometer.



FIGURE 5.2: Picture of the verification setup. Contact between test weight and load changer defined by V-groove and sphere.

TABLE 5.1: Uncertainty for the weight force generated by the test mass.

Description	Standard uncertainty*	Uncertainty contribution
Gravity acceleration	0.18 ppm	0.5 %
Laser verticality	$\leq 1.5'$	0.2 %
Balance readout for 35 g test mass**	1.64 ppm	45.5 %
Balance readout for 50 g E1 weight**	1.15 ppm	22.4 %
Mass of 50 g E1 weight	0.35 ppm	2.0 %
Air pressure during 35 g test mass calibration	0.09 %	1.0 %
Relative humidity during 35 g test mass calibration	6.3 %	0.2 %
Temperature during 35 g test mass calibration	2.2 %	6.0 %
Air pressure during measurements	0.12 %	4.4 %
Relative humidity during measurements	19.0 %	0.8 %
Temperature during measurements	1.4 %	3.4 %
Density of 50 g E1 weight at 20 °C	0.58 %	10.8 %
Aluminum density at 20 °C	4.30 %	2.8 %
Force generated by test mass	2.4 ppm	

*All standard uncertainties are relative, except for the laser verticality

**The balance readout contributions are determined by linearity deviations

different instruments at different conditions, the uncertainties obtained are not equal. Additionally, the determination of the density for both aluminum weight and the stainless steel E1 weight are necessary. These quantities are determined with uncertainties of 4.3 % and 0.58 % respectively. The uncertainty of the aluminum weight is relatively high because the exact composition of the alloy used is unknown and an estimation was used. The uncertainty for the E1 weight was extracted from the OIML R 111-1 international recommendation [40].

The biggest contributions for the measurement uncertainty of the force generated by the test mass are given by the balance readout deviations. For the test mass and the E1 weight these contributions are 45.5 % and 22.4 % respectively. The third and forth biggest contributions are given by the density of the E1 weight and the temperature measurement during the test mass calibration, which are 10.8 % and 6.0 % respectively. The remaining contributions represent 15.3 % of the total uncertainty budget.

5.2 EXPERIMENTAL RESULTS

Figure 5.3 shows measurement results obtained with the experimental setup of figure 5.1. For each measurement, a calibration routine was performed and the weight of the test mass was measured by using the load changer. During the calibration mode, the position of the sensing element and the induced voltages were measured with the laser interferometer and the digital voltmeter, as performed in setup 2 of table 4.5. The measurements were repeated 634 times, and the results obtained have a standard deviation of 40 ppm and a mean value of

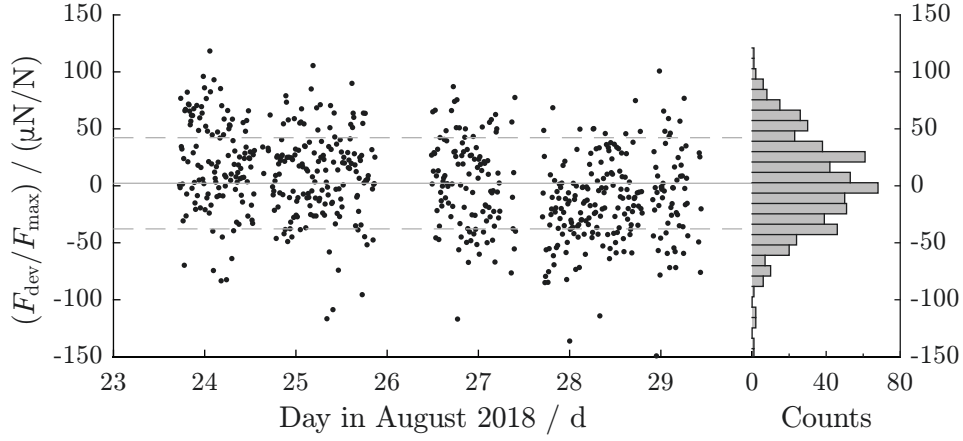


FIGURE 5.3: Relative deviation for the force measurement with the multicomponent transducer using the integrated calibration. The weight force of the test mass F_{\max} is approximately 756 mN. The measurements were repeated 634 times and the mean value and standard deviation obtained are 2.2 ppm and 40 ppm respectively.

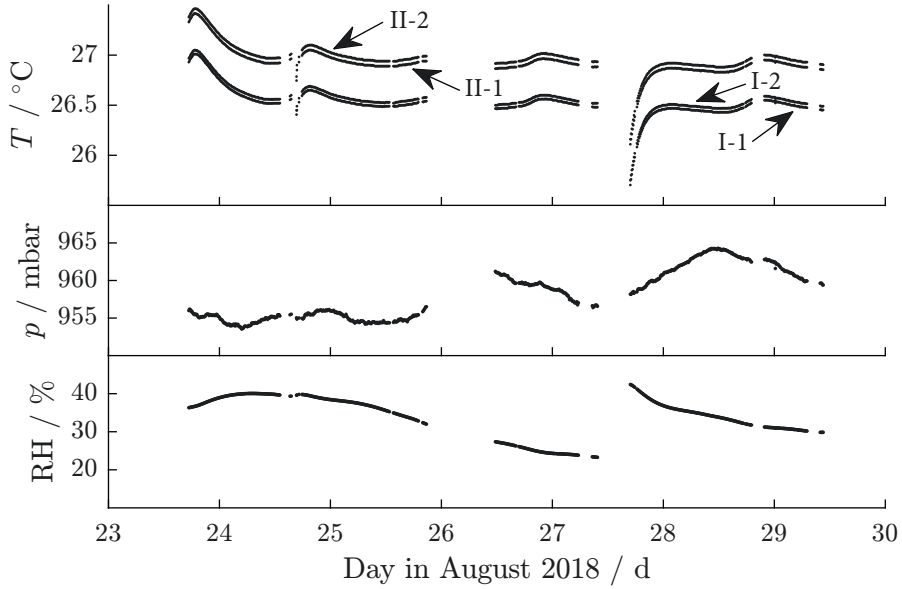


FIGURE 5.4: Temperature, air humidity and pressure variation during measurement for verification of the multicomponent transducer with a test mass. The temperature for the four magnet systems of the actuators responsible for generating forces in the x direction is shown. The reference to the actuators are the same as used in table 3.1 on page 35.

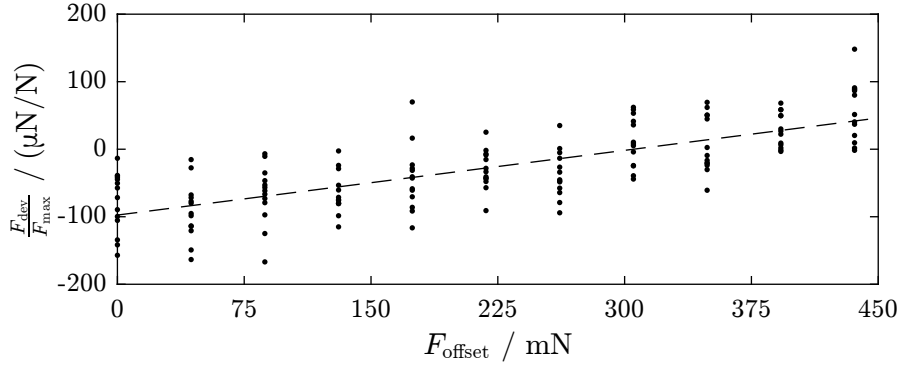


FIGURE 5.5: Deviations caused by the coil-current effect in the force measurement. The weight force of the test mass F_{\max} is approximately 756 mN.

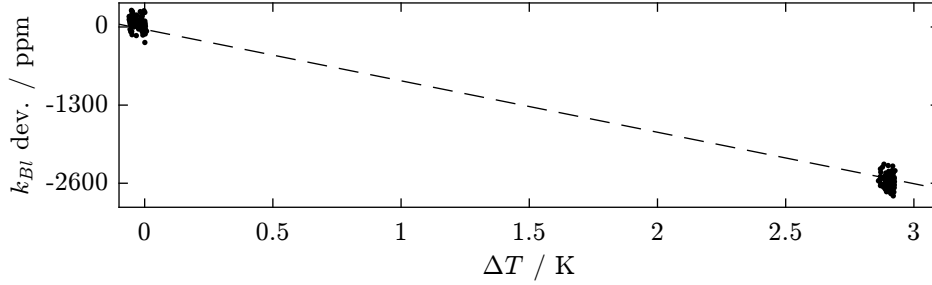


FIGURE 5.6: Relative variation of the actuator constant k_{BI} as a function of the temperature. The temperature variation is relative to 22.1 °C.

2.2 ppm. For the total test mass of 77 g that represents 30 μN and 1.7 μN respectively. Relative to a force of 2 N, the standard deviation obtained is equal to 15 ppm and the mean-value deviation is 0.8 ppm. The temperature of the magnet systems of the actuators, the air humidity and the pressure were measured with the integrated sensors, which are described in section 3.1.2. Figure 5.4 shows the measurement results obtained with these sensors. The temperature for the four magnet systems of the actuators responsible for generating forces in the x direction are shown. These are the actuators 1 and 2 of the coils I and II. Since the coils of group II are responsible for compensating the weight force of the sensing element, the electrical currents flowing in these coils are higher. That causes a higher power dissipation and, for this reason, the temperature of these actuators is about 0.5 °C higher. Temperature deviations higher than 1 °C were observed during the measurements. The air pressure and relative humidity also changed in a range of about ± 5 mbar and ± 10 % during the measurements.

Figure 5.5 shows the coil current effect for the case when no compensation is used. For these measurements, the same procedure for obtaining the results of figure 5.3 was performed, but different offset forces were generated with the coils II. For an offset force of 378 mN, the deviation in the force measurement is near to zero. This force is the half of the weight force generated by the test mass and, for this reason, it is near to zero. This behavior is known for traditional

Kibble balance experiments [53]. Measurement deviations up to 100 ppm can be caused due to the coil-current effect.

The temperature dependency of the actuator constant, which is described in section 3.2.2, was evaluated by using the same experimental setup. Figure 5.6 shows the results obtained. In these measurements, the actuator constant of the coil 1 of group I was measured by using the calibration mode of the multicomponent transducer. Measurements were performed inside a climate chamber at temperatures of 22.1 °C and 25 °C. A temperature dependency of about -900 ppm/K was obtained and this value is similar to the results expected.

CHAPTER 6

APPLICATIONS OF THE SYSTEM

In this chapter, examples for the application of multicomponent transducers are provided, including the dynamic and static identification of other multicomponent force and torque transducers, the determination of flow velocities in liquid metals by using the Lorentz force velocimetry and the force and torque measurement in micromachining.

6.1 IDENTIFICATION OF FORCE AND TORQUE TRANSDUCERS¹

The characterization of the behavior of force and torque transducers is a requirement for the precise measurement of forces and torques. As described in chapter 2, there are several measuring principles for these quantities available, with corresponding implementations and prototypes. Two examples are the measurement of deformations in compliant mechanisms with strain gauges and the electromagnetic force compensation (EMFC). The performance of these systems has been extensively evaluated regarding aspects such as the linearity and dynamic response. There are well-known methods for consistently analyzing one-component force measurement systems [11, 86, 87], however, when considering multicomponent force and torque transducers, more attention should be taken [72]. With the additional measuring components, new requirements for adjusting the position and orientation of the transducer are introduced. Furthermore, the coupling between the different measuring components must be considered and, for the torque components, the center of the measuring axes, which can differ from the geometrical center of the transducer due to manufacturing tolerances, must be identified. The identification of multicomponent force transducers has been addressed in the literature and several technics have been presented. For instance, as described in section 2.2.2, the use of deadweights and automated load changers are principles applied to one component transducers that were successfully adapted to multicomponent force measuring systems [13, 72, 88, 89]. Other identification technics, such as the shape from motion method, are dedicated to multicomponent transducers [90, 91]. In this section, an experimental setup for identifying multicomponent transducers is described and used for characterizing the dynamic and static behavior of a test transducer. The main component of this setup is the multicomponent transducer based on the electromagnetic force compensation presented in [12]. The system adopted for the tests is a force and

¹Part of the content of this section has been published by the author in [85].

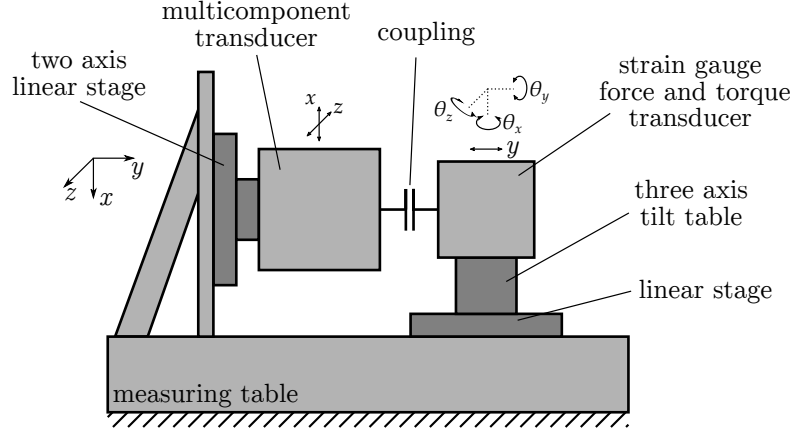


FIGURE 6.1: Experimental setup used for the identification of multicomponent force and torque transducers.

torque transducer based on strain gauges, which is capable of measuring forces and torques in three orthogonal directions simultaneously [88]. A further objective of this setup is to verify numerical simulations used for describing the dynamic and static behavior of the test transducer.

6.1.1 EXPERIMENTAL SETUP

The experimental setup used for the identification tasks is presented in figure 6.1. The multicomponent transducer, which is described in [12], is the main component of the experimental setup. This multicomponent transducer is similar to the system described in chapter 3, but it does not include the calibration system and was designed for measuring forces and torques in a higher range. This transducer can be used to generate force and torque vectors with arbitrary magnitude, direction and time behavior. The line of action of the forces generated can be changed as well and, in this way, the forces can be applied directly to the center of the transducer under test without generating a torque in the coordinate system of this transducer. The transducer to be tested is coupled to the multicomponent transducer by a rigid coupling. The relative position and angle between the systems can be adjusted in six degrees of freedom with a single-axis linear stage (LS1A, appendix A), a two-axis linear stage and a three-axis tilt table. These adjustment directions are shown in figure 6.1. While this system was used only with one type of test transducer, it can be adapted to any multicomponent force and torque transducer that has a similar measuring range.

The sensing element of the multicomponent transducer is shown in figure 6.2. The voice coil actuators are used to generate the dynamic and static forces for the identification process. These actuators are also responsible for generating an offset force to compensate the weight of the sensing element. As an example, a pair of forces F_1 and F_2 is shown in figure 6.2. With these forces it is possible to generate a force in the x direction with the magnitude

$$F_x = F_1 - F_2, \quad (6.1)$$

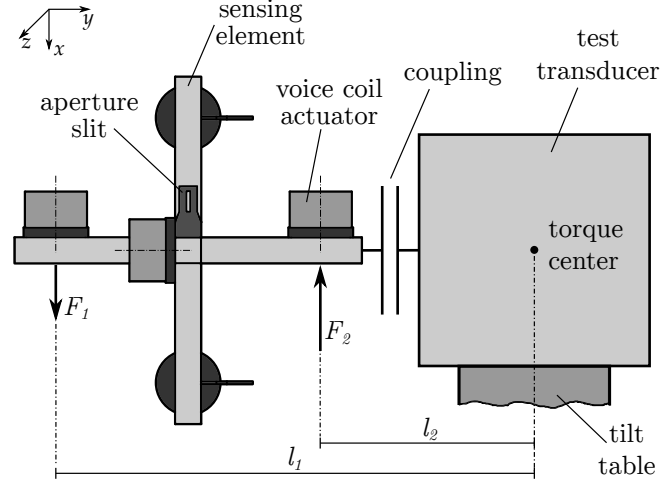


FIGURE 6.2: Sensing element and test transducer.

and a torque in the z direction with the magnitude

$$T_z = F_1 l_1 - F_2 l_2. \quad (6.2)$$

The torque component is calculated for the torque center of the test transducer. In case the parameters l_1 and l_2 are unknown, they can be identified by generating linearly independent combinations of F_1 and F_2 and measuring the output torque T_z of the test transducer. In this way, the following linear system of equations is obtained:

$$\begin{bmatrix} T_z^1 \\ T_z^2 \\ \vdots \\ T_z^n \end{bmatrix} = \begin{bmatrix} F_1^1 & -F_2^1 \\ F_1^2 & -F_2^2 \\ \vdots & \vdots \\ F_1^n & -F_2^n \end{bmatrix} \begin{bmatrix} l_1 \\ l_2 \end{bmatrix} \quad (6.3)$$

where n represents the amount of measurements and combinations for the forces F_1 and F_2 . This overdetermined system of equations can be solved by using the ordinary least squares method. The solution is given by the following expression:

$$\mathbf{l} = (\mathbf{F}^T \mathbf{F})^{-1} \mathbf{F}^T \mathbf{T} \quad (6.4)$$

In this equation $\mathbf{l} \in \mathbb{R}^2$ represents the vector containing the parameters l_1 and l_2 , $\mathbf{F} \in \mathbb{R}^{n \times 2}$ is the matrix with the combinations of forces and $\mathbf{T} \in \mathbb{R}^n$ is the vector with the measured torques.

With this system it is possible to generate arbitrary test signals, such as the chirp signal, the maximum length binary sequence (MBLS) [92] and signal patterns given by calibration guidelines for force transducers, like the DAkkS-DKD-R 3-3, published by the national accreditation body for the Federal Republic of Germany [15]. The forces and torques are generated and measured simultaneously by using a real-time controller equipped with eighteen analog-to-digital converter (ADC) input channels and six digital-to-analog converter (DAC) output channels. Six ADC channels are used for measuring the electrical output signals of the test

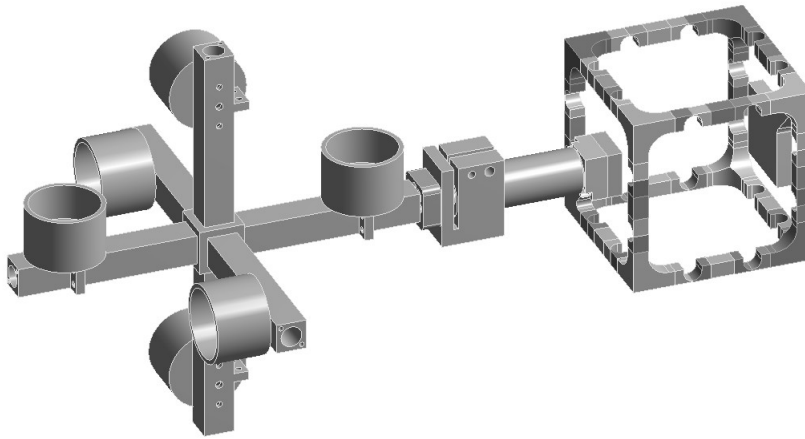


FIGURE 6.3: Model used for the finite element simulations of the multicomponent transducer.

transducer which are proportional to the applied forces and torques, six ADC channels are used for measuring the electrical signals related to the position and angles of the sensing element and six ADC channels are used for measuring the current flowing in the voice coil actuators with the help of measurement resistors. These current signals are used to determine the forces and torques generated by the multicomponent transducer. The reference signals for the forces and torques are generated by the six DAC channels. Since the six output signals from the test transducer are measured simultaneously, it is possible to identify interferences and cross-talk between the components. The force and torque vectors generated by the multicomponent transducer are resulted from the sum of the forces and torques generated by the six voice coil actuators, in a way to freely change the direction of the forces and torques actuating in the test transducer. An additional feature of the presented system is the possibility to measure the linear and rotational stiffness of the test transducer by using the position and angle signals provided by the six aperture slit position sensors together with applied forces and torques.

6.1.2 SIMULATION MODEL

Force and torque transducers are used in several branches of science, industry and commerce. Depending on the specific application, additional elements have to be attached to the transducer to perform the measurement task. For example, in the Lorentz force velocimetry, which is described in section 6.2, permanent magnets have to be mounted in the sensing element in order to measure the interaction forces between a liquid metal flow and the static magnetic field generated by the permanent magnet. Depending on the mass of the element attached, the eigenfrequency of the system can suffer a significant change and, when measuring dynamic forces, it is fundamental to track these changes to determine the frequency response of the transducer. In order to easily predict these changes, a simulation model of the transducer can be used. The experimental setup presented here can be applied not only for the identification of force and torque transducers, but also for validating numerical models that describe these systems. With a consistent

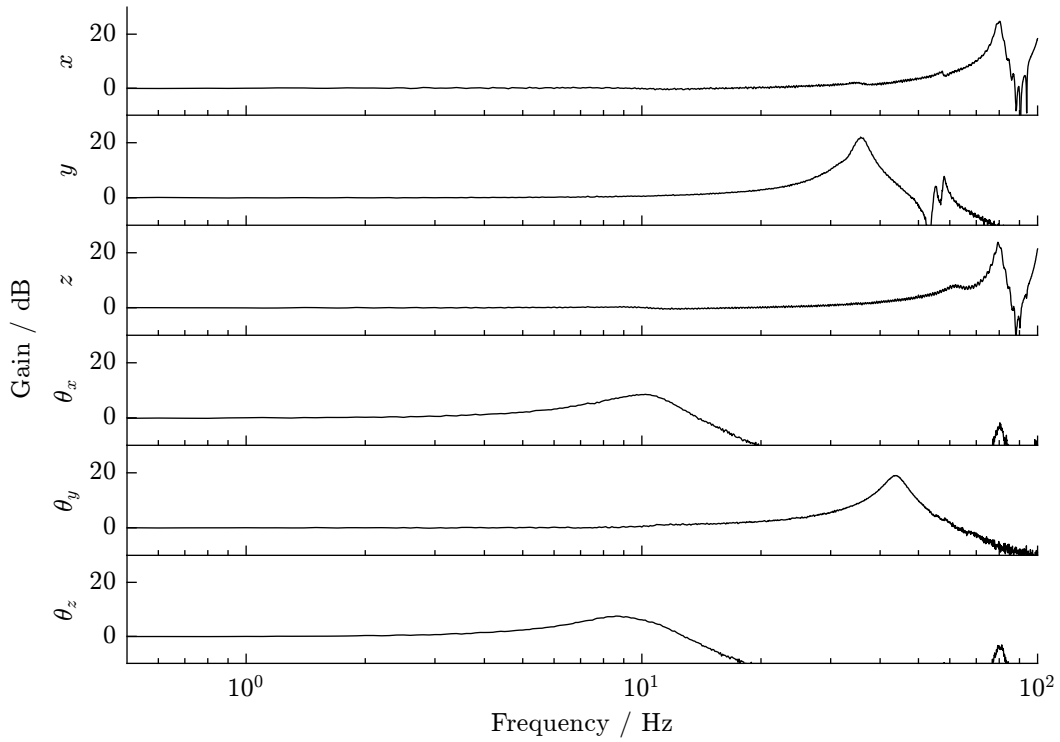


FIGURE 6.4: Frequency response of the test transducer for the six degrees of freedom.

numerical model it is possible to identify how design changes and measurement conditions influence the static and dynamic behavior of the transducer. This is important not only for the application of force and torque transducers, but also for the design of new systems.

By using a finite element analysis software, a model for the current experimental setup considering both multicomponent and test transducers was implemented (figure 6.3). This model was used to perform a harmonic analysis and identify the frequency response of the test transducer with the multicomponent transducer coupled to it, while generating dynamic forces and torques. The model of the test transducer could be verified by comparing results from both simulations and measurements.

6.1.3 RESULTS FOR A STRAIN GAUGE TRANSDUCER

The measurement setup presented here was used to identify the frequency response of the multicomponent test transducer based on strain gauges. Figure 6.4 shows the measured frequency response for the linear and angular directions, representing the transducer's dynamic response for the force and torque measurement respectively. Some characteristics of the system, such as eigenfrequency and damping, can be evaluated through this figure. These measurements were performed with chirp test signals for the forces and torques, and the frequency responses shown here were determined by using the output force/torque signals of the test transducer and the forces and torques generated by the multicomponent transducer. Additionally, the linearity of the static behavior of the test

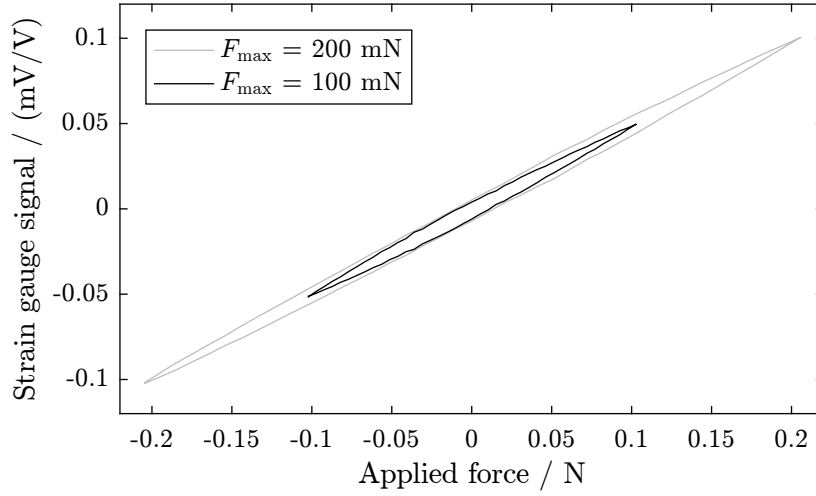


FIGURE 6.5: Hysteresis measured in the strain gauge force transducer. Representation of the hysteresis effect on the x -axis exaggerated by factor 20.

transducer was investigated. Figure 6.5 contains the measurement results of the transducer's hysteresis for the x direction. In order to perform this measurement, static force levels were applied to the transducer in a way to generate cycles of loading and unloading. Two measurements with maximal forces of 100 mN and 200 mN were performed. For these measurements, the hysteresis was responsible for an maximal relative error of about 0.3%. For the axis y and z , a similar hysteresis effect was observed in the test transducer. The stiffness of this transducer could also be measured for the y axis and a value of 12.8 kN m^{-1} was obtained. Simulations were performed with the objective to determine the stiffness for the same direction and a value of 11.1 kN m^{-1} was obtained.

Since the direction of the forces and torques generated by the EMFC transducer can be freely changed, it is possible to execute an identification procedure similar to the shape-from-motion [90, 91]. The main difference between the original method and the procedure executed in this work is that, instead of rotating the transducer to change the direction of the acting force, which is the gravitational force, the test transducer is maintained in a static position and the identification force is generated in different directions. In this way the moving mechanism for rotating the test transducer is not required. Figure 6.6 shows a measurement result for this identification method, where forces with magnitude of about 0.16 N were generated in different directions. In this figure three circles over the planes yz , xz and xy are shown, that were produced by rotating the identification force around the axis x , y and z respectively. These circles indicate if the test transducer exhibits any sort of deviation when combined forces from different components are generated.

The results obtained with the simulation model could be verified by comparing them with the measurements. Table 6.1 contains the eigenfrequencies of the test transducer obtained from both measurements and simulations. The magnitude of the error between the results is also shown in this table and a maximal error of 1.9 Hz was observed. The results shown here are for the first mode of vibration.

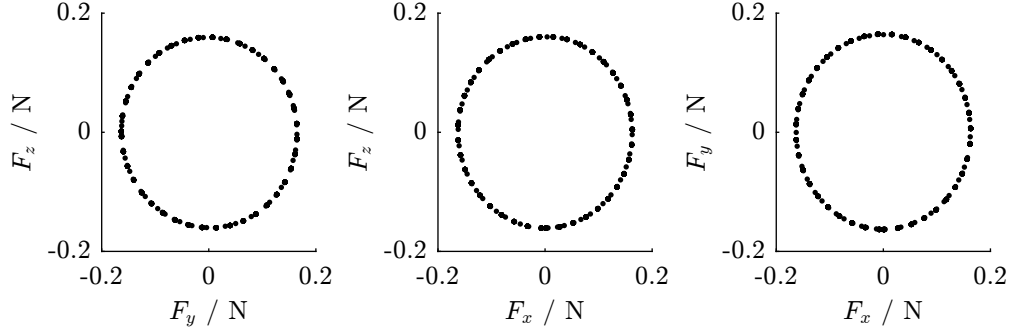


FIGURE 6.6: Results for the shape from motion measurement with the multicomponent transducer.

TABLE 6.1: Eigenfrequencies determined with the multicomponent transducers by means of measurements and simulations.

Direction	Measurement	Simulation	Deviation Magnitude
x	79.8 Hz	79.5 Hz	0.3 Hz
y	35.9 Hz	37.8 Hz	1.9 Hz
z	79.9 Hz	79.5 Hz	0.4 Hz
θ_x	10.2 Hz	10.0 Hz	0.2 Hz
θ_y	43.8 Hz	45.1 Hz	1.3 Hz
θ_z	8.7 Hz	10.1 Hz	1.4 Hz

6.2 LORENTZ FORCE VELOCIMETRY²

The Lorentz force velocimetry is a contactless technique for the measurement of flow velocities in liquid metal flows [93]. In this technique, the interaction forces between a liquid metal flowing and a permanent magnet are measured and this information is used to determine the velocity of the flow and the flow rate. Figure 6.7 shows an example of a Lorentz force flowmeter. It is basically composed by a force transducer with a permanent magnet attached to it. For a liquid metal with conductivity σ and a magnet with dipole moment m , the following relationship between the force magnitude F caused in the permanent magnet and the flow velocity magnitude v can be obtained [5]:

$$F \sim \mu_0^2 \sigma v m^2 L^{-3} \quad (6.5)$$

where L is the distance between the center of the magnet and the liquid metal. For the derivation of this relationship it was originally assumed that the fluid occupies a semi-infinite region in space.

Multicomponent force and torque transducers can be used in the Lorentz force velocimetry as described in [94]. In this way, both direction and magnitude of the flow velocity can be obtained. An important aspect for the multicomponent measurement in the Lorentz force velocimetry is the determination of the application point for the forces in the permanent magnet. This information is fundamental

²Part of the content of this section has been published by the author in [6].

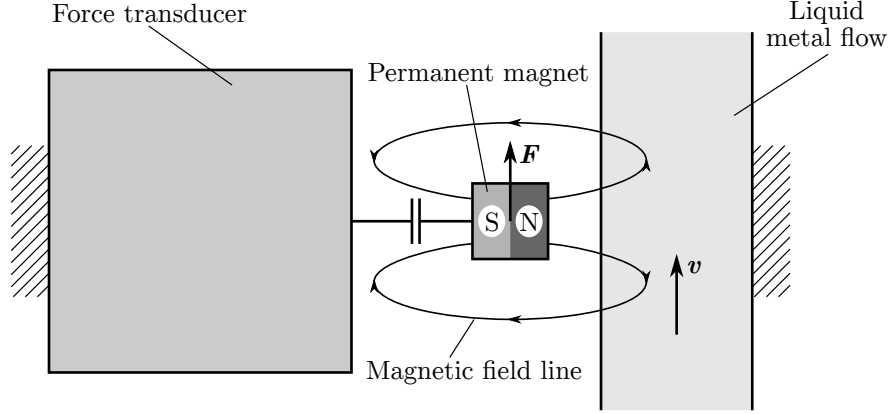


FIGURE 6.7: Principle of the Lorentz force velocimetry with a multicomponent transducer.

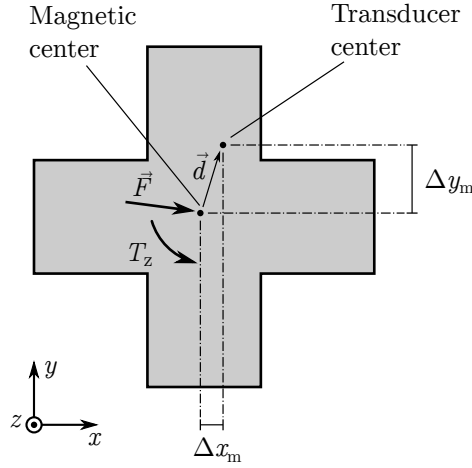


FIGURE 6.8: Magnetic center and transducer center for the cross-shaped magnet.

for the interpretation of the information obtained with the torque measurement. The application point for the forces is defined here as the magnetic center of the permanent magnet.

While the forces and torques measured by the multicomponent transducer are relative to a reference frame fixed to the transducer center, the forces actuating in the permanent magnet are generated in the magnetic center (figure 6.8). In order to determine the torque actuating in this magnetic center, the following calculation can be performed:

$$T_z = T_s - (\vec{F} \times \vec{d}) \cdot \vec{e}_z \quad (6.6)$$

where T_z is the z -component of the torque generated by the interaction between the magnetic field and the liquid metal flow, T_s is the z -component of the torque measured by the multicomponent transducer, $\vec{F} \in \mathbb{R}^3$ is the Lorentz force and $\vec{d} = (\Delta x_m, \Delta y_m, 0)$ is a vector with the distance between the magnetic center and transducer center. For determining this distance, an experimental setup composed basically by the force measuring system, the permanent magnet and

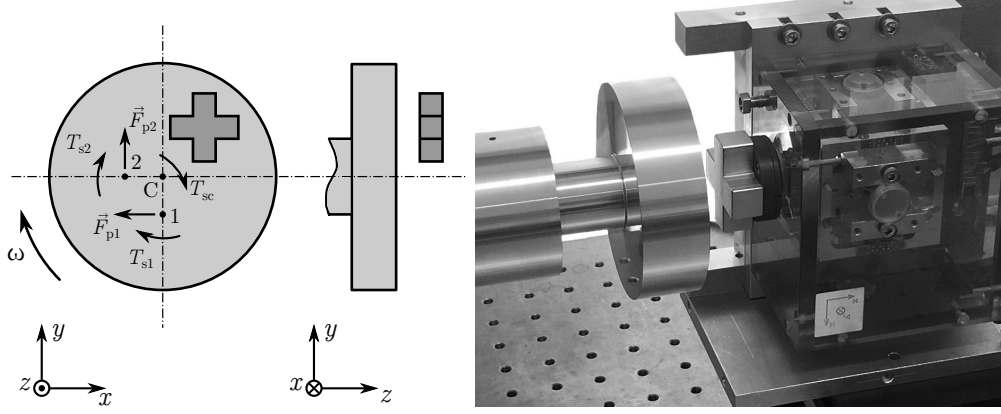


FIGURE 6.9: Experimental setup used for the calibration of the magnetic system and points adopted for the calibration procedure. In this setup the magnet system is coupled to the force transducer, as shown in the picture on the right hand side. The disc has a diameter of 100 mm and the external dimensions of the cross-shaped magnet are 45 mm \times 45 mm \times 15 mm.

a rotating disc is used (figure 6.9). With this setup it is possible to generate a Lorentz force vector \vec{F} with known direction and determine the position coordinates of the magnetic center relative to the transducer center. This is done by changing the position of the magnet relative to the rotating disc as shown in figure 6.9. For the points 1 and 2 shown in this figure, the following relationship can be obtained:

$$T_{z1} = T_{s1} + F_{p1}\Delta y_m \quad (6.7)$$

$$T_{z2} = T_{s2} + F_{p2}\Delta x_m \quad (6.8)$$

where F_{p1} and F_{p2} represent the magnitude of the force vectors \vec{F}_{p1} and \vec{F}_{p2} respectively. For the center of the rotating disc, the following relationship can be obtained:

$$T_{zc} = T_{sc} \quad (6.9)$$

As shown in [95], the z -component of the torque is constant for a region near to the disc's center. Assuming that the points 1 and 2 are inside this region, the torques T_{zc} , T_{z1} and T_{z2} are equal and the unknown parameters Δx_m and Δy_m can be determined with the equations (6.8) and (6.7) respectively:

$$\Delta x_m = \frac{T_{zc} - T_{s2}}{F_2} \quad (6.10)$$

$$\Delta y_m = \frac{T_{zc} - T_{s1}}{F_1} \quad (6.11)$$

where T_{zc} , T_{s1} , T_{s2} , F_1 and F_2 are measured quantities. Figure 6.10 shows the measured Lorentz force vector in the $x-y$ plane. This measurement was executed by scanning an area of 8 mm by 8 mm over the disc's surface. By analyzing this figure the center of the disc can be determined and the points for executing

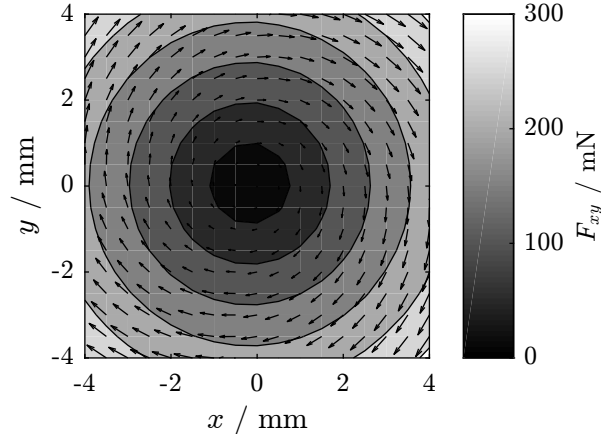


FIGURE 6.10: Measured Lorentz force with the rotating disc and a cross-shaped magnet.

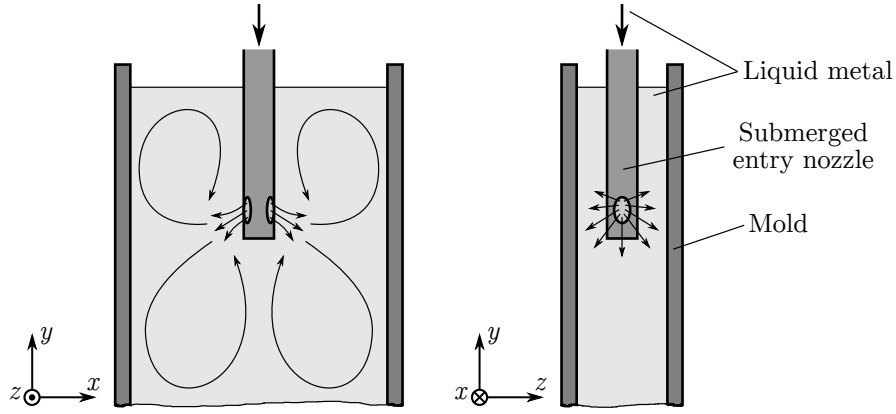


FIGURE 6.11: Mold of the continuous casting model used to perform the tests. Liquid metal flows inside the mold through the submerged entry nozzle.

the calibration can be defined. Finally, the parameters $\Delta x_m = 0.467 \text{ mm}$ and $\Delta y_m = 6.408 \text{ mm}$ were determined and the position of the center of the cross shaped magnet with respect to the transducer center could be identified.

The cross-shaped permanent magnet identified was used to perform a measurement task in a continuous casting model. This model is the mini-LIMMCAST facility at the Helmholtz Zentrum Dresden Rossendorf (HZDR). The mini-LIMMCAST has an acrylic glass mold with 210 mm height, 140 mm length and 55 mm depth, which is shown in figure 6.11. The walls of the mold have a thickness of about 7.4 mm. For these measurements, the area of the mold was discretized in a regular grid. By using a two-axis linear stage the position of the transducer and magnet can be changed and the measurements can be performed for each point. Measurement results obtained by scanning an area of $145 \text{ mm} \times 160 \text{ mm}$ are shown in figure 6.12. For these measurements, a grid spacing of 5 mm was used, resulting in a total of 990 points. The air gap between the magnet and the mold was approximately 1 mm.

In figure 6.12 two measurement results are presented: in the left hand side the

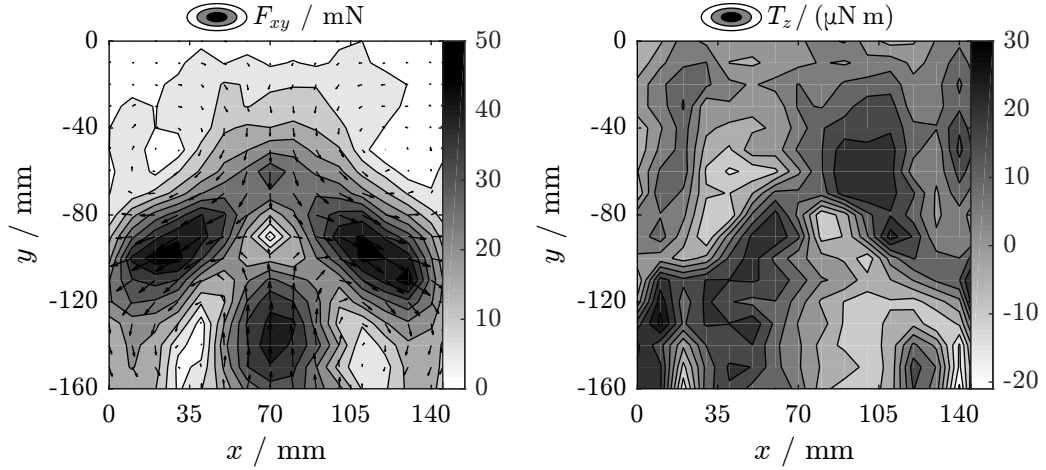


FIGURE 6.12: Forces and torque measured due to interaction of permanent magnet with liquid metal flow.

tangential force magnitude F_{xy} and direction is shown and in the right hand side the magnitude of the torque in normal direction T_z is shown. The force information can be used to determine the velocity and direction of the flow. The flow velocity is higher near to the output of the submerged entry nozzle. The measurement results are similar to the expected flow structure shown in figure 6.11. A similar study was performed in [94], where results obtained with the Lorentz force velocimetry were compared with results obtained with ultrasonic doppler velocimetry (UDV). The measurement results obtained with both experiments exhibited a good correlation. In [6] comparisons between results obtained with Lorentz force velocimetry and computational fluid dynamics also show a good correlation. As described in the same publication, the torque information in normal direction can be used to determine the vorticity of the velocity field.

6.3 MICROMACHINING³

Micromachining methods are of great importance for the fabrication of microelectromechanical systems [96, 97] and mechanical components with high accurate micron-scale structures [98]. There are several known methods for micromachining, such as micro-milling, laser processing, electrochemical etching and micro-scratching. For some of these technics, it is an advantage to determine the forces involved in the fabrication process and how they affect the results obtained [99–101]. These information are not only important for a better understanding of the machining method itself, but also for eventually improving it.

Micro scratching experiments were performed by using the multicomponent transducer. With this system the scratching process and the force measurement were performed simultaneously. To accomplish this task, a force control system

³Part of the content of this section has been published by the author in [7].

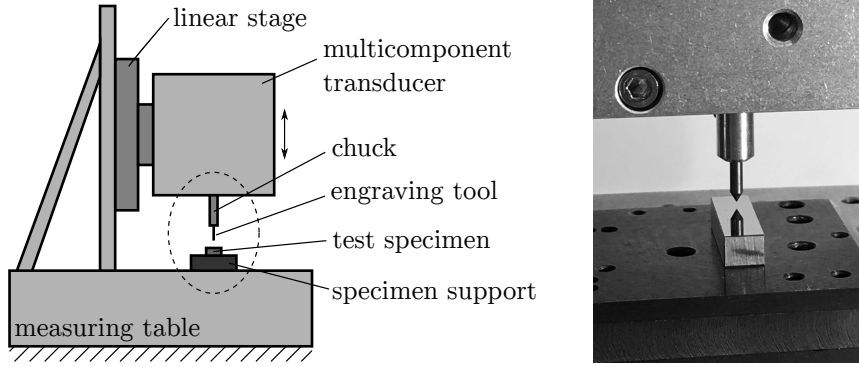


FIGURE 6.13: Drawing and picture of the experimental setup used for the surface micromachining tasks.

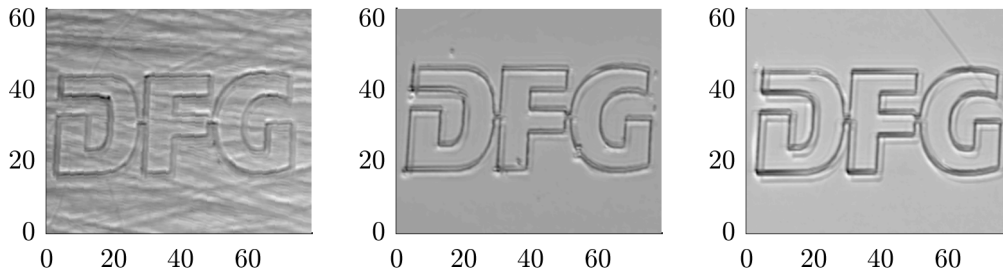


FIGURE 6.14: Test specimens used for the micromachining tasks. From left to right: hardened steel alloy (polished), silicon and glass. The scale shown is in micrometers.

for regulating the machining forces was implemented. This control system is described with details in subsection 3.3.6. Experiments were performed with specimens of three materials: polished steel, glass and silicon. The results obtained were evaluated with a nanopositioning and nanomeasuring machine.

6.3.1 EXPERIMENTAL SETUP FOR MICROMACHINING

The experimental setup used to perform the surface micromachining tasks is presented in figure 6.13. The main component of this setup is the multicomponent force and torque transducer, which is described in [12]. This system is a previous version of the multicomponent transducer developed in this work, which is described in section 3. With this system it is possible to perform the micromachining task itself and simultaneously measure the forces and torques involved in the process. A chuck used for mounting the engraving tool is attached to the sensing element of the multicomponent transducer. For obtaining these results, a boron nitride (PCBN) engraving tool with conical shape was used. The whole system is mounted on a precision measurement table. Different types of test specimens can be attached to the system with the help of a support. As shown in figure 6.14, three types of material were analyzed as test specimens: hardened steel alloy (polished), silicon and glass. A further component of the measurement system is the automated linear stage used to move the transducer vertically. In

TABLE 6.2: Specifications of the multicomponent force and torque transducer used for performing the micromachining tasks [12].

Specification	Value
Force measurement range	± 7 N
Torque measurement range	± 0.35 N m
Force measurement resolution	10 μ N
Torque measurement resolution	0.3 μ N m
Range of linear motion	± 0.2 mm
Range of angular motion	± 4 mrad
Linear positioning resolution	1 nm
Angular positioning resolution	20 nrad

this way it is possible to adjust the vertical position of the transducer for processing specimens of different shape. The specifications of the multicomponent force and torque transducer are shown in table 6.2. The resolution limits of the current experimental setup for the force, torque, position and angle measurement are given by these specifications.

6.3.2 RESULTS FOR MICROMACHINING

Figures 6.15 and 6.16 contain the measured normal and tangential forces for engraving a logo of the German Research Foundation (Deutsche Forschungsgemeinschaft, DFG) with a size of approximately $30 \mu\text{m} \times 70 \mu\text{m}$ on the polished steel surface. This logo was available as a set of 2D coordinates and, in order to execute the micromachining task, the path of the machining tool was defined by linear interpolation. Figure 6.17 contains the path of the tool over time. Additionally, figure 6.18 contains the measured forces and torques over the time. For this experiment a normal force of 20 mN was used and, for the tangential directions, a maximum force of about 7 mN was measured. The whole task was performed in approximately 8 min with a velocity of $0.86 \mu\text{m/s}$ for the tool tip.

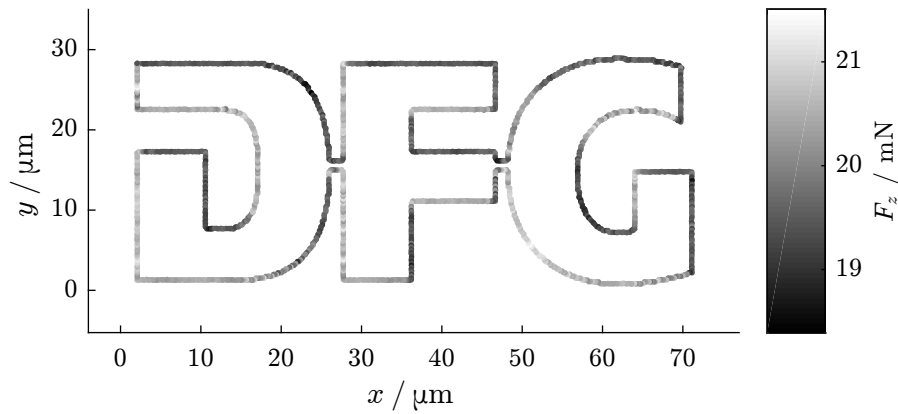


FIGURE 6.15: Normal force as a function of the position coordinates.

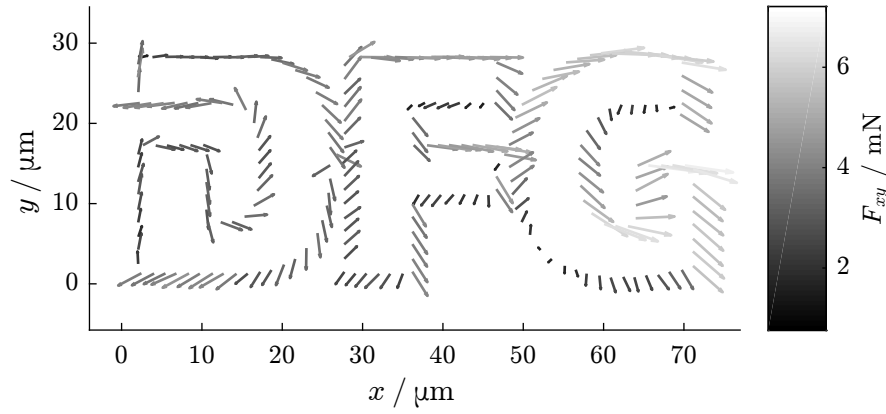


FIGURE 6.16: Tangential as a function of the position coordinates.

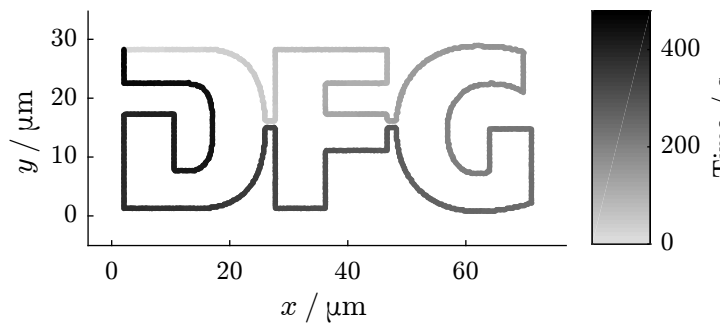


FIGURE 6.17: Engraving time as a function of the position coordinates.

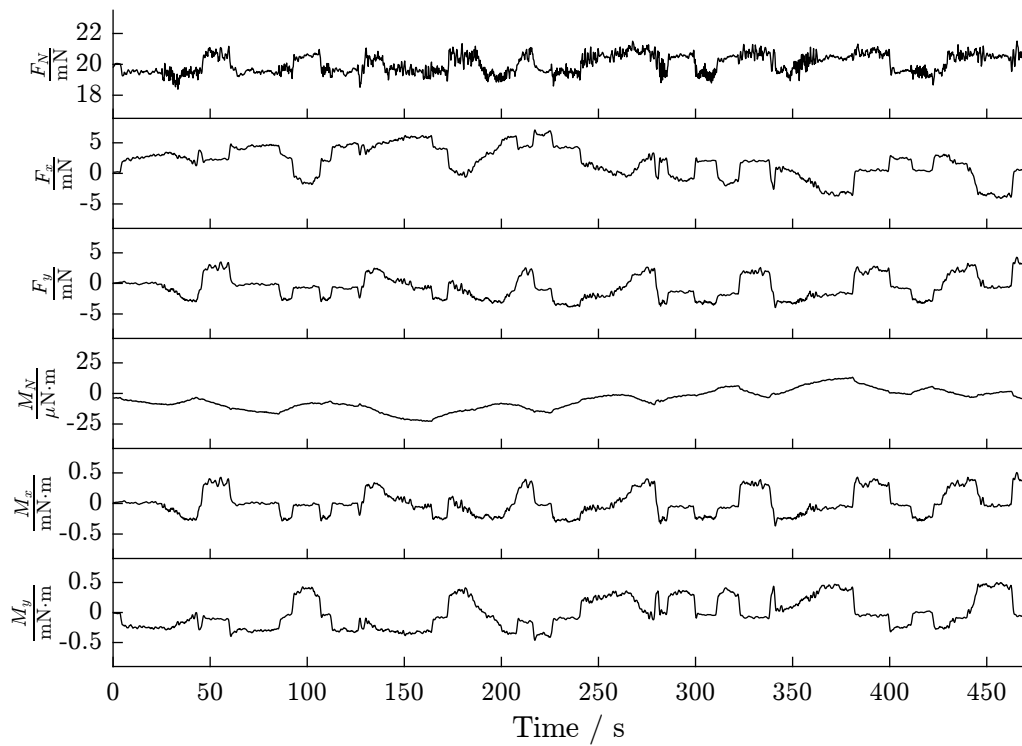


FIGURE 6.18: Measured forces and torques as a function of the engraving time.

The results shown in figure 6.14 were obtained by optically scanning the test specimens with a nanopositioning and nanomeasuring machine [102, 103] using a focus sensor [104]. Although the system employed during the micro-scratching has a positioning and angular resolution of respectively 1 nm and 20 nrad, the results shown here are in the scale of micrometres. The main reason for this limitation in the processing resolution is the boron nitride engraving tool used, which is not suitable for executing machining tasks with structures in the order of nanometres.

It was shown that, with the multicomponent transducer, structures with the size of some micrometers can be machined in polished steel, silicon and glass surfaces. For the microprocessing tasks considered, forces with the magnitude of millinewtons were measured. The system presented here exhibits a high potential for improvement concerning the machining tool used and the position and angle measuring system of the multicomponent force transducer. With an engraving tool with a smaller diamond tip, it would be possible to reduce the size of the structures to be machined, and with a laser interferometric system for the position and angle measurement, the positioning resolution could be reduced while providing a traceable measurement [105]. In this way, the application spectrum of the current system can eventually be extended to the fabrication of nanoscale structures in surfaces, such as already performed with atomic-force microscopes [106, 107].

CHAPTER 7

CONCLUSIONS

In this chapter, the main results obtained are reviewed and an outlook with improvement possibilities for multicomponent force and torque transducers is provided. The main results obtained include the contribution of this work to the state of the art of multicomponent force and torque measurement and the different applications considered. The improvement possibilities suggested involve the reduction of the uncertainty for the force and torque measurement with the instrument by performing design changes.

7.1 MAIN RESULTS

The design of an instrument used to measure three force and three torque components simultaneously was described here. The system is based on the electromagnetic force compensation and Kibble balance principles and was designed with the objective to simplify the calibration procedure and improve the measurement of forces and torques. With the system proposed here, it is not necessary to derive the force and torque quantities from the mass and gravity acceleration measurements. Instead, the forces and torques are derived from the measurement of electrical voltage, electrical resistance, position, angle and time. In this way, the multicomponent force and torque transducer can be calibrated in conditions where the local gravity acceleration is unknown or inexistent, as well as for any orientation in space. Since the calibration procedure is integrated in the transducer, it is more practical and simpler to perform. Additionally, the system is an alternative to traditional calibration methods for force and torque transducers, which use deadweights, and lower measurement uncertainties can be achieved.

A careful uncertainty analysis was performed with the objective to determine the uncertainties for both force and torque measurements. This involves the calibration of the measuring equipment used and the determination of the single uncertainty contributions. Some compensation strategies were implemented in order to provide a traceable force and torque measurement with the uncertainty specified, including the coil-current effect and the inductive coupling between the coils. The uncertainty analysis was performed for different configurations, involving the use of internal aperture slit position sensors or laser interferometers, for the position and angle measurement, and the use of analog-to-digital converters from the real-time controller or precision voltmeters, for the voltage measurement. The lowest uncertainty determined is for the force measurement by using the laser interferometer for position and angle measurement and the digital voltmeter for the voltage measurement. For a force of 2.2 N a relative expanded uncertainty

($k=2$) of 88 ppm was obtained. For the torque measurement, a relative expanded uncertainty ($k=2$) of 920 ppm was obtained considering a torque of 0.11 N m.

Verifications were performed with the multicomponent transducer by comparing results obtained with the integrated calibration procedure with results from traditional calibration methods based on deadweights and the local gravity acceleration. During these verifications, the weight force generated by a test mass of 77 g was measured with a relative standard uncertainty lower than 43 ppm. Measurement deviations caused by the coil-current effect and the temperature dependency of the actuator constant were also evaluated.

The application of multicomponent transducers to the identification of force and torque transducers, to the Lorentz force velocimetry and in micromachining was described and measurement results for these applications were provided. For the Lorentz force velocimetry, the results were obtained by using a strain-gauge multicomponent transducer and can be improved by using the instrument described here. A further application for the multicomponent transducer is the biomechatronics. This field involves the development or improvement of mechatronic products based on the knowledge acquired in biology. Force and torque measurements can be applied to biomechatronics for the investigation of biological systems and processes. The information obtained can be used in the development of new methods or in the design of new devices. An example for this application is the use of force and torque transducers to the investigation of tactile sensing mechanisms based on vibrissae, which are used by some animals of the mammal class [8, 9].

Table 7.1 shows the main differences of the system described here in comparison with a previous version of the multicomponent transducer based on the electromagnetic force compensation principle, which is presented in [12]. The main improvement relative to the previous system is the integration of the calibration procedure. In order to implement the integrated calibration and obtain the desired measurement uncertainty, it was necessary to increase the actuator constant of the voice coil actuators, to change the material of the coil forms, to change the amplifier electronics for the position sensors, to perform some modifications in the design of the transducer to enable the adjustment of all voice coils, to change the wires used to transmit the electrical current, to add six actuators to the sensing element, to add a switching system to the transducer and to use 18 additional analog-to-digital converters and 6 additional digital-to-analog converters. Another improvement is the integration of a temperature measuring system for the magnet systems of the actuators, which can be used to compensate the temperature dependency of the magnetic field generated by the permanent magnets. This compensation is important if the transducer suffers temperature changes during the sensing mode. The air pressure and air humidity measuring systems can be used to determine changes in the air density, which cause a change in the buoyancy force generated in the sensing element. The pluggable resistance modules simplify the calibration and investigation of the resistors used. The use of modules and interfaces also simplifies possible system upgrades and the replacement of faulty components. The measuring range for both force and torque measurements was reduced with the objective to design a multicomponent transducer for applications with forces and torques smaller than 2.2 N and

TABLE 7.1: Comparison between the multicomponent force and torque transducers from [12] and this work.

Transducer feature	Previous version [12]	This version
Integrated calibration	Not present	Present
Temperature compensation	Not present	For 12 magnets
Actuator constant (k_{Bl})	4.5 N/A	20 N/A
Material of coil forms	Aluminum	Polyacetal
Amplifier for position sensors	Bridge	Transimpedance
Air pressure measurement	Not present	Present
Relative humidity measurement	Not present	Present
Pluggable resistance modules	Not present	Present
Adjustment of all voice coils	Not possible	Possible
Wires for current transmission	100 μ m cooper	25 μ m gold
Number of voice coil actuators	6	12
Integrated switching system	Not present	Present
AD converters used	12	30
DA converters used	6	12
Force measurement range	7 N	2.2 N
Torque measurement range	0.35 Nm	0.11 Nm
Achievable relative uncertainty*	210 ppm	88 ppm

*Relative expanded measurement uncertainty ($k=2$)

0.11 N m respectively. With all changes performed, the relative expanded uncertainty ($k=2$) for the force measurement could be reduced from 210 ppm to 88 ppm.

7.2 OUTLOOK

Based on the results obtained with the prototype of the system, improvement possibilities for the multicomponent transducer can be identified. A change in the mechanical hardware of the transducer with the objective to reduce the amount of parts and focus in a monolithic design can provide a more stable behavior and simplify the assembling processes. For instance, with a more stable mechanical hardware, the relative position between the aperture slits suffers less variation and the integrated position measuring system can be improved. The electromagnetic actuators used can also be improved by changing the permanent magnet design [27] in order to obtain a more uniform gradient for the magnetic field. The material of the permanent magnet can also be changed to reduce the temperature dependency of the magnetic field strength. The distance between the actuators can be increased with the objective to eliminate effects caused by the inductive coupling. The mechanical compliance caused by the metallic wires can also be reduced by using thinner wires or by changing the design of the transducer in a way to avoid the use of the wires. For some applications it is desired to reduce the form factor of the transducer in order to have a miniaturized design. This is possible by changing the mechanical design and reducing the size of the different

components of the transducer. By using an integrated position and angle measuring system based on laser interferometer, the uncertainty for the determination of the actuator constants can be reduced. The multicomponent transducer can also be improved by integrating a more suitable multi-channel voltage measuring system. These improvement possibilities are suggested as further work for reducing the uncertainty for the force and torque measurements with multicomponent transducers.

APPENDIX A

USE OF COMMERCIALY AVAILABLE PRODUCTS

In this appendix references to specific commercial products, processes, or services used during the work are provided. These references do not constitute or imply any endorsement, recommendation, or favoring by the author of this work.

TABLE A.1: List of commercially available off-the-shelf products used in this work.

Reference	Product description	Manufacturer
CPU-B	DS1006 processor board	dSPACE GmbH
ADC-B	DS2004 high-speed A/D board	dSPACE GmbH
DAC-B	DS2102 high-resolution D/A board	dSPACE GmbH
GPIO-B	DS4003 digital I/O board	dSPACE GmbH
PFR	VHA518-11Z 4 terminal resistor	Vishay Precision Group, Inc.
RLY	G6AK-274P-STLT-5V low signal relay	OMRON Corporation
VCA	LA13-12-000B voice coil actuator	BEI Kimco
PHT	MS8607-02BA01 PHT combination sensor	TE Connectivity Ltd.
TPS	TSYS01 digital temperature sensors	TE Connectivity Ltd.
LED-PS	L9337-2 infrared LED	Hamamatsu Photonics K.K.
DPD-PS	SFH 221 silicon differential photodiode	Osram Licht AG
TBLI	SP 2000 TR triple-beam interferometer	SIOS Meßtechnik GmbH
SBLI	SP 500 laser interferometer	SIOS Meßtechnik GmbH
HENEL	Stabilized HeNe Laser SL 03	SIOS Meßtechnik GmbH
DVM	3458A digital multimeter, 8 1/2 digit	Keysight Technologies, Inc.
FCTR	53131A Counter with option 012	Keysight Technologies, Inc.
PCS	3245A universal source	Hewlett-Packard Company
GPSFR	RS-CGGO10 GPS frequency reference	INWAVE AG
LS2A	LS-110 linear translation stage	Physik Instrumente GmbH & Co.KG
LS1A	M-403.4PD precision translation stage	Physik Instrumente GmbH & Co.KG
GCW	Gold and cooper wires in different diameters	Goodfellow Cambridge Ltd.
SMAB	ME235S semi micro analytical balance	Sartorius AG
VCAL	5720A multifunction calibrator	Fluke Corporation
FRCMB	FC1500-250-WG optical frequency comb	Menlo Systems GmbH
WLMET	WLM-VIS integrated wavelength meters	Menlo Systems GmbH
MCSCN	High-precision scanner 2024	PREMA Präzisionstechnik GmbH

APPENDIX B

TERMS AND DEFINITIONS

In this appendix a list of some terms defined in the literature and used in this work are mentioned.

The term **multicomponent transducer**, used here as a reference to multicomponent force and torque measuring instruments, is present in the VDI/VDE/DKD 2638 guideline [24]. In the force and torque measurement literature, such devices are also referred to as multicomponent sensors or similar terms.

Further terms used here are **force** (113-03-14), **torque** (113-03-26), **resistance** (131-12-04), **time** (113-01-03), **electric current** (121-11-13), **position vector** (102-03-15) and **angle** (102-03-29), from the International Electrotechnical Vocabulary (IEC 60050) [108]. This literature reference contains many other terms used in this work.

The following terms are defined in the International Vocabulary of Metrology [109] and the definitions are reproduced here:

quantity “property of a phenomenon, body, or substance, where the property has a magnitude that can be expressed as a number and a reference”

measurement “process of experimentally obtaining one or more quantity values that can reasonably be attributed to a quantity”

measurand “quantity intended to be measured”

indication “quantity value provided by a measuring instrument or a measuring system”

measurement uncertainty “non-negative parameter characterizing the dispersion of the quantity values being attributed to a measurand, based on the information used”

calibration “operation that, under specified conditions, in a first step, establishes a relation between the quantity values with measurement uncertainties provided by measurement standards and corresponding indications with associated measurement uncertainties and, in a second step, uses this information to establish a relation for obtaining a measurement result from an indication”

measurement standard “realization of the definition of a given quantity, with stated quantity value and associated measurement uncertainty, used as a reference”

measurement result “set of quantity values being attributed to a measurand together with any other available relevant information”

resolution “smallest change in a quantity being measured that causes a perceptible change in the corresponding indication”

measurement repeatability “measurement precision under a set of repeatability conditions of measurement”

measurement precision “closeness of agreement between indications or measured quantity values obtained by replicate measurements on the same or similar objects under specified conditions”

repeatability condition of measurement “condition of measurement, out of a set of conditions that includes the same measurement procedure, same operators, same measuring system, same operating conditions and same location, and replicate measurements on the same or similar objects over a short period of time”

metrological traceability “property of a measurement result whereby the result can be related to a reference through a documented unbroken chain of calibrations, each contributing to the measurement uncertainty”

measurement procedure “detailed description of a measurement according to one or more measurement principles and to a given measurement method, based on a measurement model and including any calculation to obtain a measurement result”

measurement principle “phenomenon serving as a basis of a measurement”

measurement method “generic description of a logical organization of operations used in a measurement”

measurement model “mathematical relation among all quantities known to be involved in a measurement”

BIBLIOGRAPHY

- [1] R. Schwartz, “Teil B: Sensoren, Kraft, Masse, Drehmoment”, in *Handbuch der Mess- und Automatisierungstechnik in der Produktion*, H.-J. Gevatter and U. Grünhaupt, Eds., Berlin: Springer, 2006, pp. 55–88. DOI: 10.1007/3-540-34823-9.
- [2] H.-R. Tränkler and L. M. Reindl, Eds., *Sensortechnik: Handbuch für Praxis und Wissenschaft*, 2nd ed., ser. VDI-Buch. Springer Vieweg, 2014, ISBN: 978-3-642-29941-4. DOI: 10.1007/978-3-642-29942-1.
- [3] B. F. R. Ewald, “Multi-component force balances for conventional and cryogenic wind tunnels”, *Measurement Science and Technology*, vol. 11, no. 6, R81, 2000. DOI: 10.1088/0957-0233/11/6/201.
- [4] E. Guizzo, “Anatomy of a crash-test dummy”, *IEEE Spectrum*, vol. 44, no. 10, pp. 42–49, 2007. DOI: 10.1109/MSPEC.2007.4337665.
- [5] A. Thess, E. V. Votyakov, and Y. Kolesnikov, “Lorentz Force Velocimetry”, *Phys. Rev. Lett.*, vol. 96, p. 164 501, 16 2006. DOI: 10.1103/PhysRevLett.96.164501.
- [6] D. Hernández, R. Marangoni, J. Schleichert, C. Karcher, T. Fröhlich, and T. Wondrak, “Numerical and experimental study on vorticity measurement in liquid metal using local Lorentz force velocimetry”, *Measurement Science and Technology*, vol. 29, no. 3, p. 035 301, 2018. DOI: 10.1088/1361-6501/aa9f85.
- [7] R. R. Marangoni, J. Schleichert, I. Rahneberg, R. Mastlylo, E. Manske, and T. Fröhlich, “Multi-component force measurement in micromachining”, *Technisches Messen*, vol. 84, p. 587, 9 2017. DOI: 10.1515/teme-2016-0066.
- [8] C. Will, C. Behn, and J. Steigenberger, “Object contour scanning using elastically supported technical vibrissae”, *ZAMM - Journal of Applied Mathematics and Mechanics*, 2017. DOI: 10.1002/zamm.201600161.
- [9] J. A. Birdwell, J. H. Solomon, M. Thajchayapong, M. A. Taylor, M. Cheely, R. B. Towal, J. Conradt, and M. J. Z. Hartmann, “Biomechanical models for radial distance determination by the rat vibrissal system”, *Journal of Neurophysiology*, vol. 98, pp. 2439–2455, 4 2007. DOI: 10.1152/jn.00707.2006.
- [10] D. M. Stefanescu, *Handbook of Force Transducers: Principles and Components*, 1st ed. Springer-Verlag Berlin Heidelberg, 2011. DOI: 10.1007/978-3-642-18296-9.

- [11] M. Kühnel, “Rückführbare Messung der mechanischen Eigenschaften von Federkörpern für die Kraftmesstechnik”, PhD thesis, Technische Universität Ilmenau, 2013. [Online]. Available: <http://nbn-resolving.de/urn:nbn:de:gbv:ilm1-2013000426>.
- [12] J. Schleichert, “Entwicklung und Untersuchung von Mehrkomponentensensoren für Kraft und Drehmoment”, PhD thesis, Technische Universität Ilmenau, 2015. [Online]. Available: <http://nbn-resolving.de/urn:nbn:de:gbv:ilm1-2016000165>.
- [13] J. Nitsche, S. Baumgarten, M. Petz, D. Röske, R. Kümme, and R. Tutsch, “Measurement uncertainty evaluation of a hexapod-structured calibration device for multi-component force and moment sensors”, *Metrologia*, vol. 54, no. 2, p. 171, 2017. DOI: 10.1088/1681-7575/aa5b66.
- [14] Deutsches Institut für Normung, *DIN EN ISO 376: Metallische Werkstoffe – Kalibrierung der Kraftmessgeräte für die Prüfung von Prüfmaschinen mit einachsiger Beanspruchung*, 2011.
- [15] Deutsche Akkreditierungsstelle GmbH, *DAkkS-DKD-R 3-3 Kalibrierung von Kraftmessgeräten*, 2010.
- [16] Deutsche Akkreditierungsstelle GmbH, *DAkkS-DKD-R 3-9 Kontinuierliche Kalibrierung von Kraftaufnehmern nach dem Vergleichsverfahren*, 2010.
- [17] Deutsche Akkreditierungsstelle GmbH, *DAkkS-DKD-R 3-5 Kalibrierung von Drehmomentmessgeräten für statische Wechseldrehmomente*, 2010.
- [18] Deutsches Institut für Normung, *DIN 51309: Werkstoffprüfmaschinen – Kalibrierung von Drehmomentmessgeräten für statische Drehmomente*, 2005.
- [19] VDI/VDE-Gesellschaft Mess- und Automatisierungstechnik, *VDI/VDE 2646: Torque measuring devices - Minimum requirements in calibrations*, 2006.
- [20] ASTM International, *ASTM F3109-16: Standard Test Method for Verification of Multi-Axis Force Measuring Platforms*, 2016.
- [21] International Organization of Legal Metrology, *OIML R 60-1: Metrological regulation for load cells - Part 1: Metrological and technical requirements*, 2017.
- [22] International Organization of Legal Metrology, *OIML R 60-2: Metrological regulation for load cells - Part 2: Metrological controls and performance tests*, 2017.
- [23] International Organization of Legal Metrology, *OIML R 60-3: Metrological regulation for load cells - Part 3: Test report format*, 2017.
- [24] VDI/VDE-Gesellschaft Mess- und Automatisierungstechnik, *VDI/VDE/DKD 2638: Characteristics of force transducers - Terms and definitions*, 2008.

- [25] R. R. Marangoni, J. Schleichert, I. Rahneberg, F. Hilbrunner, and T. Fröhlich, “A self-calibrating multicomponent force/torque measuring system”, in *Proceedings of 59th Ilmenau Scientific Colloquium*, 2017. [Online]. Available: <http://nbn-resolving.de/urn:nbn:de:gbv:ilm1-2017iwk-081:5>.
- [26] R. R. Marangoni, J. Schleichert, I. Rahneberg, F. Hilbrunner, and T. Fröhlich, “A self-calibrating multicomponent force/torque measuring system”, *Measurement Science and Technology*, vol. 29, no. 7, p. 074 002, 2018. DOI: 10.1088/1361-6501/aac00f.
- [27] I. A. Robinson and S. Schlamminger, “The watt or Kibble balance: a technique for implementing the new SI definition of the unit of mass”, *Metrologia*, vol. 53, no. 5, A46, 2016. DOI: 10.1088/0026-1394/53/5/A46.
- [28] Y. Azuma, P. Barat, G. Bartl, H. Bettin, M. Borys, I. Busch, L. Cibik, G. D’Agostino, K. Fujii, H. Fujimoto, A. Hioki, M. Krumrey, U. Kuetgens, N. Kuramoto, G. Mana, E. Massa, R. Meeß, S. Mizushima, T. Narukawa, A. Nicolaus, A. Pramann, S. A. Rabb, O. Rienitz, C. Sasso, M. Stock, R. D. V. Jr, A. Waseda, S. Wundrack, and S. Zakel, “Improved measurement results for the Avogadro constant using a 28 Si-enriched crystal”, *Metrologia*, vol. 52, no. 2, p. 360, 2015. DOI: 10.1088/0026-1394/52/2/360.
- [29] D. Haddad, F. Seifert, L. S. Chao, A. Possolo, D. B. Newell, J. R. Pratt, C. J. Williams, and S. Schlamminger, “Measurement of the Planck constant at the National Institute of Standards and Technology from 2015 to 2017”, *Metrologia*, vol. 54, no. 5, p. 633, 2017.
- [30] B. M. Wood, C. A. Sanchez, R. G. Green, and J. O. Liard, “A summary of the Planck constant determinations using the NRC Kibble balance”, *Metrologia*, vol. 54, no. 3, p. 399, 2017. DOI: 10.1088/1681-7575/aa70bf.
- [31] G. A. Shaw, “Current state of the art in small mass and force metrology within the international system of units”, *Measurement Science and Technology*, vol. 29, no. 7, p. 072 001, 2018. DOI: 10.1088/1361-6501/aaac51.
- [32] T. Gast, *Eine registrierende Torsionswaage mit elektrischer Kompensation*, DE000000914445B, 1943.
- [33] T. Gast, *Elektronische Waage*, DE000001035371B, 1955.
- [34] M.-S. Kim, J.-H. Choi, J.-H. Kim, and Y.-K. Park, “SI-traceable determination of spring constants of various atomic force microscope cantilevers with a small uncertainty of 1%”, *Measurement Science and Technology*, vol. 18, no. 11, p. 3351, 2007. DOI: 10.1088/0957-0233/18/11/014.
- [35] G. A. Shaw, J. Stirling, J. A. Kramar, A. Moses, P. Abbott, R. Steiner, A. Koffman, J. R. Pratt, and Z. J. Kubarych, “Milligram mass metrology using an electrostatic force balance”, *Metrologia*, vol. 53, no. 5, A86, 2016. DOI: 10.1088/0026-1394/53/5/A86.

- [36] V. Nesterov, O. Belai, D. Nies, S. Buetefisch, M. Mueller, T. Ahbe, D. Naparty, R. Popadic, and H. Wolff, “SI-traceable determination of the spring constant of a soft cantilever using the nanonewton force facility based on electrostatic methods”, *Metrologia*, vol. 53, no. 4, p. 1031, 2016. DOI: 10.1088/0026-1394/53/4/1031.
- [37] S.-J. Chen, S.-S. Pan, Y.-S. Yeh, and Y.-C. Lin, “Measurement of cantilever spring constant using an electrostatic sensing and actuating force measurement system”, *Measurement Science and Technology*, vol. 25, no. 11, p. 115 006, 2014. DOI: 10.1088/0957-0233/25/11/115006.
- [38] P. Sun, M. Zhao, J. Jiang, Y. Zheng, Y. Han, and L. Song, “The differential method for force measurement based on electrostatic force”, *Journal of Sensors*, vol. 2017, p. 1 857 920, 2017. DOI: 10.1155/2017/1857920.
- [39] K.-H. Chung, G. A. Shaw, and J. R. Pratt, “Accurate noncontact calibration of colloidal probe sensitivities in atomic force microscopy”, *Review of Scientific Instruments*, vol. 80, no. 6, p. 065 107, 2009. DOI: 10.1063/1.3152335.
- [40] International Organization of Legal Metrology, *OIML R 111-1: Weights of classes E1, E2, F1, F2, M1, M1-2, M2, M2-3 and M3 - Part 1: Metrological and technical requirements*, 2004.
- [41] National Physical Laboratory, *Guide to the Measurement of Force*, 2013.
- [42] A. Nishino, K. Ueda, and K. Fujii, “Design of a new torque standard machine based on a torque generation method using electromagnetic force”, *Measurement Science and Technology*, vol. 28, no. 2, p. 025 005, 2017. DOI: 10.1088/1361-6501/28/2/025005.
- [43] S. Baumgarten, H. Kahmann, and D. Röske, “Metrological characterization of a 2 kNm torque standard machine for superposition with axial forces up to 1 MN”, *Metrologia*, vol. 53, no. 5, p. 1165, 2016. DOI: 10.1088/0026-1394/53/5/1165.
- [44] C. Ferrero, L. Q. Zhong, C. Marinari, and E. Martino, “New automatic multicomponent calibration system with crossed-flexure levers”, in *Proceedings of the Third International Symposium on Measurement and Control in Robotics*, 1993.
- [45] G.-S. Kim, “The development of a six-component force/moment sensor testing machine and evaluation of its uncertainty”, *Measurement Science and Technology*, vol. 11, no. 9, p. 1377, 2000. DOI: 10.1088/0957-0233/11/9/318.
- [46] P. A. Parker, M. Morton, N. Draper, and W. Line, “A single-vector force calibration method featuring the modern design of experiments”, in *Proceedings of the 39th AIAA Aerospace Sciences Meeting & Exhibit*, 2001. DOI: 10.2514/6.2001-170.
- [47] P. A. Parker and T. Liu, “Uncertainty analysis of the single-vector force balance calibration system”, in *Proceedings of the 22nd AIAA Aerodynamic Measurement Technology and Ground Testing Conference*, 2002. DOI: 10.2514/6.2002-2792.

- [48] R. D. Rhew, P. A. Parker, T. H. Johnson, and D. Landman, “Variable acceleration force calibration system (VACS)”, in *Proceedings of 9th International Symposium on Strain-Gaged Balance*, 2014. [Online]. Available: <https://ntrs.nasa.gov/search.jsp?R=20160000775>.
- [49] B. P. Kibble, “A measurement of the gyromagnetic ratio of the proton by the strong field method”, in *Atomic Masses and Fundamental Constants*, J. H. Sanders and A. H. Wapstra, Eds., vol. 5, New York: Springer, 1976, pp. 545–51. DOI: 10.1007/978-1-4684-2682-3_80.
- [50] B. Josephson, “Possible new effects in superconductive tunnelling”, *Physics Letters*, vol. 1, no. 7, pp. 251–253, 1962, ISSN: 0031-9163. DOI: 10.1016/0031-9163(62)91369-0.
- [51] K. v. Klitzing, G. Dorda, and M. Pepper, “New method for high-accuracy determination of the fine-structure constant based on quantized hall resistance”, *Phys. Rev. Lett.*, vol. 45, pp. 494–497, 6 1980. DOI: 10.1103/PhysRevLett.45.494.
- [52] D. Haddad, F. Seifert, L. S. Chao, S. Li, D. B. Newell, J. R. Pratt, C. Williams, and S. Schlamminger, “Invited Article: A precise instrument to determine the Planck constant, and the future kilogram”, *Review of Scientific Instruments*, vol. 87, no. 6, p. 061 301, 2016. DOI: 10.1063/1.4953825.
- [53] S. Li, F. Bielsa, M. Stock, A. Kiss, and H. Fang, “Coil-current effect in Kibble balances: analysis, measurement, and optimization”, *Metrologia*, vol. 55, no. 1, p. 75, 2018. DOI: 10.1088/1681-7575/aa9a8e.
- [54] S. Li, S. Schlamminger, D. Haddad, F. Seifert, L. Chao, and J. R. Pratt, “Coil motion effects in watt balances: A theoretical check”, *Metrologia*, vol. 53, no. 2, p. 817, 2016. DOI: 10.1088/0026-1394/53/2/817.
- [55] H. Fang, F. Bielsa, A. Kiss, T. Lavergne, Y. F. Lu, L. Robertsson, E. de Mirandés, S. Solve, and M. Stock, “Progress on the BIPM watt balance”, in *2016 Conference on Precision Electromagnetic Measurements (CPEM 2016)*, Jul. 2016, pp. 1–2. DOI: 10.1109/CPEM.2016.7540540.
- [56] H. Fang, A. Kiss, A. Picard, and M. Stock, “A watt balance based on a simultaneous measurement scheme”, *Metrologia*, vol. 51, no. 2, S80, 2014. DOI: 10.1088/0026-1394/51/2/S80.
- [57] D. Kim, B.-C. Woo, K.-C. Lee, K.-B. Choi, J.-A. Kim, J. W. Kim, and J. Kim, “Design of the KRISS watt balance”, *Metrologia*, vol. 51, no. 2, S96, 2014. DOI: 10.1088/0026-1394/51/2/S96.
- [58] M. Thomas, D. Ziane, P. Pinot, R. Karcher, A. Imanaliev, F. P. D. Santos, S. Merlet, F. Piquemal, and P. Espel, “A determination of the Planck constant using the LNE Kibble balance in air”, *Metrologia*, vol. 54, no. 4, p. 468, 2017. DOI: 10.1088/1681-7575/aa7882.
- [59] H. Baumann, A. Eichenberger, F. Cosandier, B. Jeckelmann, R. Clavel, D. Reber, and D. Tommasini, “Design of the new METAS watt balance experiment Mark II”, *Metrologia*, vol. 50, no. 3, p. 235, 2013. DOI: 10.1088/0026-1394/50/3/235.

- [60] C. M. Sutton, “An oscillatory dynamic mode for a watt balance”, *Metrologia*, vol. 46, no. 5, p. 467, 2009. DOI: 10.1088/0026-1394/46/5/010.
- [61] Z. Zhonghua, H. Qing, L. Zhengkun, H. Bing, L. Yunfeng, L. Jiang, L. Chen, L. Shisong, X. Jinxin, W. Nong, W. Gang, and G. Hongzhi, “The joule balance in NIM of China”, *Metrologia*, vol. 51, no. 2, S25, 2014. DOI: 10.1088/0026-1394/51/2/S25.
- [62] D. Haddad, F. Seifert, L. Chao, A. Cao, G. Sineriz, J. Pratt, D. Newell, and S. Schlamminger, “First Measurements of the Flux Integral With the NIST-4 Watt Balance”, *IEEE Transactions on Instrumentation and Measurement*, vol. 64, no. 6, pp. 1642–1649, 2015. DOI: 10.1109/TIM.2015.2407531.
- [63] B. P. Kibble, I. A. Robinson, and J. H. Belliss, “A Realization of the SI Watt by the NPL Moving-coil Balance”, *Metrologia*, vol. 27, no. 4, p. 173, 1990. DOI: 10.1088/0026-1394/27/4/002.
- [64] C. A. Sanchez, B. M. Wood, D. Inglis, and I. A. Robinson, “Elimination of Mass-Exchange Errors in the NRC Watt Balance”, *IEEE Transactions on Instrumentation and Measurement*, vol. 62, no. 6, pp. 1506–1511, Jun. 2013. DOI: 10.1109/TIM.2012.2225957.
- [65] H. Ahmedov, N. Babayigit, B. Korutlu, and R. Orhan, “Preliminary Planck constant measurements via UME oscillating - magnet Kibble balance”, *Metrologia*, vol. 55, no. 3, p. 326, 2018. DOI: 10.1088/1681-7575/aab23d.
- [66] C. Rothleitner, J. Schleichert, N. Rogge, L. Günther, S. Vasilyan, F. Hilbrunner, D. Knopf, T. Fröhlich, and F. Härtig, “The Planck-Balance - using a fixed value of the Planck constant to calibrate E1/E2-weights”, *Measurement Science and Technology*, vol. 29, no. 7, p. 074 003, 2018. DOI: 10.1088/1361-6501/aabc9e.
- [67] F. Hilbrunner, I. Rahneberg, and T. Fröhlich, “Wattwaage mit Hebelübersetzung auf Basis eines kommerziellen EMK-Wägesystems”, *Technisches Messen*, 2017. DOI: 10.1515/teme-2017-0065.
- [68] J. Schleichert, I. Rahneberg, F. Hilbrunner, and T. Fröhlich, “Mehrkomponenten-Kraft- und -Drehmomentsensor nach dem Prinzip der elektromagnetischen Kompensation”, *Technisches Messen*, vol. 83, p. 445, 7-8 2016. DOI: 10.1515/teme-2015-0088.
- [69] J. Sindram, “Entwicklung einer elektrischen Umschalteinheit für Anwendungen in der Präzisionsmesstechnik”, Master’s thesis, Technische Universität Ilmenau, Germany, 2018.
- [70] C. Diethold, T. Fröhlich, F. Hilbrunner, and G. Jäger, “High precision optical position sensor for electromagnetic force compensated balances”, in *Proceedings of the IMEKO 21st TC3 International Conference*, 2010.
- [71] R. N. Jazar, *Advanced Dynamics: Rigid Body, Multibody, and Aerospace Applications*, 1st ed. Wiley, 2011. DOI: 10.1002/9780470950029.

- [72] J. Schleichert, M. Carlstedt, R. R. Marangoni, I. Rahneberg, F. Hilbrunner, and T. Fröhlich, “Dynamische Charakterisierung eines Dreikomponenten Kraftsensors mit Hilfe eines Lorentzkraft-Lastwechslers”, *Technisches Messen*, vol. 83, p. 430, 7-8 2016. DOI: 10.1515/teme-2015-0089.
- [73] J. Pyrhonen, T. Jokinen, and V. Hrabovcova, *Design of Rotating Electrical Machines*, 1st ed. Wiley, Dec. 2009. DOI: 10.1002/9780470740095.
- [74] R. R. Marangoni, I. Rahneberg, F. Hilbrunner, R. Theska, and T. Fröhlich, “Analysis of weighing cells based on the principle of electromagnetic force compensation”, *Measurement Science and Technology*, vol. 28, no. 7, p. 075 101, 2017. DOI: 10.1088/1361-6501/aa6bcd.
- [75] K. C. Chen, L. K. Warne, Y. T. Lin, R. L. Kinzel, J. D. Huff, M. B. McLean, M. W. Jenkins, and B. M. Rutherford, “Conductor fusing and gapping for bond wires”, *Progress In Electromagnetics Research M*, vol. 31, pp. 199–214, 2013. DOI: 10.2528/PIERM13051311.
- [76] H. Baumgartl, “Optimierung dynamischer Waagen nach dem Prinzip der elektromagnetischen Kraftkompensation mittels numerischer Modelle zur Systemsimulation”, PhD thesis, Technische Universität Ilmenau, 2015. [Online]. Available: <http://nbn-resolving.de/urn:nbn:de:gbv:ilm1-2015000362>.
- [77] M. Srbulov, *Ground Vibration Engineering*. Springer Netherlands, 2010. DOI: 10.1007/978-90-481-9082-9.
- [78] G. Antonelli, N. Sarkar, and S. Chiaverini, “External force control for underwater vehicle-manipulator systems”, in *1999. Proceedings of the 38th IEEE Conference on Decision and Control*, vol. 3, 1999, 2975–2980 vol.3. DOI: 10.1109/CDC.1999.831389.
- [79] R. R. Marangoni, J. Schleichert, and T. Fröhlich, “Multicomponent force/torque sensor with integrated calibration system”, in *Sensors and Measuring Systems; 19th ITG/GMA-Symposium*, Jun. 2018, pp. 1–4.
- [80] J. A. Stone and J. H. Zimmerman, *Index of refraction of air*, 2001. [Online]. Available: <http://emtoolbox.nist.gov/Wavelength/Documentation.asp>.
- [81] Working Group 1 of the Joint Committee for Guides in Metrology, *Evaluation of measurement data - Guide to the expression of uncertainty in measurement*, 2008.
- [82] A. V. Oppenheim and R. W. Schaffer, *Digital Signal Processing*. Pearson, 1974.
- [83] A. Rüfenacht, N. E. Flowers-Jacobs, and S. P. Benz, “Impact of the latest generation of Josephson voltage standards in ac and dc electric metrology”, *Metrologia*, vol. 55, no. 5, S152, 2018. DOI: 10.1088/1681-7575/aad41a.
- [84] S. Schlamminger, “Design of the Permanent-Magnet System for NIST-4”, *IEEE Transactions on Instrumentation and Measurement*, vol. 62, pp. 1524–1530, 6 Jun. 2013. DOI: 10.1109/TIM.2012.2230771.

- [85] R. R. Marangoni, J. Schleichert, I. Rahneberg, and T. Fröhlich, “Static and dynamic identification of multi-component force and torque sensors”, in *Proceedings of the IMEKO 23rd TC3 International Conference*, 2017. [Online]. Available: <https://www.imeko.org/publications/tc3-2017/IMEKO-TC3-2017-006.pdf>.
- [86] A. Link, B. Glöckner, C. Schlegel, R. Kumme, and C. Elster, “System identification of force transducers for dynamic measurements”, in *Proceedings of the XIX IMEKO World Congress*, 2009. [Online]. Available: <https://www.imeko.org/publications/wc-2009/IMEKO-WC-2009-TC3-039.pdf>.
- [87] Y. Fujii and H. Fujimoto, “Proposal for an impulse response evaluation method for force transducers”, *Measurement Science and Technology*, vol. 10, no. 4, N31, 1999. DOI: 10.1088/0957-0233/10/4/006.
- [88] J. Schleichert, I. Rahneberg, and T. Fröhlich, “Calibration of a novel six-degree-of-freedom force/torque measurement system”, *International Journal of Modern Physics: Conference Series*, vol. 24, p. 1360017, 2013. DOI: 10.1142/S2010194513600173.
- [89] Y.-K. Park, R. Kumme, D. Roeske, and D.-I. Kang, “Column-type multi-component force transducers and their evaluation for dynamic measurement”, *Measurement Science and Technology*, vol. 19, no. 11, p. 115205, 2008. DOI: 10.1088/0957-0233/19/11/115205.
- [90] R. M. Voyles, J. D. Morrow, and P. K. Khosla, “The Shape From Motion Approach to Rapid and Precise Force/Torque Sensor Calibration”, *J. Dyn. Sys., Meas., Control*, vol. 119, no. 2, pp. 229–235, 1997. DOI: 10.1115/1.2801238.
- [91] K. Kim, Y. Sun, R. M. Voyles, and B. J. Nelson, “Calibration of Multi-Axis MEMS Force Sensors Using the Shape-From-Motion Method”, *IEEE Sensors Journal*, vol. 7, no. 3, pp. 344–351, 2007. DOI: 10.1109/JSEN.2006.890141.
- [92] R. Isermann and M. Münchhof, *Identification of Dynamic Systems*. Springer Verlag Berlin Heidelberg, 2011. DOI: 10.1007/978-3-540-78879-9.
- [93] A. Thess, E. Votyakov, B. Knaepen, and O. Zikanov, “Theory of the Lorentz force flowmeter”, *New Journal of Physics*, vol. 9, no. 8, p. 299, 2007. DOI: 10.1088/1367-2630/9/8/299.
- [94] D. Hernández, J. Schleichert, C. Karcher, T. Fröhlich, T. Wondrak, and K. Timmel, “Local Lorentz force flowmeter at a continuous caster model using a new generation multicomponent force and torque sensor”, *Measurement Science and Technology*, vol. 27, no. 6, p. 065302, 2016. DOI: 10.1088/0957-0233/27/6/065302.
- [95] D. Hernández, T. Boeck, C. Karcher, and T. Wondrak, “Numerical and experimental study of the effect of the induced electric potential in Lorentz force velocimetry”, *Measurement Science and Technology*, vol. 29, no. 1, p. 015301, 2018. DOI: 10.1088/1361-6501/aa9095.

- [96] J. W. Wittwer, T. Gomm, and L. L. Howell, "Surface micromachined force gauges: Uncertainty and reliability", *Journal of Micromechanics and Microengineering*, vol. 12, no. 1, p. 13, 2002. DOI: 10.1088/0960-1317/12/1/303.
- [97] M. Lemkin and B. E. Boser, "A three-axis micromachined accelerometer with a cmos position-sense interface and digital offset-trim electronics", *IEEE Journal of Solid-State Circuits*, vol. 34, no. 4, pp. 456–468, 1999. DOI: 10.1109/4.753678.
- [98] D. Dornfeld, S. Min, and Y. Takeuchi, "Recent advances in mechanical micromachining", *{CIRP} Annals - Manufacturing Technology*, vol. 55, no. 2, pp. 745–768, 2006. DOI: 10.1016/j.cirp.2006.10.006.
- [99] J. Wulfsberg and G. Brudek, "Detection of cutting forces in micro machining operations", in *Proceedings of the 5th international conference of the European Society for Precision Engineering and Nanotechnology (euspen)*, vol. 2, 2005, pp. 533–536.
- [100] R. Transchel, J. Stirnimann, M. Blattner, B. Bill, R. Thiel, F. Kuster, and K. Wegener, "Effective dynamometer for measuring high dynamic process force signals in micro machining operations", *Procedia CIRP*, vol. 1, pp. 558–562, 2012. DOI: 10.1016/j.procir.2012.04.099.
- [101] E. Korkmaz, B. A. Gozen, B. Bediz, and O. B. Ozdoganlar, "High-frequency compensation of dynamic distortions in micromachining force measurements", *Procedia Manufacturing*, vol. 1, pp. 534–545, 2015. DOI: 10.1016/j.promfg.2015.09.027.
- [102] E. Manske, "Modular family of sensors for a nanopositioning and nanomeasuring machine", *International Journal of Optomechatronics*, vol. 7, no. 2, pp. 122–135, 2013. DOI: 10.1080/15599612.2013.777823.
- [103] E. Manske, G. Jäger, T. Hausotte, and R. Füll, "Recent developments and challenges of nanopositioning and nanomeasuring technology", *Measurement Science and Technology*, vol. 23, no. 7, p. 074001, 2012. DOI: 10.1088/0957-0233/23/7/074001.
- [104] R. Mastilo, D. Dontsov, E. Manske, and G. Jäger, "A focus sensor for an application in a nanopositioning and nanomeasuring machine", in *Optical Measurement Systems for Industrial Inspection IV, Proceedings of SPIE*, vol. 5856, 2005, pp. 238–244. DOI: 10.1117/12.612887.
- [105] C. Diethold, M. Kühnel, F. Hilbrunner, T. Fröhlich, and E. Manske, "Determination of force to displacement curves using a nanopositioning system based on electromagnetic force compensated balances", *Measurement*, vol. 51, pp. 343–348, 2014. DOI: 10.1016/j.measurement.2014.02.034.
- [106] M. J. Jackson, *Micro and Nanomanufacturing*. Springer US, 2007. DOI: 10.1007/b136902.

- [107] Y.-P. Song, S. Wu, L.-Y. Xu, J.-M. Zhang, D. J. Dorantes-Gonzalez, X. Fu, and X.-D. Hu, “Calibration of the effective spring constant of ultra-short cantilevers for a high-speed atomic force microscope”, *Measurement Science and Technology*, vol. 26, no. 6, p. 065 001, 2015. DOI: 10.1088/0957-0233/26/6/065001.
- [108] International Electrotechnical Commission (IEC) - Technical Committee 1, *International Electrotechnical Vocabulary*, 2018. [Online]. Available: <http://www.electropedia.org/>.
- [109] Joint Committee for Guides in Metrology, *International vocabulary of metrology – Basic and general concepts and associated terms (VIM)*, 2012.